TECHNISCHE UNIVERSITÄT WIEN

DIPLOMA THESIS

A Dynamic Multi-Zone gPROMS Model of Basic Oxygen Steelmaking

submitted in satisfaction of the requirements for the degree of
Diplom-Ingenieurin (Dipl.-Ing. Or DI)

within the scope of the master programme
Chemical and Process Engineering

at the Faculty of Technical Chemistry TU Wien,
Institute of Chemical, Environmental and Bioscience Engineering

by
Arleen Victoria Walk, BSc
Matriculation number: 01226378

under the supervision of

Ao.Univ.Prof. Dipl.-Ing. Dr.techn. **Michael Harasek**
Assistant Prof. Dipl.-Ing. Dr.techn. **Walter Wukovits**

Vienna, _____ _____ _____
(Signature author) (Signature supervisor)

TECHNISCHE UNIVERSITÄT WIEN

DIPLOMARBEIT

Ein dynamisches Multizonenmodell des Sauerstoffblaseverfahrens in gPROMS

zur Erlangung des akademischen Grades
Diplom-Ingenieurin (Dipl.-Ing. oder DI)

im Rahmen des Studiums
Verfahrenstechnik

ausgeführt an der Fakultät Technische Chemie TU Wien, Institute für Verfahrenstechnik, Umwelttechnik und technische Biowissenschaften

eingereicht von
Arleen Victoria Walk, BSc
Matrikelnummer: 01226378

unter Anleitung von

Ao.Univ.Prof. Dipl.-Ing. Dr.techn. **Michael Harasek**
Assistant Prof. Dipl.-Ing. Dr.techn. **Walter Wukovits**

Wien, _____ _____ _____
(Unterschrift Verfasserin) (Unterschrift Betreuer)

ABSTRACT

The presented mathematical model offers a comprehensive depiction of the basic oxygen steelmaking process, capturing various factors that influence the refining reactions in the converter. It is based on a well-established multi-zone reaction interface kinetic modelling approach. Two key adaptations set this model apart from existing literature: a meticulous investigation of diffusion coefficients for refining rate description, employing coefficients measured in liquid and gas phases for liquid-liquid and liquid-gas interfaces, respectively, leading to improved predictions; and a detailed analysis of droplet behaviour, incorporating the effect of ash production. The model's validation results demonstrate its accuracy, aligning well with measured data and predictions by other research teams. The insights gained from this model have the potential to optimize the steelmaking process, allowing for the use of raw materials of lesser quality, efficient flux addition planning based on refining state, and customized furnace and lance geometry design.

KURZFASSUNG

Das präsentierte mathematische Modell bietet eine umfassende Darstellung des Stahlherstellungsprozesses im Konverter, welches verschiedene einflussreiche Faktoren erfasst, die die Oxidationsreaktionen im Konverter beeinflussen. Es basiert auf einem etablierten kinetischen Modellierungsansatz für Mehrzonen-Reaktionsgrenzflächen. Zwei wesentliche Anpassungen unterscheiden dieses Modell von bestehender Literatur: eine sorgfältige Untersuchung der Diffusionskoeffizienten zur Beschreibung der Verfeinerungsrate, wobei Koeffizienten gemessen in flüssigen und gasförmigen Phasen für flüssig-flüssige bzw. flüssig-gasförmige Grenzflächen verwendet wurden, was zu verbesserten Vorhersagen führte; und eine detaillierte Analyse des Tropfenverhaltens, die den Effekt der Aschebildung einbezieht. Die Validierungsergebnisse des Modells belegen dessen Genauigkeit, da sie gut mit gemessenen Daten und Vorhersagen anderer Forschungsteams übereinstimmen. Die gewonnenen Erkenntnisse aus diesem Modell haben das Potenzial, den Stahlherstellungsprozess zu optimieren. Sie ermöglichen den Einsatz von Rohstoffen minderer Qualität, eine effiziente Planung von Flussmittelzugaben basierend auf dem Verfeinerungszustand und eine maßgeschneiderte Gestaltung von Ofen- und Lanzengeometrien.

TABLE OF CONTENTS

1 INTRODUCTION

Steel is a fundamental material which is strongly linked to the economic development, and characterized by its strength, formability as well as a vast variety of other remarkable properties and functions.

The production and use of steel have a significant global impact. According to the data provided by the world steel association [1], no country has achieved high incomes per capita without significantly increasing its steel consumption. As humanity continues to strive for economic advancement, it is reasonable to expect that steelmaking will at least maintain its importance, if not amplify it. However, it is important to acknowledge that the iron and steel industry (ISI) is one of the largest CO_2 emitters among heavy industries. The International Energy Agency (IEA) [2], states that approximately 7% of total energy system emissions stem from the ISI. Therefore, there is a strong emphasis on reducing the CO_2 emissions in the steelmaking route. These efforts include the utilization of renewable energy sources, carbon capture and storage (CCS) technologies, the use of hydrogen and the development of more energy-efficient processes through process simulation and in-depth unit operation simulations.

Numerous studies have been conducted to identify the production stages that have the most significant negative impact on CO_2 emissions in the steelmaking process. Typically, the coking plant is regarded as the largest source of CO_2 emissions, followed closely by the blast furnace and lastly the basic oxygen furnace.

In terms of energy consumption, ironmaking exhibits the highest primary energy intensity, followed by primary steelmaking, and finally tertiary steelmaking. When comparing the aforementioned steelmaking routes, it is observed that the Electric Arc Furnace (EAF) consumes approximately 4-6 times more energy than the Basic Oxygen Furnace (BOF) [3]. However, the BOF emits significantly more CO_2 than the EAF. Synoptic both routes have considerable drawbacks offering ample opportunities for research and optimization. Nevertheless, due to the large-scale production of steel, conducting real-time experiments to approximate improvements in operating parameters is impractical. This is where process

simulation and detailed unit-operation simulation come into play, enabling the exploration of potential enhancements in a more feasible manner.

It is crucial to recognize that not everything can be measured directly in the steelmaking process. This is where process simulation plays a pivotal role, allowing for the gathering of insights into the process and facilitating a deeper understanding of its dynamics, optimization potential, and environmental impact.

Process simulation aims to construct a graphical representation or flowchart of the workflow, depicting individual steps and providing a comprehensive overview of all unit operations involved. These unit operations are represented by mathematical models that incorporate their primary chemical, physical, and technical aspects. This approach offers a clear visualization of the workflow, which can be analyzed to improve efficiency, enhance transparency, and establish best practices by ensuring consistency and standardization. Furthermore, process simulation provides a concise and user-friendly summary, making it easily understandable for stakeholders and facilitating effective communication and decision-making processes.

This thesis focuses on the modeling and optimization of a key unit operation in primary steelmaking: the basic oxygen furnace (BOF). The primary objective is to develop a comprehensive, dynamic, and multizone kinetic model that can serve as a stand-alone tool for calibration of existing black box models. Additionally, this research aims to enhance the understanding of the physiochemical phenomena that take place during the BOF process, particularly in relation to the operating parameters. By gaining deeper insights into these phenomena, it becomes possible to achieve a more environmentally friendly operation of the process, reducing energy and resource consumption.

2 BASIC OXYGEN STEELMAKING

The steelmaking process can generally be divided into two main parts: the production of iron from iron ore (referred to as “ironmaking”), and the production of steel from iron (referred to as “steelmaking”). In Europe steel is produced predominantly via two basic routes: either the blast furnace (BF) – basic oxygen furnace (BOF) route or the electric arc furnace route (EAF). Figure 2-1 depicts both steelmaking processes [4]. However, the most common production method is the BF-BOF route and thus will be elaborated in more detail.

Figure 2-1 Overview of the steelmaking process [4]

Throughout the first part the raw materials iron ore, coke, and limestone are fed into the top of the BF, while hot air and pulverized coal (optional) are blasted into the bottom. The heat and pressure inside the furnace cause the reduction of iron oxide to elemental iron.

The second part of the steel production is further divided into three phases: the primary, secondary and tertiary production phase. Primary steelmaking involves smelting iron into steel, during the second phase alloying elements or gases are added or removed and lastly the tertiary steelmaking includes forming processes such as casting into sheets, rolls or other forms.

This chapter will provide a detailed insight into the BOF unit operation. The subchapters will cover the historical background, a description of the physical structures needed to perform

the process and the process steps. This description is of importance to later understand the boundary conditions chosen for the model and simulation of this unit operation.

2.1 History of Basic Oxygen Steelmaking

The central concept of converter processes for steelmaking is the conversion liquid, carbon-rich, hot metal from the blast furnace to low-carbon steel [5]. The historical roots of this process can be traced back to the late 1800s, when refining was achieved through the "bottom blow" technique, involving blowing air through tuyeres at the bottom of the converter, also known as OBM (Oxygen Bottom Blowing) or Q-BOP (Quiet-Bottom Oxygen Process). However, the use of air for the blow resulted in a high nitrogen content, which affected the steel quality negatively. Although the beneficial effects of blowing pure oxygen in steel refining were well-known, there was no economic method to produce pure oxygen at that time. This challenge was overcome in the 1920s, not only marking a significant milestone in the development of the process but also revealing the next key problem – extreme wear of the bottom and tuyere area.

The breakthrough and next step in the developmental history of the process occurred in Linz and Donawitz Austria, with the introduction of the "top blow" technique, also known as BOF (Basic Oxygen Furnace) or BOP (Basic Oxygen Process). In this method, oxygen was blown into the converter through a water-cooled lance lowered through the vessel mouth, bypassing the issues associated with bottom wear.

Over time, the process conditions underwent changes, including variations in the gases blown through the top and/or bottom, as well as modifications of the geometries of the tuyeres and the top lance. These changes resulted in a variety of different methods, as depicted in Figure 2-2 [6]. Presently, most converters employ a hybrid process consisting of top and bottom blow, which will also be incorporated into the mathematical model in later chapters.

Over the course of the past 150 years, extensive research and development efforts have transformed this process into one of the most successful methods for producing crude steel [7]. Approximately 70% of all crude steel is now produced using BOF technology. This approach offers several advantages over alternative methods such as the electric arc furnace, including the ability to produce high-quality steel while maintaining high productivity and efficient utilization of raw materials.

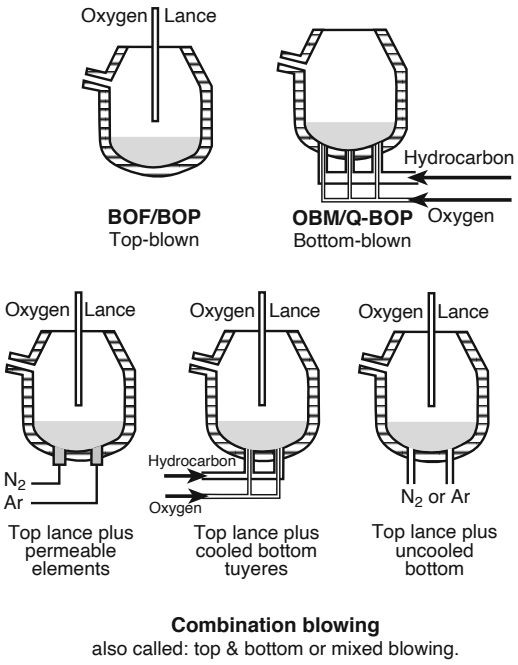

Figure 2-2 Depiction of different converter types [6]

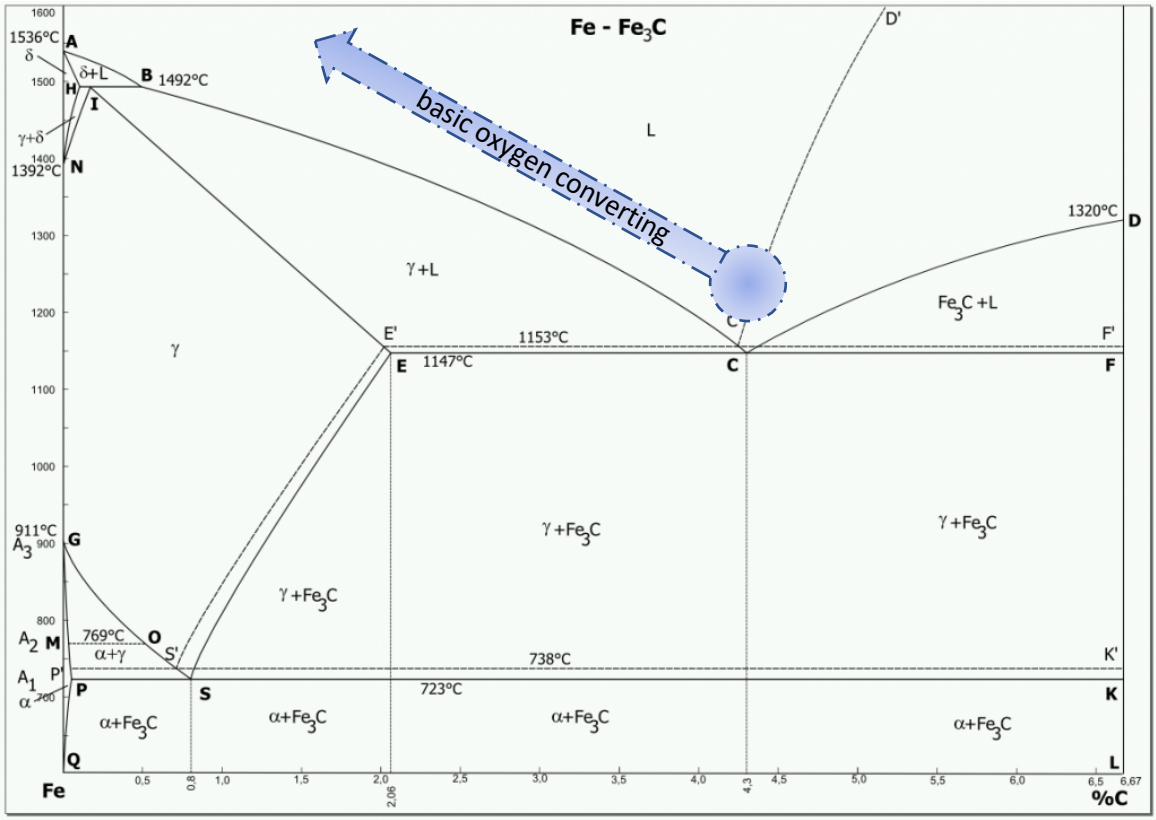

Figure 2-3 Oxygen converting in respect to the binary phase diagram Fe-C [8]

Figure 2-3 schematically depicts the evolution of the basic oxygen furnace process within the binary phase diagram of iron and carbon, showcasing the relationship between the concentration of carbon and the corresponding phase composition of the steel during the

refining process. However, in reality the qualitative progress of carbon removal is not strictly linear. Various factors, such as temperature, residence time, and the composition of the steel, can influence the kinetics of the reactions and the subsequent phase transformations. The complexity of these physicochemical phenomena underscores the need for detailed modelling and optimization approaches to enhance the understanding and control of the process.

2.2 Process

Basic oxygen steelmaking is a six-step batch process, as depicted in Figure 2-4. The first step (1) involves charging the empty furnace with scrap, which constitutes approximately 20% of the total metallic charge and serves as the second-largest source of iron. The scrap mainly consists of recycled iron or steel, such as rails. While its primary purpose is energy consumption, it also contributes to a decrease in temperature during the subsequent exothermic oxygen blow.

In the second step (2), hot metal is poured onto the scrap. The composition of the hot metal can vary greatly, typically the charge contains [6]: Carbon 4 – 4.5 [wt%], Silicon 0.3 – 1.5 [wt%], Manganese 0.25-2.2 [wt%], Phosphorus 0.04-0.2 [wt%], Sulphur 0.03-0.08 [wt%].

The third step (3) involves lowering of the lance into the vessel, preparing for the oxygen blow. During the fourth step (4), known as the “main blow”, oxygen is blown onto the hot metal bath. This step facilitates the oxidation of impurities, allows for sample collection, and involves the addition of fluxes (e.g., iron ore, lime, dolomite, fluorspar). The duration of this step is usually between 15 and 22 minutes. The charge undergoes three main refining periods.

Throughout the first period the majority of the oxygen is consumed by the oxidation of minor elements such as silicon, manganese, phosphorus, titanium, vanadium, while the carbon content decreases approximately linearly. As the hot metal bath reaches the critical carbon content, the mass transfer of dissolved carbon becomes the rate-limiting step, which characterizes the second period. During the third period carbon is no longer able to reduce all the formed iron oxide (FeO), which leads to a rapid increase of FeO content in slag.

Lastly, the fifth (5) and sixth (6) steps involve tapping the steel and slag from the furnace, respectively.

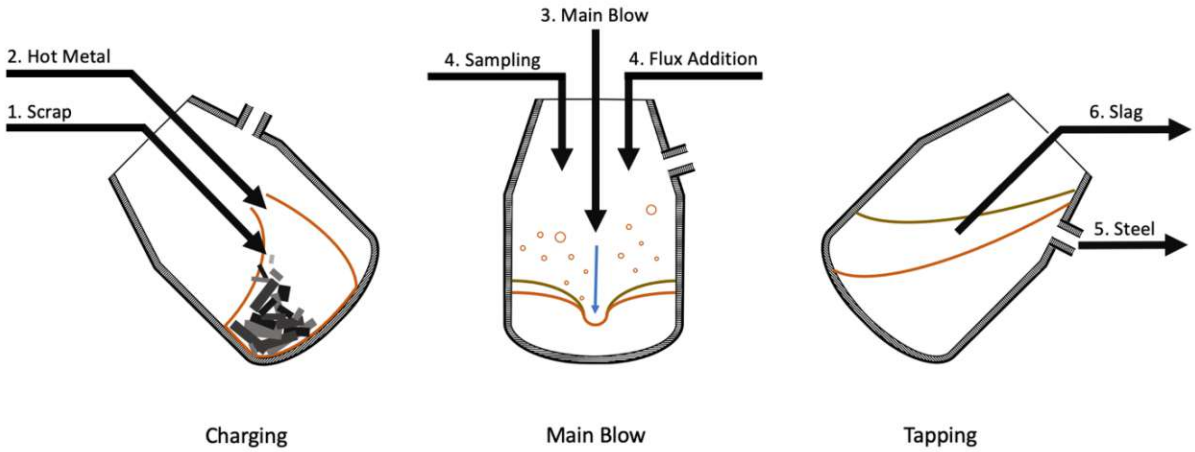

Figure 2-4 BOF six step batch process

The charging procedure of a furnace is depicted in Figure 2-4. The figure illustrates schematically one blow and the sequential introduction of fluxes and iron ore during the process, along with the sculling of the lance and the varying oxygen flow rates over time. Possible sampling points are also depicted. They are needed to ensure the that the goals of the refining procedure are met.

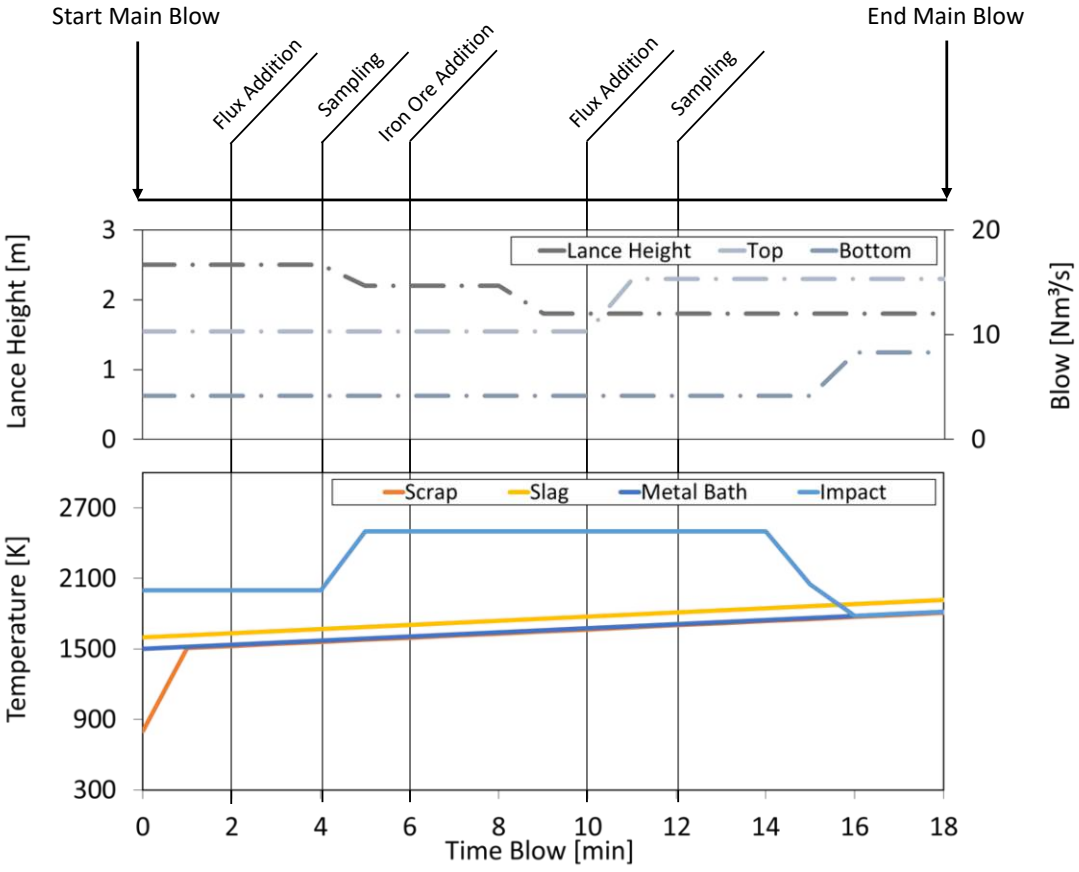

Figure 2-5 Schematic representation of one blow

2.2.1 Basic Oxygen Furnace

The furnace used consists of a vertical vessel, lined with basic refractory as it is schematically shown in Figure 2-6. The basic refractory or working lining, acts as a barrier enduring the harsh conditions within the furnace during a blow. It is of great interest to preserve the refractory lining, and thus lengthen the lifespan of the furnace. To reduce chemical wear of the working lining magnesium oxide (MgO) is added to the slag until saturation limit. Further, keeping the iron oxide (FeO) content in the slag as low as possible minimizes corrosion effects.

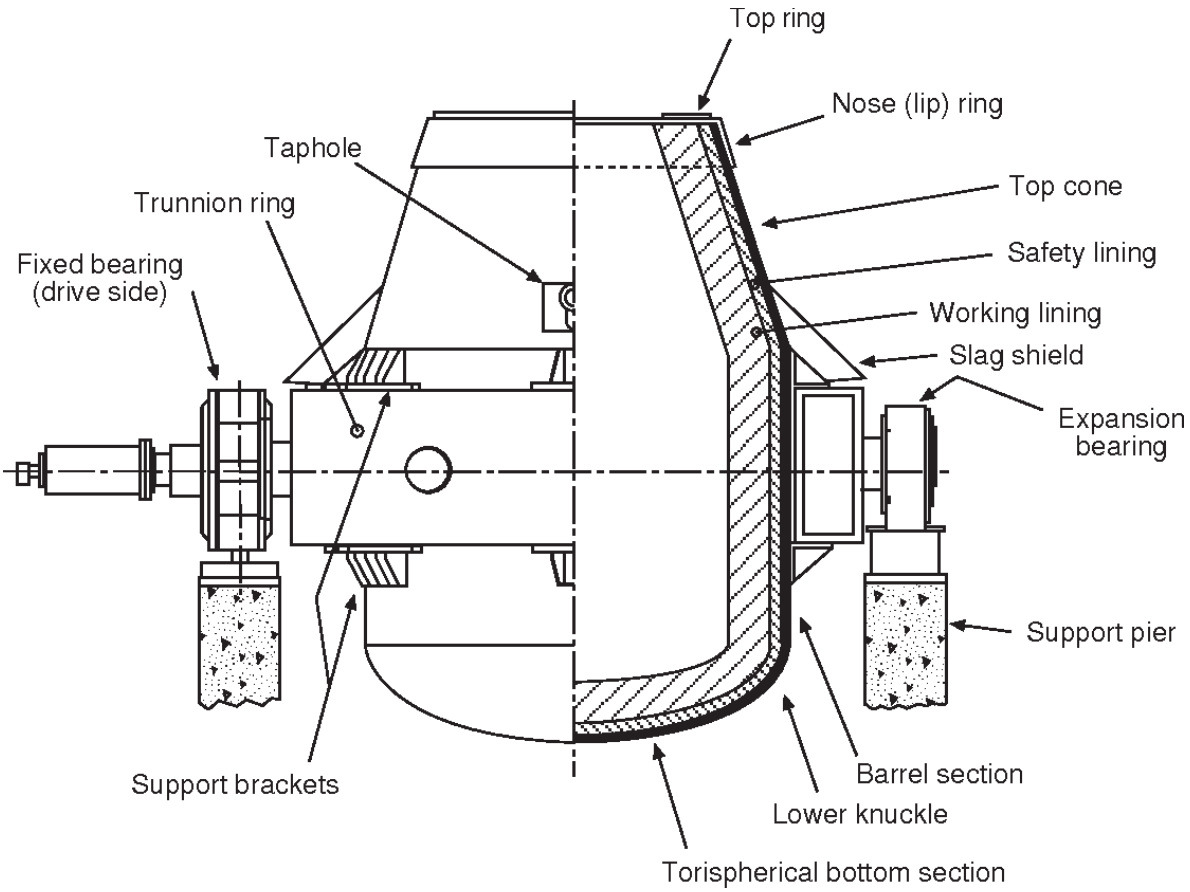

Figure 2-6 Basic Oxygen Furnace Vessel [9]

Typically, converter vessels contain between 50 to 400 tons of hot metal and scrap. They are designed in a way that the volume occupied by the charge is approximately 20% of the converters volume. The working volume might seem relatively little, but the converter must be tilted during the process without spilling its content for example for sampling or to be charged with raw materials. Furthermore, the phenomena of foaming and splashing due to the blowing occur which should be contained by the vessel [9].

2.2.2 Top Blow

The top blow is realized by using a water-cooled lance, its design and blowing program are crucial to the evolution of the process. An example of such a lance is depicted in Figure 2-7. Several parameters have a significant impact, such as the number of nozzles (holes in the lance tip), nozzle geometry, lance height, and blowing velocity. These parameters influence the rate and oxidation order of iron ore constituents, iron droplet splashing, slag foaming, droplet emulsification in the slag and postcombustion of carbon monoxide (CO). Typically, a lance has 4-7 nozzles, through which supersonic jets are formed [10].

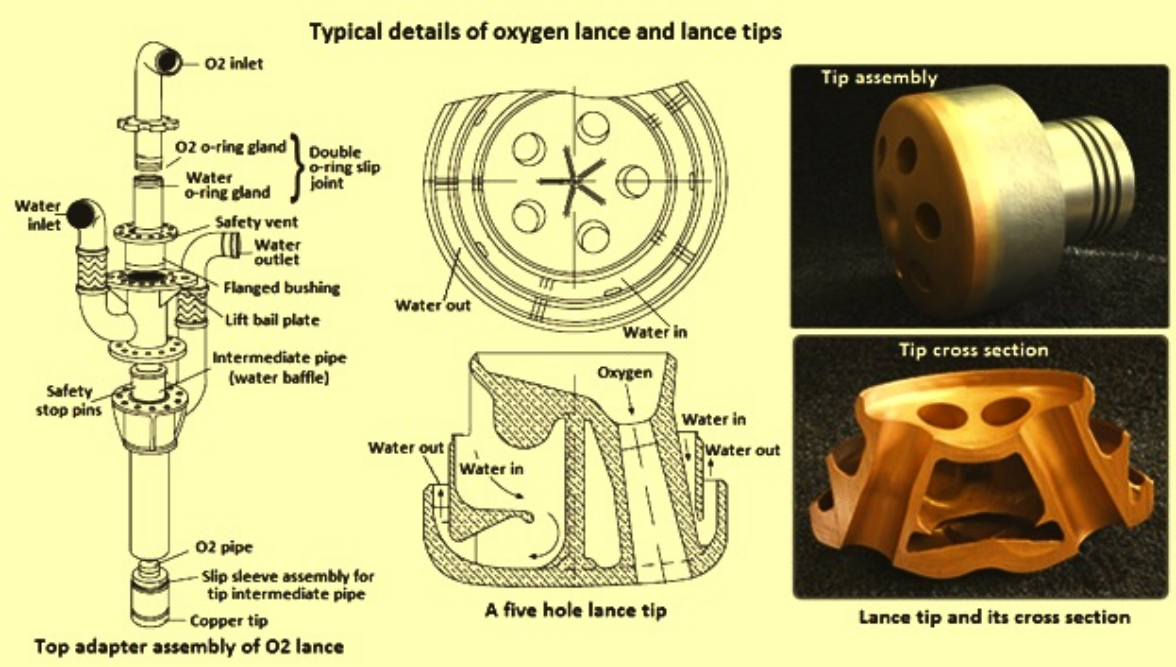

Figure 2-7 Schematic representation of top blow lance [11]

2.2.3 Bottom Blow

To further enhance the refining process and increase stirring of the metal bath, a technique known as "bottom blow" is practised, which involves injecting gas from the furnace's bottom. There are various devices that can be installed, and generally, the ease of maintenance is inversely proportional to the level of stirring benefits achieved [6]. The simplest form of bottom blowing device would be a porous plug or permeable element as depicted in Figure 2-8. These do not require gas pressure to be maintained when the bottom stirring is off, as the hot metal cannot penetrate them. However, the stirring effect obtained by using them is very little, because only a limited amount of gas can permeate through one plug.

A more complex method to conduct the bottom involves the use of tuyeres, which enhance the stirring performance. However, they can become blocked if the gas flow rate is not properly maintained or if there is a build-up at the bottom of the furnace. To mitigate the drawbacks of each method, different devices and techniques can be combined.

In bottom blowing, either argon or nitrogen gas is used. Due to argon gas being cheaper it is used in the beginning to prevent the bottom stirring elements from clogging, whereas nitrogen gas is used during the blow depending on the type of steel. It is important to note that oxygen cannot be used for bottom blowing due to the heat generated by oxidation reactions. The use of oxygen would significantly shorten the lifespan of the bottom stirring elements, rendering them economically unfeasible.

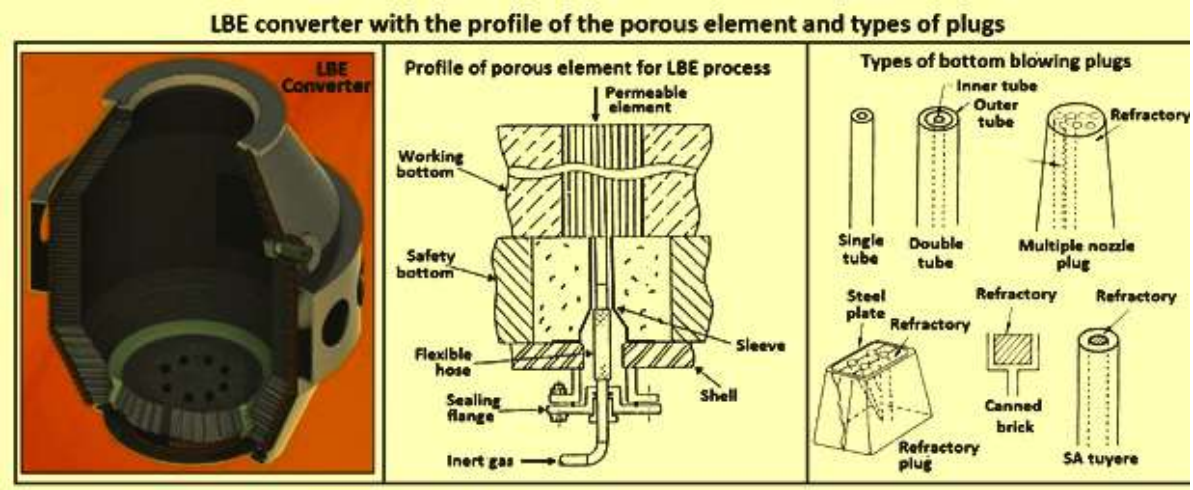

Figure 2-8 Schematic representation of bottom blow [12]

2.3 Process Phenomena

There are numerous mechanical and thermal phenomena as well as a complex combination of chemical reactions occurring during the main blow. The following list will give an overview of the most important ones for the mathematical modelling of the process:

1. Blowing through the lance, “top blow”, causes slag foaming, splashing, and stirring
2. Blowing through the bottom, “bottom blow”, stirs the metal bath and thus the reaction surfaces are renewed constantly
3. Oxidation reactions progressing simultaneously whilst intensively producing and consuming heat
4. Creation of slag which changes its composition over the blow time
5. Heat transport and loss by gas/dust flow
6. Scrap melting and metal bath cooling
7. Heating and melting of different fluxes, in particular: lime, dolomite, iron ore

3 State of the Art Basic Oxygen Furnace Model Review

Modelling of the basic oxygen furnace process, for in-line process control and fundamental research has gained great importance over the past few decades, due to it becoming the most common way of producing crude steel. A vast number of different models can be found in literature. Notably, there is a trend towards integrating fundamental physiochemical relations and not solemnly base the model on statistics or machine learning. Extensive studies and discussions on the various models have been conducted by Lotte De Vos et. al [13]. This chapter aims to provide an overview of the different modelling approaches.

In general, there are two distinct approaches to construct a dynamic BOF model: mathematical or statistical as presented in Figure 3-1. The mathematical model is based on physiochemical relations, whereas the statistical model is purely based on industrial data and statistical methods. However, due to the high complexity of the process some of the later presented mathematical models use a certain amount of empirical data to fit model parameters.

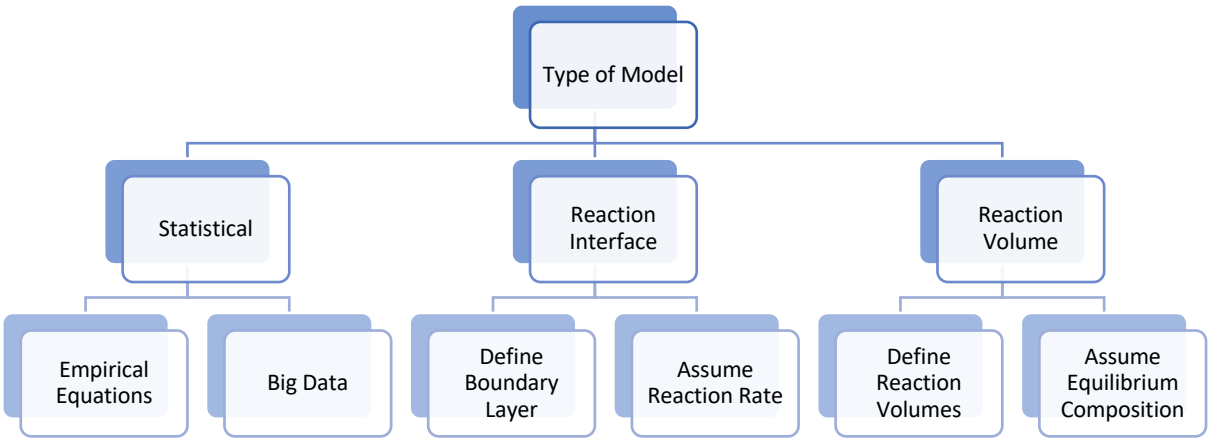

Figure 3-1 Overview of model types

Statistical models have demonstrated excellent predictive capabilities. However, these predictions are limited to a specific furnace for which measurements are available to compile the training dataset. Thus, making this approach not applicable to different furnaces. A further drawback would be that the amount of data sets needed to train such a model is

extremely high (at least a couple of thousand measurements must be conducted, categorized and evaluated).

Mathematical models can be categorized into two types: reaction interface-based and reaction volume-based as presented in Figure 3-2.

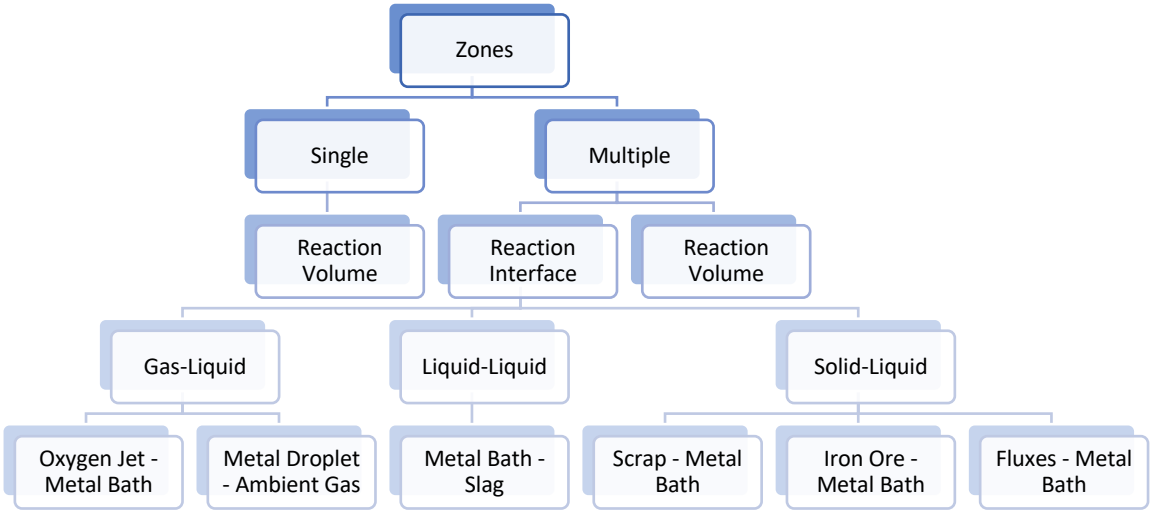

Figure 3-2 Overview of zone types

The reaction interface approach focuses on the dynamic interaction between two phases along an interface e.g., liquid-liquid interface (slag-metal zone) or gas-liquid interface (impact or emulsion zone) describing the rate of reaction by assuming the resistance against mass transfer in the diffusion boundary layers. This type of modelling relies on partial differential equations (PDEs), which are able to describe mass, momentum and energy transport at a chosen interface. This opens the possibility for a detailed description of variations in reaction rates and temperature gradients across different interfaces. It allows to factor in changes in slag composition, temperature, addition of fluxes as well as other additives and gas flow rates over time which impact the governing reaction rates drastically [13].

The reaction volume model [14], [15], on the other hand, treats the entire vessel as a single well-mixed volume, assuming that the active volume achieves equilibrium composition at every time step. There have been efforts to subdivide the black box style volume into more interacting reaction volumes to increase the detail [13]. However, in general, this model does not focus on the detailed interface dynamics, it considers an averaged representation of the system. The reactions are assumed to occur uniformly throughout a homogeneous volume, neglecting local concentration and temperature variations, and the model mainly emphasizes

overall mass and energy balances. It provides a macroscopic view of the BOF process, making it suitable for understanding bulk behaviour and large-scale kinetics. This type of modelling typically relies on ordinary differential equations (ODEs) to represent the overall mass and energy balances within the system.

The key distinction between the reaction interface model and the reaction volume model in basic oxygen steelmaking stem from their respective levels of detail in capturing localized reactions, mass transfer, and spatial variations. The reaction interface model accounts for local variations and phenomena at the interfaces, while the reaction volume model considers a homogenized representation of the entire vessel.

Moreover, the models can be subdivided depending on how detailed they depict the basic oxygen steelmaking process. These distinctions encompass various aspects such as the representation of impurities, additives, and the adaptability of the model concerning the dynamic changes in operational parameters over time.

Notably, how, where and the degree to which impurities are effectively oxidized and refined during a single blow significantly influences the quality of the produced steel. Thus, a comprehensive inclusion of impurities in the model enables a more profound understanding of optimizing steel production. This not only results in energy and cost savings but also ensures an optimal utilization of produced gases and resources charged into the converter during the blow. The most prevalent impurities modelled through refining reactions are summarized in Figure 3-3.

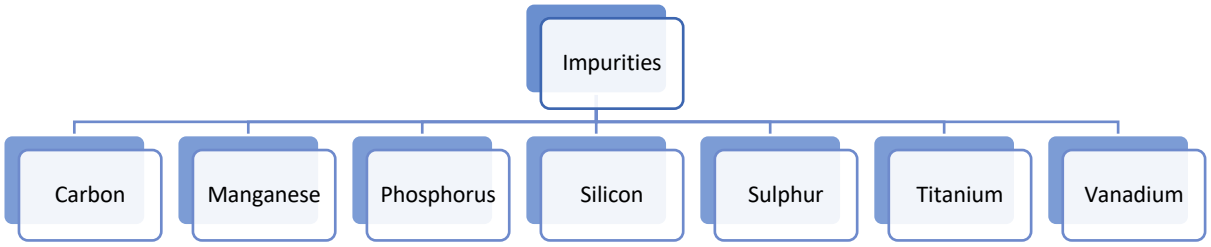

Figure 3-3 Most significant impurities in basic oxygen steelmaking

Research indicated that additives such as scrap [16], iron ore [17], and various fluxes play a significant role in influencing the temperature profile of the hot metal bath and the composition of slag within the basic oxygen furnace. Consequently, these factors profoundly

impact the oxidation process of impurities. Based on these findings most models in literature incorporate melting and dissolution submodels.

Furthermore, to capture the complexities of the real-world process effectively, the model's adaptability concerning dynamic changes in operational parameters over time, such as lance height, sample taking, charging of additives and fluxes, and blow duration, is crucial. This adaptability ensures that the model can emulate the time dependent nature of the industrial operation accurately. The models that factor in the changes in operation parameters with respect to time are called dynamic models and are the counterpart to static black box models.

The literature research conducted, and the model aspects presented in this chapter were built upon a comprehensive review paper authored by Lotte De Vos et al. [13] which provides an extensive compilation of models that aim to depict the basic oxygen furnace process.

To create a comprehensive overview of possible modelling approaches, the models mentioned in [13] were summarized and extended by further physiochemical and statistical models found in literature. The summary is presented in tabular form and is provided in the Appendix, 12.1 Model summary. It encompasses the following aspects: model type, number of reaction zones, integration of thermodynamics and kinetics, temperature and impurities. While most of these attributes are self-explanatory, there are two that need further elaboration: temperature and impurities. "Temperature" pertains to whether the temperature evolution during the process is imposed or modelled using an energy balance calculation. "Impurities" refers to the number and type of constituents that are considered in modelling the refining process. The existing BOF models were evaluated, and the key findings, modelling approaches, submodels, and boundary conditions were summarized in a decision tree. The decision tree was subsequently discussed with experts to identify the most promising and useful modelling approaches.

4 DYNAMIC MULTIZONE MODEL

The primary objective of this thesis is to provide a comprehensive understanding of the phenomena occurring during a blow in the basic oxygen furnace (BOF) process using a mathematical model. To achieve this, a multi-zone approach that allows for a detailed depiction is considered the most appropriate. In order to identify the optimal number and locations of critical reaction zones, an extensive literature research was conducted. The foundation for this research was the work by Lotte De Vos et al. [13], as it provides a description and comparison of physiochemical BOF models which were summarized and extended as presented in the Appendix 12.1 Model summary.

Upon comparing different modelling approaches, the work of Dogan et al. ([18], [16], [17], [19]), Rout et al. [20] and Dering et al. [21] particularly stand out due to their excellent predictions and the impressive amount of detail. Drawing inspiration from the publications of these researchers, an outline for the model was conceptualized.

The chosen approach for modelling the unit operation was implemented in gPROMS Process, a comprehensive process simulation software. The program was chosen with the intention of using the model as a stand-alone tool to not only calibrate existing black box models but also to deepen the understanding of the BOF unit operation. By utilizing gPROMS Process, it is possible to incorporate detailed physicochemical relations and capture the process dynamics, thereby enhancing the accuracy and reliability of the model. This integrated approach makes it possible to study optimization strategies and provide valuable insights for improving the efficiency and environmental sustainability of the BOF steelmaking process.

The novelty presented in this thesis lies in the programming and implementation of a dynamic model into a model library that consists of static models, using the gPROMS Modelbuilder® and gPROMS Process®. Furthermore, the number of submodels in this thesis exceeds those presented by previous research groups, allowing for a more in-depth depiction of the process. Additionally, certain submodels have been modified and optimized in collaboration with experts to enhance their accuracy and effectiveness.

4.1 ASSUMTION

The modelling process required making certain assumptions, which are outlined as follows:

1. Temperature Profiles: The temperature profiles for different zones within the converter are imposed based on established literature sources Figure 4-1.

    - Hot metal bath: For the hot metal bath, the starting temperature is the charge temperature of the hot metal, which then increases linearly until it reaches the end point temperature. The end point temperature, which is determined by the chosen slope of the linear progression, is derived from empirical correlations.

    - Slag: The temperature profile is assumed to be 100°C higher and parallel to the one of the metal bath.

    - Impact Zone (Impact): It is assumed that the maximum temperature of 2500K is reached within the first 20% of the blowing time. During the last 20% of the blow, the temperature decreases linearly until it reaches the end point temperature. This decrease is attributed to the oxidation reactions of impurities being mostly completed during this stage.

    - Droplet: For the ejected droplets, correlations have been imposed which describe the changes in temperature with respect to the residence time in the emulsion zone.

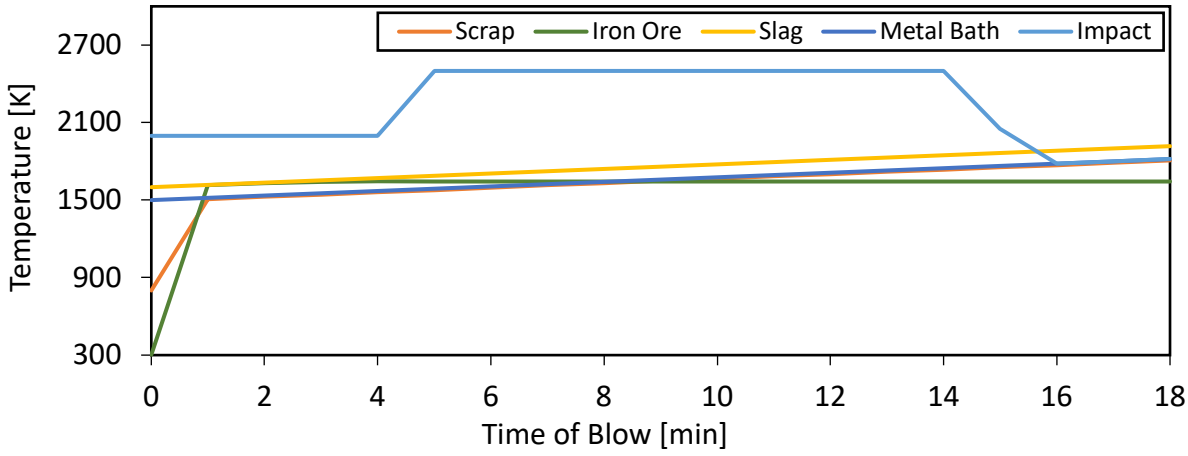

Figure 4-1 Imposed temperature profiles

2. Slag composition: Due to the complex nature of its development, the change in slag composition over time is imposed mostly based on the work of [5] which is presented in Figure 4-2. However, after reviewing data found in literature as well as measured industrial data the evolution of the slag composition was adapted as depicted in Figure 4-3.

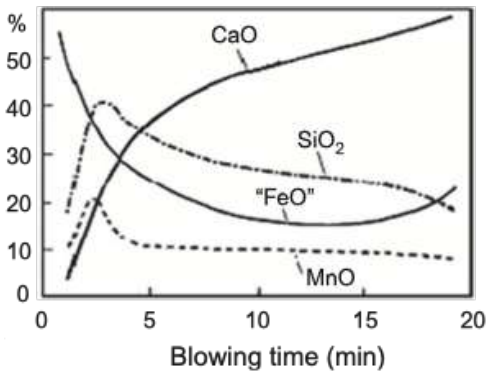

Figure 4-2 Slag composition as proposed by [5]

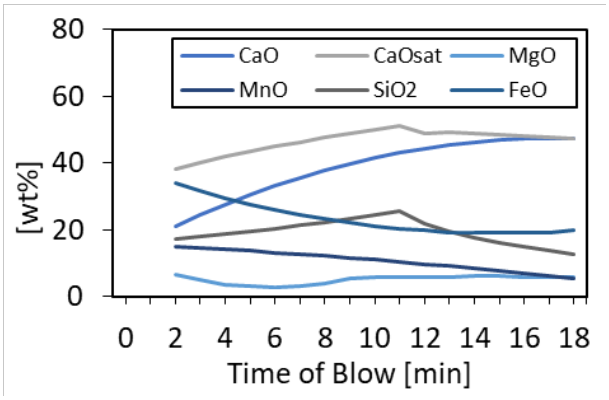

Figure 4-3 Imposed evolution of slag composition

3. Fluxes: The added fluxes are assumed not to change the composition or temperature of the slag or the hot metal bath. However, they do affect the mass of the hot metal bath.

4. Viscosity: Change in slag and hot metal viscosity is considered and depends on the operating parameters.

5. Droplet motion: The ballistic motion of each droplet is taken into account.

6. Bloated droplet theory: The bloating droplet theory and its impact on the droplet motion is considered.

4.2 Final Model Concept

Following an in-depth review of the existing literature, which is summarized in the Appendix 12.1 Model summary, a model outline was created. The modelling decisions and main phenomena modelled can be summarized as follows:

1. The model is based on the reaction interface approach and consists of three main reaction interfaces: impact zone, slag metal zone and emulsion zone Figure 4-4.

   a. The impact zone is situated in the impingement point of the oxygen jet and the hot metal bath.

b. The slag metal zone describes the interface between the hot metal bath and the slag.

c. The emulsion zone consists of a summation of the surface area of all hot metal droplets, which are ejected from the hot metal bath.

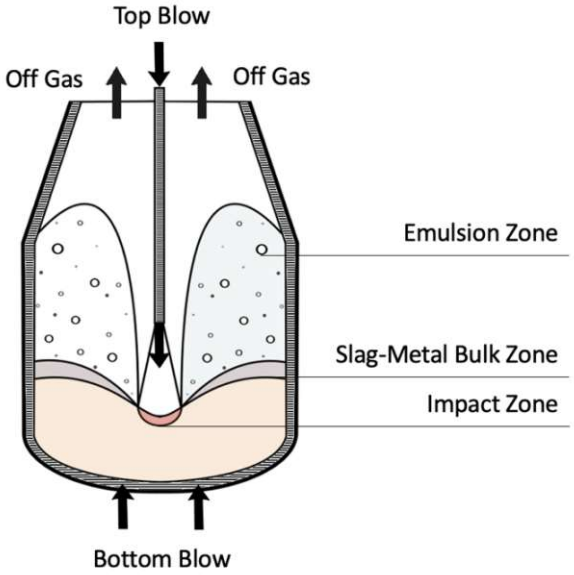

Figure 4-4 Schematic representation of the reaction interfaces

2. The impurities considered during the refining process are: carbon, silicon, phosphorus, manganese.

3. The impact of lance geometry and height on the process is considered. It is possible to choose the number of nozzles as well as a dynamic lance height.

4. The stirring and surface renewal effect due to the top blow.

5. The bath stirring effect of the bottom blow, which is dependent on the number of tuyeres.

6. The scrap melting process is simulated in two ways. If the user has detailed knowledge on the scrap geometry and composition a particularized method for the melting process can be chosen. However, if there is limited knowledge on the scrap a less detailed melting model is implemented.

7. The melting of different fluxes as iron ore, dolomite and limestone is implemented. The user can choose how much and at what point in time these fluxes are added.

4.3 ALGORITHM

Figure 4-5 showcases the step-by-step process the algorithm follows to compute the different model phenomena previously listed that are part of the equation-oriented system.

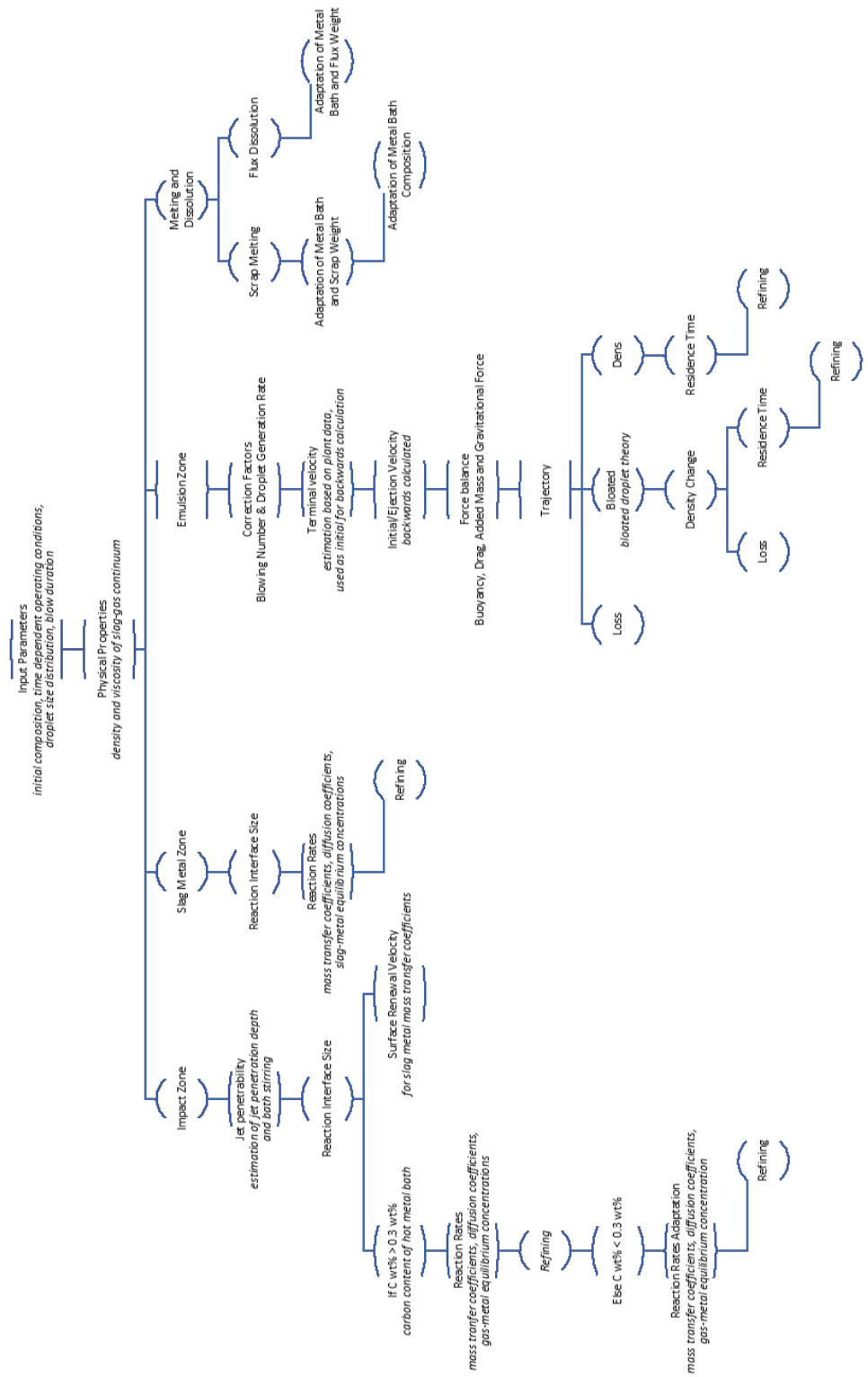

Figure 4-5 Algorithm

5 RATE PHENOMENA

This chapter is strongly influenced by the work of Turkdogan [22], who has made significant contributions to the field of iron and steelmaking. His expertise lies in the development of mathematical models, simulation techniques, and optimization of steelmaking processes. His work has focused on the development of mathematical models for various steelmaking processes, including the basic oxygen steelmaking process, the electric arc furnace process, and the continuous casting process. Turkdogan's contributions have been widely recognized through publications in esteemed peer-reviewed journals and conferences. Additionally, he has collaborated on industrial projects related to the optimization of steelmaking processes. In the forthcoming chapters, the refining reactions modelled as well as their theoretical background will be discussed in detail.

5.1 THEORETICAL BACKGROUND

A vast variety of rate phenomena must be considered when modelling a BOF. This work mainly deals with chemical forward and backward reactions, mass transfer via diffusion and heat transfer. To be able to depict the chemical reactions taking place during a blow two different approaches have been established by researchers. The reaction interface modelling approach and the reaction volume modelling approach. The basis for these approaches is the knowledge of the concentration of the individual constituents and their diffusion coefficients.

After identifying the reactions that are a key component in realizing a BOF model which are summarized in the Appendix, 12.1 Reactions Modelled, the governing equations describing these refining reactions across the chosen reaction interfaces were formulated. It has been suggested by various research groups ([13], [23], [20]) that first-order rate equations describe the refining reactions in enough detail, thus this approach was adopted for the model and will be elaborated in more detail.

5.1.1 First-order Rate Equations

First-order rate equations describe the rate of change of the concentration of a reactant or a product in a chemical reaction. The rate of the reaction is solely dependent on the concentration of the reactant. The general form of a first-order rate equation is:

$$-\frac{d[A]}{dt} = k[A] \qquad \text{Eq. 1}$$

Where $\frac{d[A]}{dt}$ represents the rate of change of the concentration of the reactant A, k is the rate constant, and [A] is the concentration of the reactant. The negative sign indicates that the concentration of the reactant is decreasing over time. The rate constant k is a measure of the speed of the reaction, and it has the unit of time^{-1}. As it is determined experimentally its value is specific to the reaction taking place and the conditions under which it is performed.

5.1.2 Fick's Laws

Further Fick's laws of diffusion need to be considered for the mathematical description of the phenomena taking place in the converter. Fick's laws of diffusion aim to mathematically describe the diffusion process, which is the transport of particles from regions of higher concentration to regions of lower concentration. The laws were first proposed by physicist Adolf Fick in 1855 and are based on the assumption that the rate of diffusion is proportional to the concentrations gradient.

The first law, states that the diffusion flux (J) is proportional to the concentration gradient (-dC/dx), where C is the concentration of the diffusing species, x is the position and J has the units of concentration per unit area per unit time (e.g. mol/m^{2}s). Mathematically, it can be expressed as:

$$J = -\frac{dC}{dx} = -D\nabla C \qquad \text{Eq. 2}$$

Where D is the diffusion coefficient, which is a measure of the ease with which a species diffuses through a medium and ∇C is the concentration gradient.

The second law, states that the rate of change of concentration with respect to time (dc/dt) is proportional to the second spatial derivative of the concentration with respect to position (d^2c/dx^2).

Mathematically, it can be expressed as:

$$\frac{dC}{dt} = -D\nabla^2 C \qquad \text{Eq. 3}$$

It's important to note that these laws are only valid for systems in which the diffusion process is described by a linear partial differential equation and when the diffusion is isotropic, i.e., the diffusion coefficient is independent of position. In addition, it is also important to note that Fick's laws assume no chemical reaction is taking place and that the diffusion is due to the thermal motion of the particles.

5.1.3 Diffusion Coefficients

In general, the diffusion coefficient characterizes how much mass of a substance diffuses over a certain time span through a unit surface at a concentration gradient of unity. In the theory it is usual that the diffusion coefficient is independent of concentration, when examining melts [24].

The diffusion coefficient of a solute in a melt is a fundamental quantity required to characterize mass-transport rates. However, there is a variety of arising difficulties and uncertainties when it comes to the accuracy of measuring diffusion coefficients in liquid metals at medium and high temperatures. The main obstacle is the occurrence of natural convection which causes bulk motion of the fluid and thus mass transport. There are different methods for measuring the diffusion coefficient of a species in metallurgical applications, each with its own advantages and disadvantages [24]. Some of the common methods, which are the basis for the diffusion coefficients used in this study, include:

1. The isotopic tracer method: This method involves introducing a small amount of an isotopically labelled species into a sample, and then measuring the concentration of the tracer species as a function of time and position. The diffusion coefficient is then calculated by fitting the concentration profile to a diffusion equation.

2. The electrochemical method: This method involves measuring the current flowing through a sample as a function of time and position, as the species diffuses through the sample. The diffusion coefficient is then calculated by fitting the current profile to a diffusion equation.
3. The thermal diffusion method: This method involves measuring the temperature profile of a sample as a function of time and position, as the species diffuses through the sample. The diffusion coefficient is then calculated by fitting the temperature profile to a diffusion equation.

It's important to note that these laws are only valid for systems in which the diffusion process is described by a linear partial differential equation and when the diffusion is isotropic, i.e., the diffusion coefficient is independent of position. In addition, it is also important to note that Fick's laws assume no chemical reaction is taking place and that the diffusion is due to the thermal motion of the particles.

To fine tune the mathematical model, various diffusion coefficients used in other converter models were gathered and their impact on the calculation results of the model was investigated. An overview of the diffusion coefficients is given in Table 1, as is obvious from comparing them, they differ gravely. The most commonly used diffusion coefficients are based on the experimental application of capillary methods by Goldberg and Belton [25], Kawai and Mori [26] and Grace [27]. However, the investigators all point out a number of drawbacks using these methods. For example, unfavorable temperature gradients, mechanical effects or differences in density can easily cause convection which distorts the measurements. To minimize the source of error the diameter of the capillary used should be decreased, but it must be regarded that past a certain diameter the wall effects become significant.

To eliminate these unwanted effects Calderon et al. [28], have chosen a Tammann resistance chamber which is based on a capillary method with a stationary diffusion source. During the experiment a gaseous intermediate layer serves as a supply between the investigated species and the solvent. The key benefit of this method is that the initial and boundary conditions of the diffusion equation can be met more accurately. Furthermore, the melt is not disturbed by convection caused by the difference in densities or phase transition of the sample.

Electrochemical methods eliminate the majority of shortcomings capillary methods pose, such as uncontrolled convection, wall effects and long experimental time. However, they can only be used if the rate limiting factor is the diffusion of oxygen in the melt. Even though the oxygen dissolved in the hot metal bath does influence the refining reactions, it is not pinpointed to be the rate limiting step. Thus, making this method not suitable for the examination of the diffusion coefficients.

Species	Method	Investigator
Carbon		
$D_C = 1.1 \times \left\{1 + \frac{wt\%\ C}{5.3}\right\} \times 10^{-8}$	capillary-reservoir technique	Goldberg and Belton [25]
$D_C = 2.0 \times 10^{-9}$		Rout et al. [20]
$D_C = 1.0e^{-4} \times exp\left\{-\left(\frac{12100}{T_m+273.15} + 2.568\right) + \left(\frac{1320}{T_m+273.15} - 0.554\right)(\%C)\right\}$ With $T_m = 1563 - 93(\%C)$ for $0.18 < \%C \leq 4.5$ $T_m = 1535 - 84(\%C)$ for $\%C \leq 4.5$		Shukla et al. [29]
Manganese		
$D_{Mn} = 1.8 \times 10^{-7} \times exp\left(-\frac{13000}{RT}\right)$	Tammann resistance furnace	Calderon et al. [28]
$D_{Mn} = 7 \times 10^{-9}$		
From D_{Mn}(1550°C): 1.77x10^{-9} To D_{Mn}(1700°C): 2.5x10^{-9}	capillary-reservoir technique	Kawai et al. [26]
8.8x10^{-9} to 1.05x10^{-8}	capillary-reservoir technique	Grace [27]
Silicon		
$D_{Si} = 5.1 \times 10^{-7} \times exp\left(-\frac{9150}{RT}\right)$	Tammann resistance furnace	Calderon et al. [28]
$D_{Si} = 3.8 \times 10^{-9}$		Rout et al. [20]
From D_{si}(1550°C): 4x10^{-9} To D_{si}(1725°C): 5x10^{-9}	capillary-reservoir technique	Kawai et al. [26]
1.78x10^{-8} to 2.11x10^{-8}	capillary-reservoir technique	Grace [27]
Phosphorus		
$D_P = 6 \times 10^{-9}$		Rout et al. [20]
$D_P = 4.7 \times 10^{-9}$		

Table 1 Overview of different diffusion coefficients

5.1.4 Rate Theory

To accurately describe interfacial reactions in mathematical terms, it is crucial to formulate diffusion coefficients and reaction rates that drive the chemical reactions. In theory mutual diffusion coefficients in dilute liquid metal have been correlated by methods based on absolute rate theory and the theory of corresponding states [30]. The mutual diffusion coefficient quantifies the rate at which the components of a mixture diffuse into each other. It is a measure of how quickly the different species within the mixture mix. Both approaches reproduce experimental data with similar precision.

The absolute rate theory focuses on the relationship between self-diffusion rates in a liquid and the lattice structure of the liquid state. Whereas, the theory of corresponding states suggests that the reduced viscosity or diffusivity of similar substances should exhibit universal behavior as functions of reduced temperature and pressure, particularly for simple molecules (monoatomic or spherical). In practical terms, the absolute rate theory requires less data and can be applied to a wider range of systems. Consequently, the theory of absolute reaction rates is employed to describe heterogeneous reactions occurring at interfaces, such as the slag-metal interface, liquid-gas interface (impact zone, emulsion zone), and solid-liquid interface (submodels: scrap melting, flux dissolution).

The theory is rooted in the concept that the reactants form, for an infinitesimally short time span, an intermediate activated complex. This activated complex exists in equilibrium with the reactants, and its state is described by its thermodynamic activities. The activated complex subsequently decomposes and forms the products. Considering the formation and decomposition of the intermediate state, rate constants for both forward and reverse reactions can be constituted.

It is known that the rate of a reaction is directly proportional to the concentrations of the reactants raised to some power. This knowledge can be used to calculate the rate of a reaction by measuring the concentrations of the reactants and determining the rate constant, which is a constant for a given reaction at a specific temperature.

5.1.4.1 Summary

The refining reactions in this study are modelled based on the theory of first-order rate equation, with exception of the decarburization in the impact zone when the carbon content falls below the critical level. Below this critical carbon content, gaseous diffusion becomes the rate-limiting step in the hot metal bath, rendering the adaptation of the first-order rate equation unsuitable for this particular refining reaction.

The diffusion process is characterized by using Fick's law and experimental data. From a wide array of measured diffusion coefficients, the most prevalent ones were chosen for integration into the model. Notably, the diffusion coefficients differ depending on the reaction zone. Thus, different coefficients were chosen to describe the mechanisms in different zones.

For the estimation of the refining rates, it is assumed that instantaneous equilibrium between reactants and products takes place. The estimation of refining rates and their respective rate-limiting steps varies among different constituents and is also dependent on the specific reaction zone. In the cases of Si, Mn, and P, the estimation of interfacial concentration utilizes the equilibrium distribution ratio, which is dependent on the slag composition and slag temperature. The equilibrium concentrations on the surface of a droplet in the emulsion zone are approached in the same manner as the equilibrium concentration for the slag metal zone.

5.2 Reaction Interfaces

The three main reaction interfaces considered in this thesis, as shown in Figure 4-4 (page 19), will be discussed in detail in this chapter. Generally, every reaction interface follows the same calculation steps. Firstly, the size of the reaction interface must be computed, followed by the mass transfer coefficients and lasty the refining rates.

5.2.1 Impact Zone

The impact zone is created by the gas jets exiting the nozzles located in the lance tip and impinging on the hot metal bath. The force of the jet or jets, depending on the number of nozzles, cause deformations on the liquid surface, resulting in paraboloid-shaped indentations. The impact zone area created equals the sum of all paraboloid indentations as shown in Figure 5-1.

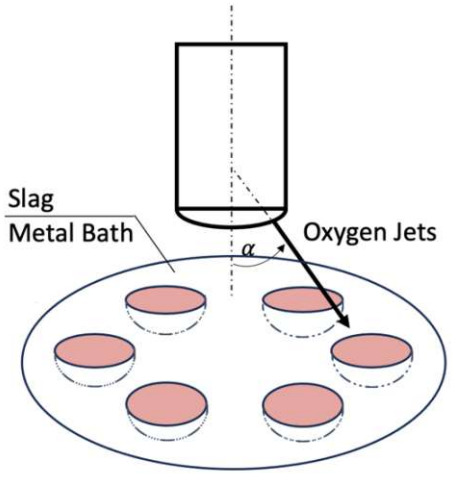

Figure 5-1 Depiction of impact interface created by a 6-nozzle lance

Understanding the depth, diameter and penetration caused by the jet is vital since these dynamic parameters dictate the sizes of the reaction zone, influencing the bath mixing and refining rates. To calculate these parameters the correlations proposed by Koria and Lange [31] are applied. These correlations were experimentally determined and are valid for carbon contents between 1 to 4% and the jets of the multi-nozzle lance do not coalesce on impinging. For precise calculations, refer to the Appendix 12.2, conducted using Mathcad Prime, which serves as a validation tool for simulated results.

The mass transfer coefficients depend on temperature, metal bath stirring intensity and the dimension of the furnace. The calculation of the bath stirring intensity is elaborated in the Appendix 12.3 Bath Stirring Energy. Furthermore, the listed dependencies have been discussed in a study conducted by Sawada et. al [32]. The work has later been extended by the work Kitamura et. al [33] showing that the there is a good correspondence between the change of the mass transfer coefficients and the furnace scale.

According to these findings, the mass transfer coefficient in the metal phase for silicon, manganese, phosphorus, and carbon is mathematically expressed as Eq. 4.

$$log\left(k_m^{gm}\right) = 1.98 + 0.5\, log\left(\frac{\varepsilon H_B^2}{100 H_L}\right) - \frac{125000}{2.3RT} \qquad \text{Eq. 4}$$

Hereby it is assumed that the fluid flow is steady, there is no compressibility effect, the impact of the slag phase is not considered, the system is considered isothermal, and there is no change of internal energy of the system due to chemical reactions. The modelling is based on a mixed control kinetics including gas phase mass transfer and chemical kinetics as well as the retarding effect of sulphur on the decarburization rate proposed by Dogan [19]. Furthermore, it is assumed that the equilibrium concentrations are approximately 0 at the impact zone reaction interface area.

An overview of reactions that are considered to take place in the jet impact zone is presented in Figure 5-2.

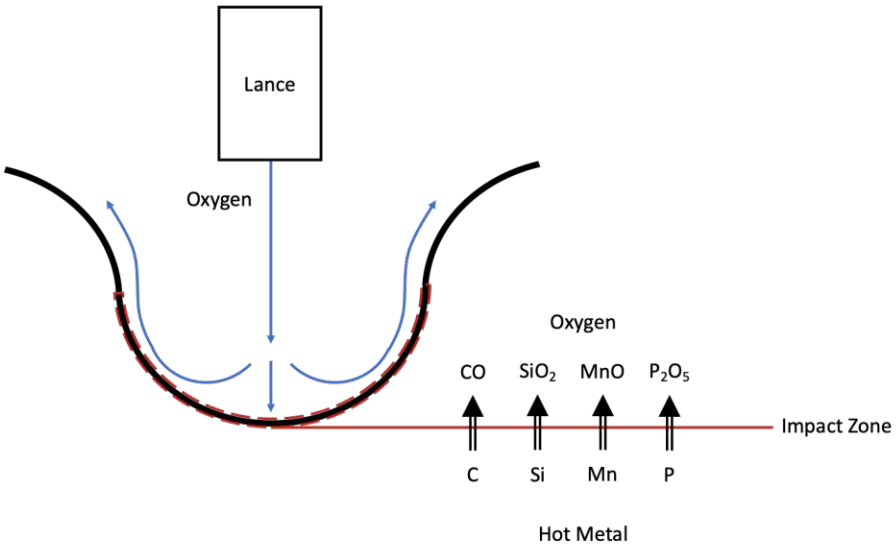

Figure 5-2 Impact zone refining reactions

The kinetics of silicon, manganese and phosphorus refining are assumed to be controlled by mass transport in liquid phase, as suggested in [20], and are described by Eq. 5. Notably the kinetics of carbon refining depend on the critical content of carbon in the metal bath, which is assumed to be 0.3 wt%. Below the critical carbon content, the carbon diffusion in liquid metal is the rate limiting step and the decarburization rate can be expressed using Eq. 5.

$$\left.\frac{d(W_m C_{jm})}{dt}\right|_{iz} = -A_{iz} k_m^{gm} \rho_m \left(C_{jm} - C_{jm}^{gm}\right) \qquad \text{Eq. 5}$$

$$j = Si, Mn, P \; and \; C_{crit} \leq 0.3 \; wt \; pct$$

Down to the critical carbon content, however, the gaseous diffusion controls the carbon refining rate which is expressed using Eq.6-8.

$$C_{crit} > 0.3 \; wt \; pct$$

$$\left.\frac{d(W_C)}{dt}\right|_{iz} = \left(\frac{dW_C}{dt}\right)_{iz}^{CO_2} + \left(\frac{dW_C}{dt}\right)_{iz}^{O_2} \qquad \text{Eq. 6}$$

$$\left(\frac{dW_C}{dt}\right)_{iz}^{CO_2} = -100 \times M_C A_{iz} k_{ap} P_{CO_2} \qquad \text{Eq. 7}$$

$$\left(\frac{dW_C}{dt}\right)_{iz}^{O_2} = -200 \times M_C A_{iz} k_g \left(1 + P_{O_2}\right) \qquad \text{Eq. 8}$$

5.2.2 Slag Metal Zone

Due to the high impact force generated by the top blow jet, it is assumed that the slag phase is pushed to the side, resulting in the formation of a reaction zone of permanent contact between the slag and hot metal bath, the “slag metal zone” reaction interface. The estimation of the slag metal zone reaction interface is based on the momentum balance for the impact zone calculation and is implemented by using Eq.9 [20].

$$A_{sm} = \pi \left(\frac{d_B^2}{4} - n_{nozzle} \times r_{cav}^2\right) \qquad \text{Eq. 9}$$

To quantify the mass transfer in the slag phase, the mathematical model employs the mass transfer coefficient proposed by the authors [33], [34], as given by Eq. 10. It was observed that the dependence of the mass transfer coefficient in metal and in slag on temperature and stirring energy is almost the same.

$$k_s = a \cdot exp(-\frac{37000}{RT}) \cdot \varepsilon$$ Eq. 10

The kinetics of reactions at this reaction interface were estimated using the concept of mixed controlled mass transfer, as proposed by Rout et al. [20]. Mixed controlled mass transfer refers to a scenario where mass transfer is influenced by multiple factors and mechanisms simultaneously. The assumptions made to model this zone include that the effect of surface oscillation is considered between slag and bulk metal and that instantaneous equilibrium between the reactants and products occurs at each computational time step. The refining reactions of manganese, silicon, phosphorus, and carbon are calculated using Eq. 11.

$$\left.\frac{d(W_m C_{jm})}{dt}\right|_{sm} = -A_{sm} k_m^{sm} \rho_m \left(C_{jm} - C_{jm}^{sm}\right)$$ Eq. 11

In contrast to the impact zone interface, where the equilibrium concentrations of the impurities are assumed to be zero, the interfacial equilibrium concentrations at the slag metal interface are implemented as proposed by [20] using distributions ratios as described by Eq.12-15. The exact calculation of the distribution ratios is explained in [20].

$$C_{sm,C,eq} = \frac{P_{CO} a_{Fe}}{f_C a_{FeO} K_C}$$ Eq. 12

$$C_{sm,Si,eq} = L_{Si} C_{Si}$$ Eq. 13

$$C_{sm,Mn,eq} = \frac{C_{Mn}}{L_{Mn}}$$ Eq. 14

$$C_{sm,P,eq} = \frac{C_P}{L_P}$$ Eq. 15

5.2.3 Emulsion Zone

The top gas jet impinges the metal bath, the force of which causes the formation of cavities. Due to the high tangential velocity of the gas jet on the side wall of the cavity a large number of metal droplets are ejected, schematically represented by Figure 5-3. Depending on the lance height over time the number of ejected droplets varies and thus the size of the dynamically generated emulsion zone. The summation of ejected droplet surfaces equals the reaction interface. The reaction interface is dynamically generated over time and its size influences the hot metal refining greatly. Thus, calculating the size of this reaction interface is vital for the accuracy of the process depiction.

There are various theoretical and experimental approaches investigating the calculation of the emulsion zone size. Van der Knoop et. al [35] for example estimated the size of the emulsion zone of a 300-ton converter. The study concluded that over a blowing time of 16 minutes the bath would be refreshed every 1.4 minutes causing a conversion of 27.1 ton/minute. This would further mean that 4.4 m^2/second "new" emulsion area are created, which is available for refining reactions over the time of the droplet residence in the emulsion.

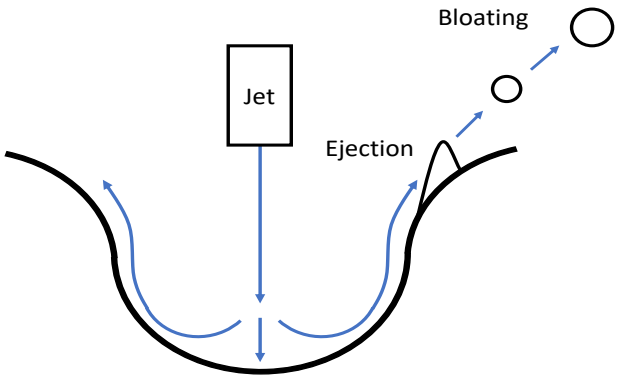

Figure 5-3 Mechanism of droplet ejection and bloating

The approach used for the model presented in this work is based on a dynamic droplet generation rate as proposed by [36]. Its implementation is described in the following paragraphs.

Firstly, it is assumed that the density of the blown gas changes when it is blown onto the hot metal. Thus, a temperature correction of the gas jet must be conducted, Eq. 16.

$$F_{g,T} = \frac{P_{g,0}}{P_{g,iz}} \frac{T_{g,iz}}{T_{g,0}} F_g \qquad \text{Eq. 16}$$

Secondly, the blowing number is calculated, Eq. 17. The blowing number is highly dependent on the calculation approach chosen for the tangential velocity. These different approaches and their impact on the overall simulation will be discussed in a separate chapter.

$$N_T = \frac{\eta^2 \rho_{g,iz} u_x^2}{2\sqrt{\rho_m \sigma_m g}} \qquad \text{Eq. 17}$$

Thirdly, using the calculated blowing number the droplet generation rate is estimated Eq. 18, which predicts the mass of generated droplets per second. With the knowledge of the droplet density the emulsion zone area can be calculated.

$$R_T = \frac{(N_T)^{3.2}}{[2.6\times10^6 + 2.0\times10^{-4}(N_T)^{12}]^{0.2}} F_{g,T} \qquad \text{Eq. 18}$$

After determining the surface, the rate of mass transfer between metal drops and slag can be specified for a single droplet Eq. 19 and lastly the rate of refining of bulk metal by the emulsion zone can be expressed by Eq. 20.

$$\left.\frac{d(W_d C_{d,j})}{dt}\right|_{em} = -A_d k_d^{em} \rho_m \left(C_{d,j} - C_{m,j}^{em}\right) \quad \text{Eq. 19}$$

$$\left.\frac{d(W_m C_{m,j})}{dt}\right|_{em} = -\frac{W_{m,j}^{eject,t} - W_{m,j}^{return,t}}{\Delta t} \quad \text{Eq. 20}$$

The determination of the equilibrium concentration of carbon is strongly influenced by the temperature and the metal bath composition, therefore a polynomial equation is used, [37].

For the impurities P, Mn, and Si, the equilibrium distribution ratio is expressed as a function of the metal bath composition and the temperature.

$$C_{m,j} = \frac{C_{m,j}}{L_j} \quad \text{Eq. 21}$$

It is crucial to factor in the change in droplet temperature to be able to depict the environment where the refining reactions take place more realistically. The droplet temperature is assumed to be the same as the impact zone temperature at the time of ejection. However, according to the findings of Rout et al. [38], it is observed that the droplet temperature decreases as it spends more time in the emulsion zone. To capture this behaviour, a correlation based on the droplet's conductivity and heat capacity is implemented. This correlation allows for the estimation of the droplet temperature as it progresses through the emulsion zone, considering the thermal characteristics of the droplet.

$$T_d = T_{iz} + \frac{T_{iz} - T_s}{1+\beta} \quad \text{Eq. 22}$$

$$\beta = \left(\frac{\lambda_m C_{p,m} \rho_m}{\lambda_s C_{p,s} \rho_s}\right)^{0.5} \quad \text{Eq. 23}$$

Furthermore, the surface tension of a droplet plays a crucial role in influencing the rate of carbon monoxide (CO) nucleation, as highlighted in reference [39]. Surface-active elements such as sulphur and oxygen negatively affect the surface tension, whilst carbon has a positive effect on it. Based on this knowledge an equation was implemented to account for this effect.

5.2.3.1 *Droplet classification*

The droplets ejected into the emulsion zone can be categorized into three main classes. First, there are droplets that undergo decarburization, resulting in bloating up to 10 times their original size and remaining in the emulsion zone for several minutes [40]. Second, there are droplets that do not undergo decarburization and return to the metal bath within less than a second, referred to as dense droplets. Finally, some droplets are small enough to get blown out through the mouth of the converter, cooling down and solidifying resulting as dust in the off-gas stream.

The mechanism accountable for the long residence time of the first droplet class is based on the bloating due to internal decarburization, when ejected into the oxidizing atmosphere. Due to the expansion and rapid decarburization, Eq. 25, the droplet density decreases, Eq. 24. Therefore, the residence time in oxidizing atmosphere is prolonged affecting the refining reaction taking place on the surface of the droplet. This phenomenon is known as the "bloated droplet theory". Once the droplets are ejected from the metal bath, the refining process begins. The changes in area, described by Eq. 26 and Eq. 27, and volume, represented by Eq. 28, of the metal droplets due to the bloating phenomena are estimated using an empirical correlation that accounts for the variation in density as a function of the decarburization rate.

$$\rho_d = \begin{cases} \rho_{d_0} \frac{rate_c^*}{rate_c}, & rate_c < rate_c^* \\ \rho_{d_0}, & rate_c \leq rate_c^* \end{cases} \quad \text{Eq. 24}$$

$$rate_c^* = \begin{cases} 2.86 \times 10^{-4} \times 20 & , C_{s,FeO} > 20, \\ 2.86 \times 10^{-4} \times C_{s,FeO}, & C_{s,FeO} \leq 20 \end{cases} \quad \text{Eq. 25}$$

$$d_d(t) = \left(\frac{6}{\pi} \times \frac{W_d}{\rho_d(t)}\right)^{1/3} \quad \text{Eq. 26}$$

$$A_d(t) = \pi \times d_d(t)^2 \quad \text{Eq. 27}$$

$$V_d = \frac{1}{6}\pi d_d^3 \quad \text{Eq. 28}$$

In order to estimate the residence time of the ejected droplets in the emulsion zone the bloated droplet theory is coupled with the ballistic motion principle as proposed by Brooks et. al [41]. This approach assumes that the phase through which the droplets travel is quiescent, allowing for the establishment of a force balance that includes buoyancy, gravity, drag, and "added mass" effects. By considering these forces, the trajectory and motion of the droplets can be determined, Figure 5-4. For the calculation, a simple explicit forward differencing numerical method is employed. However, in the event of an instability or error while running this submodel, a simplified estimation for the residence time of a spherical droplet in motion in the emulsion zone is implemented as a fallback. This simplified estimation is based on the ratio of the droplet's diameter to its velocity. While it is a less precise approach, it serves as a safeguard to ensure the continuity of the simulation and prevent potential failures.

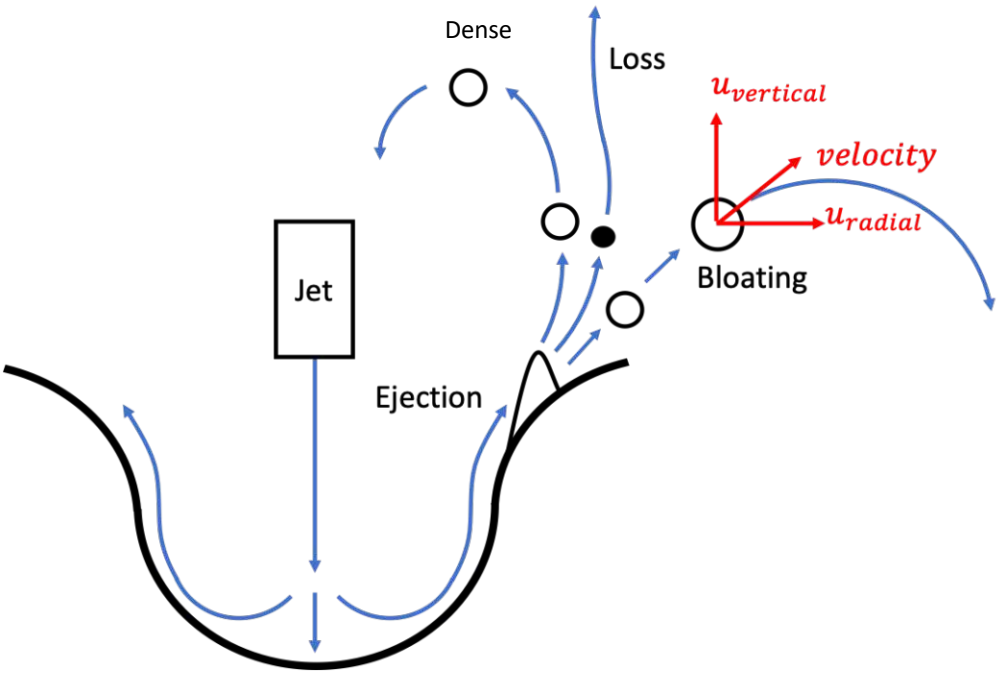

Figure 5-4 Droplet velocity calculation

The second class of droplets comprises the dense droplets, which are ejected into the emulsion zone at ejection angles ranging from less than 10° to more than 80°. Due to these steep ejection angles, the residence time of dense droplets within the emulsion zone is assumed to be less than 1 second, rendering them incapable of significantly influencing the refining rates.

Lastly, despite conducting an extensive literature review, no research group has yet attempted the modelling of the produced dust. Therefore, in the presented mathematical model, an extension has been made to account for the differentiation between the three droplet classes. After consulting with experts, it was assumed that approximately 3% of the metal bath ends up as dust in the off-gas stream during one blow. This estimate has been incorporated into the calculation algorithm.

The number of droplets ejected into the emulsion zone and consequently the distribution among the different droplet classes heavily relies on the calculation of the jet velocity. Determining the velocity of the oxygen jet in a jet impact cavity can be accomplished using various correlations. For an overview of the available methods, refer to Table 2.

All of these methods have been implemented in the model, but the best fitting method is hardcoded and cannot be switched using the user interface. While the model calculation remains stable regardless of the chosen velocity calculation method, the results are significantly affected. Advanced users who wish to study the behaviour of different jet axial velocity correlations can switch between the methods using the gPROMS Modelbuilder language interface.

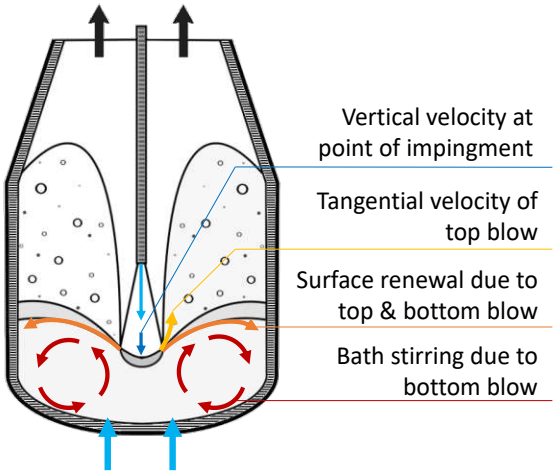

Figure 5-5 Different velocities within the furnace

The impact of the different calculation methods can be clearly observed in Figure 5-7 and Figure 5-8. Depending on the chosen method, the jet velocity in the impact zone varies between 30 m/s and 450 m/s. A CFD study indicates that the jet velocity at impact is generally high, leading to the calculation method proposed by Deo and Boom [15] was chosen for the mathematical model.

Investigator	Jet axial velocity	
Standish et al. [42]	$u_x = u_o \frac{0.97}{\frac{2ah}{d_e}+0.29}$ $a = 0.07$ for cold model	Eq. 29
Deo and Boom [43]	$u_x = \sqrt{\frac{2P_{g,iz}}{\rho_{g,iz}}}, \frac{P_{g,iz}}{P_o} = 230\left(\frac{h}{d_t}\right)^{-2.4}, \rho_{g,iz} = \frac{P_a M_{O_2}}{RT_{g,iz}}$	Eq. 30
Subagyo et al. [44]	$u_x = u_o \frac{0.97}{\frac{2ah}{d_e}+0.29}$ $a = 0.0382$ hot metal data with no reaction $a = 0.0393$ for plant data	Eq. 31
Sumi et al. [45]	$u_x = u_o(1 - e^{-0.5\varepsilon_u})$, $\varepsilon_u = \alpha\sqrt{\frac{\rho_{g,iz}}{\rho_e}}\frac{H_L}{d_e} - \beta,$ $\alpha = 0.0841, \beta = 0.6035$	Eq. 32

Table 2 Jet axial velocity calculation

The different approaches for simulating the jet axial velocity are summarized in Table 2.

5.2.3.2 *Discussion*

The operation conditions during the blow are chosen to be the same as presented in [46] and are depicted in Figure 5-6. Literature suggests that the most influential factors with regard to the droplet generation simulation are the lance height and the volume flow rate. This context can be observed clearly when comparing Figure 5-6 and Figure 5-7.

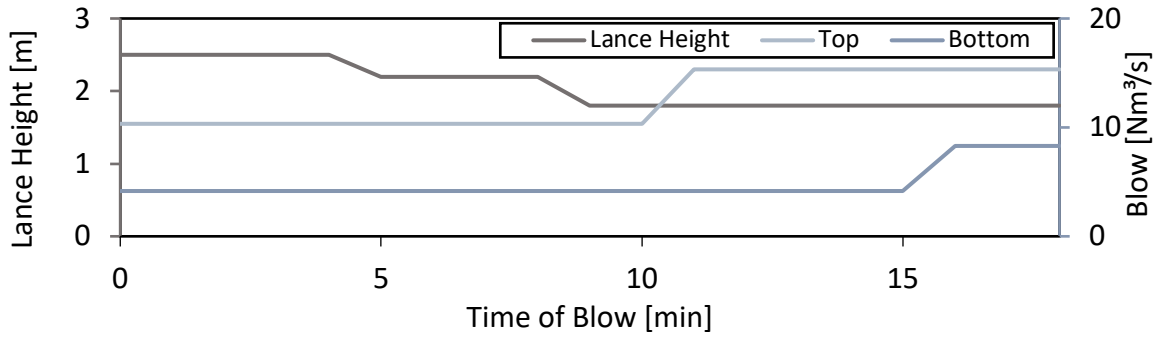

Figure 5-6 Blowing conditions for droplet generation examination

Figure 5-7 presents a graphical summary of the jet velocity simulation results obtained using various calculation methods. It is evident from the simulation results that the outcomes diverge significantly depending on the approach employed. The influence of these calculation methods on the droplet generation rate is illustrated in Figure 5-8.

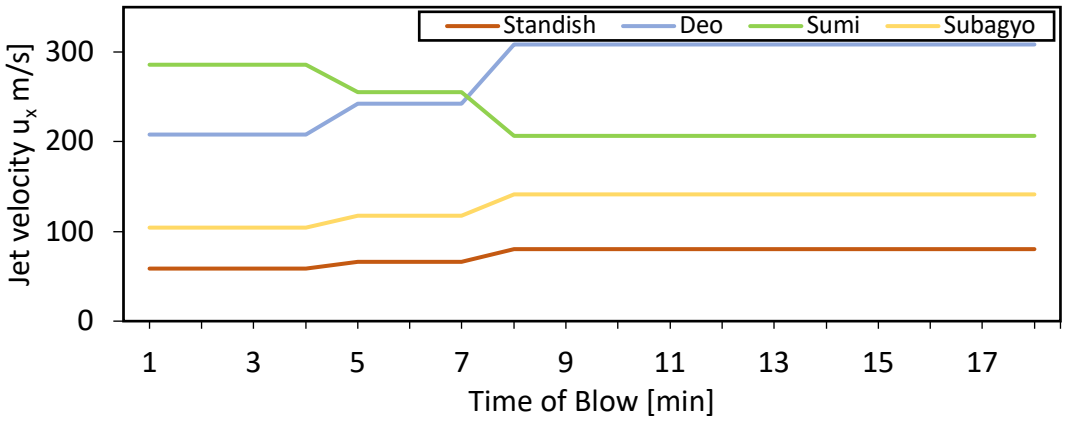

Figure 5-7 Summary of jet velocity calculation methods

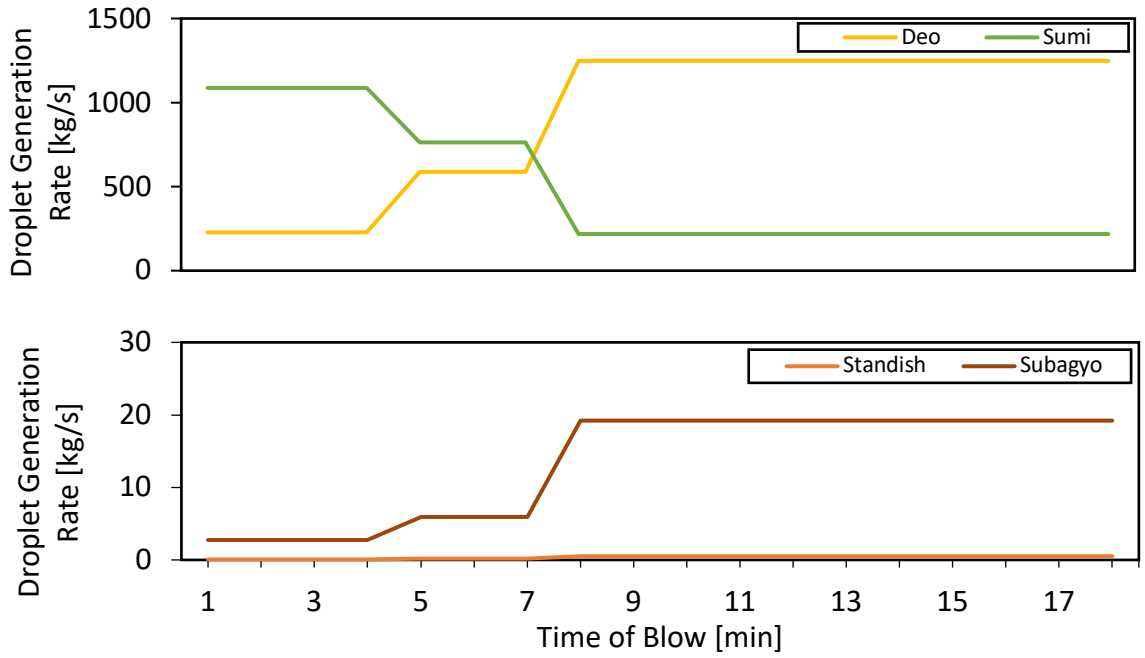

Figure 5-8 Simulated droplet generation rates using different calculation methods

It is noteworthy that applying the predictions for the correlations provided by Sumi et al. [47] show a decrease in droplet generation with decreasing lance height. However, research and cold model studies conducted by various research groups suggest that the droplet generation rates increase with decrease in lance height until reaching a critical lance position. The critical lance position is characterized by the jet not impinging but penetrating the hot metal bath, which in turn reduces the number of droplets ejected from the hot metal bath [31].

Based on the examination of the simulated droplet generation rates it is reasonable to conclude that the correlation provided in [47] does not produce satisfactory results and thus will not be used in the final model. Furthermore, correlations provided by [42] and [44] seem to underpredict the droplet generation rate gravely and will also be excluded. Thus, the method presented by [43] is chosen for the final model.

Figure 5-9 and Figure 5-10 present the behaviour of the generated reaction interface per droplet class and the corresponding carbon content reduction within each class with respect to time and the blowing parameters. Each class corresponds to a specific droplet size, starting at class 1 with a diameter of 0.23 mm with an increment in diameter of 0.35 mm per class. The generation of the reaction interface is already discussed in relation to its dependence on the jet velocity calculation, lance geometry, and its proximity to the hot metal bath. The simulations were conducted using the dataset for the converter provided by [46].

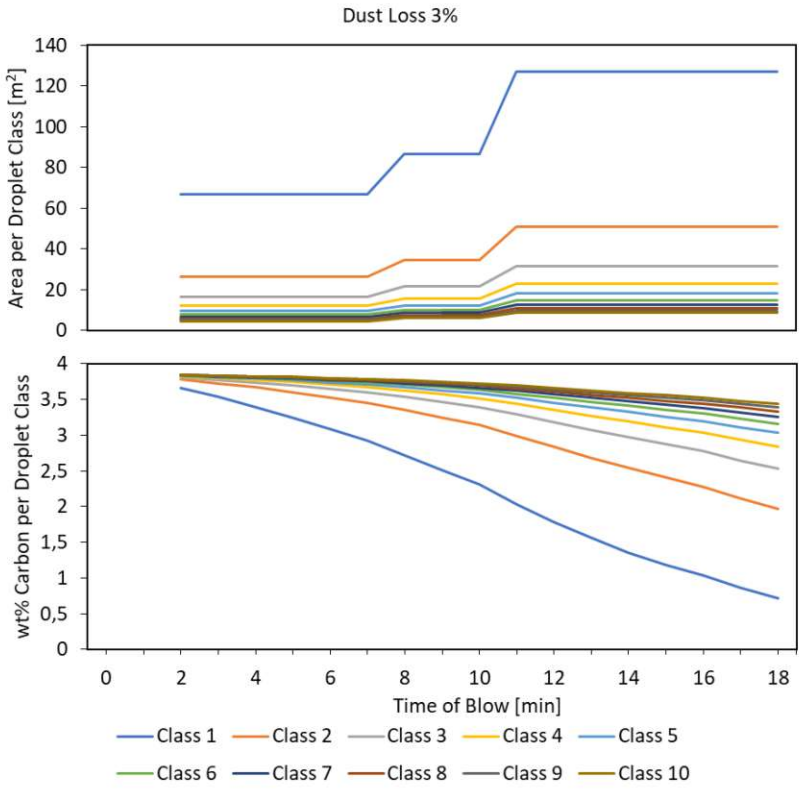

Figure 5-9 Droplet area and carbon content per droplet class with consideration of 3% dust loss

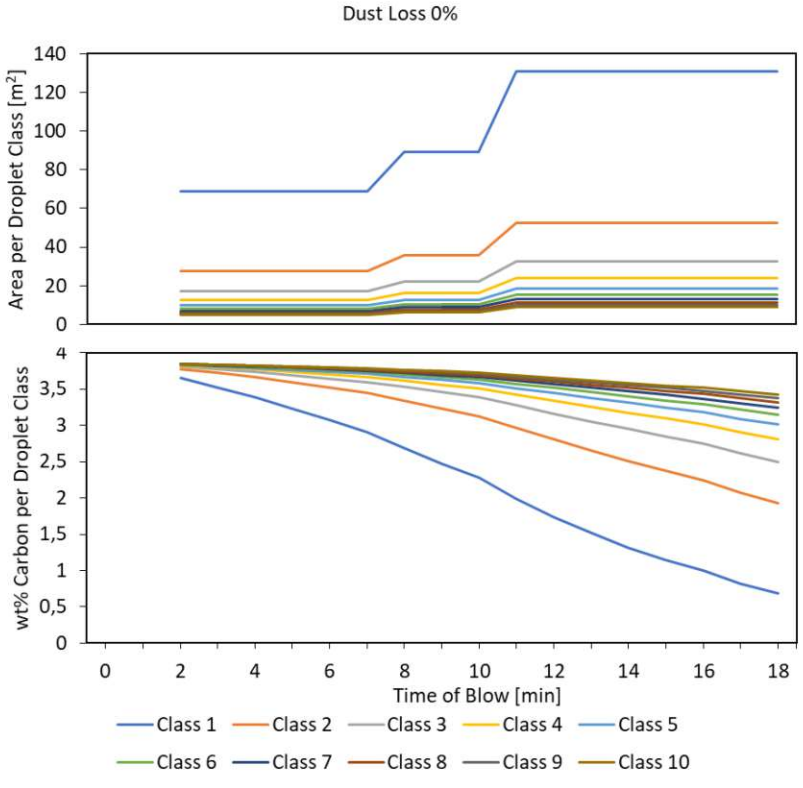

Figure 5-10 Droplet area and carbon content per droplet class without considering dust loss

The simulations reveal that the implemented droplet classification does not exert a grave impact on the refining reactions. This observation is particularly evident in Figure 5-11, where a comparison of decarburization for the first droplet class with and without dust loss is depicted.

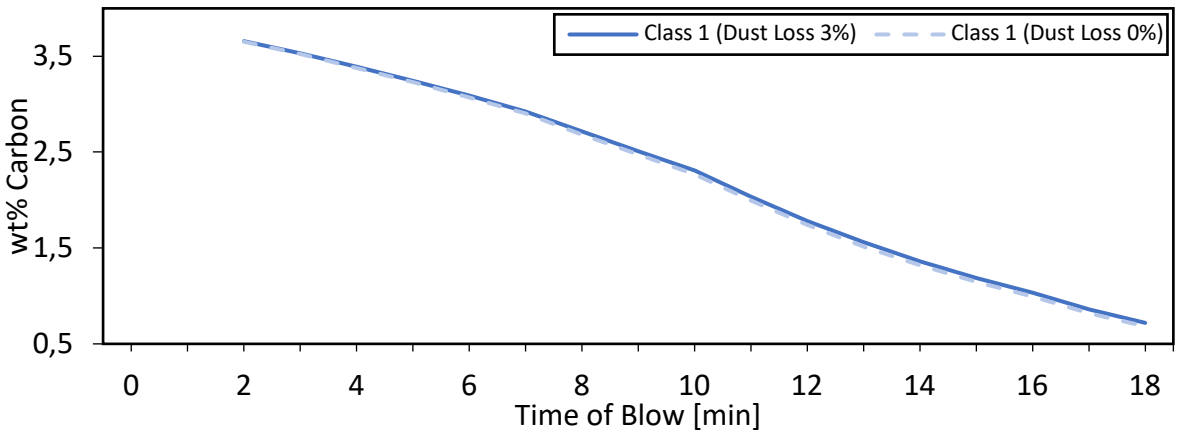

Figure 5-11 Evolution of carbon content for droplet class 1 with respect to dust loss

However, the results of the simulation suggest that introducing a correlation that characterizes the operational parameters leading to the ejection of smaller droplets may exert a more pronounced influence on the refining rates. Especially since Figure 5-9 and Figure 5-10 show that the droplet class 1 which contains the droplets with the smallest diameter generates the largest reaction interface and thus the most refining is taking place there.

To establish such a correlation, a comprehensive computational fluid dynamics (CFD) study would be of great use, focusing on investigating how different blowing parameters affect droplet size production.

Furthermore, determine the most appropriate correlation, a study on how the different approaches impact the refining rates was conducted, as shown in Figure 5-12. Upon reviewing the deviations from the measured data points, the correlations provided by Deo and Boom were found to the most suitable for implementation.

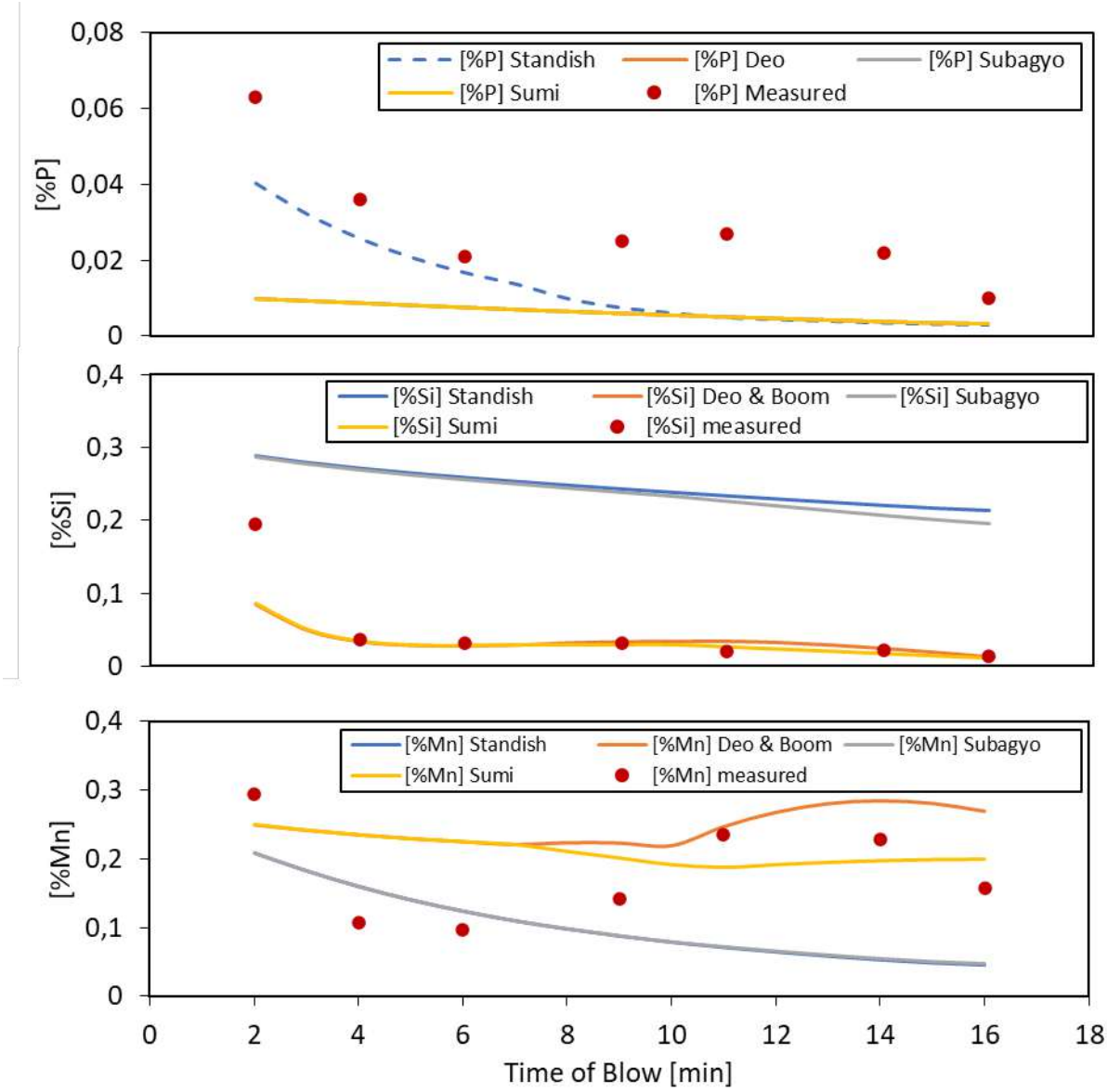

Figure 5-12 Refining rates depending on different jet velocity calculations.

5.2.3.3 Mass transfer droplet interface

Several research groups apply Higbie's penetration theory to model the mass transfer coefficient of a droplet in the emulsion zone. This theory posits that the interaction between the moving hot metal droplet and slag emulsion occurs through turbulent eddies, resulting in unsteady-state diffusion or penetration of the transferred species during their contact time. In order to calculate the mass transfer, it is necessary to determine the appropriate coefficients that depend on the characteristics of the reaction interface.

The mass transfer coefficient in metal phase can be described as follows:

$$k_{jm}^{d} = 2 \times \sqrt{\frac{D_j}{\pi t_{res}}} = 2 \times \sqrt{\frac{D_j u}{\pi d_p}} \qquad \textit{Eq. 33}$$

For the mass transfer in slag phase, it is assumed that the droplet is surrounded by a constant stream of slag. Due to the high Schmidt number the boundary layer is assumed to be laminar thus the effects of turbulence on the mass transfer can be neglected. Which results in an overall mass transfer of:

$$\frac{1}{k_d^{em}} = \frac{1}{k_{jm}^{d}} + \frac{\rho_m}{k_s^{d} \rho_s L_j} \qquad \textit{Eq. 34}$$

The diffusion of different constituents at the emulsion zone area undergoes two phases. During the first phase manganese, phosphorus, and silicon reach equilibrium. During the second phase active oxides block reaction spots on the surface area, slowing down the refining reactions. Figure 5-13 and Figure 5-14 schematically depict the mechanism of both phases.

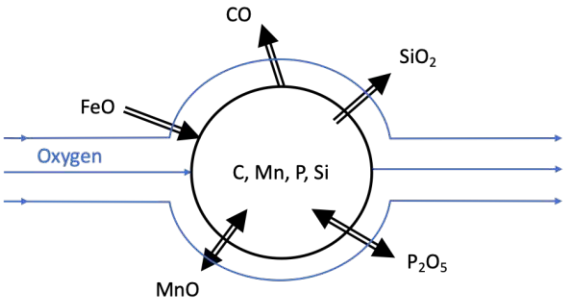

Figure 5-13 Firstly Mn, P, Si reach equilibrium

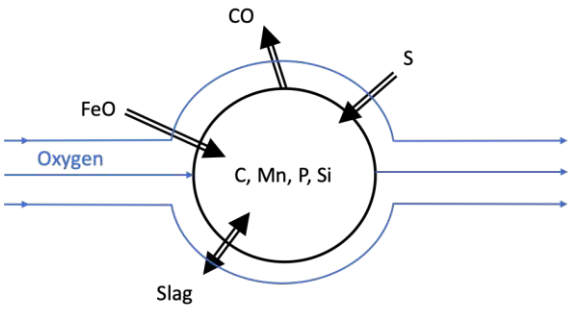

Figure 5-14 Secondly C refining is limited by surface active oxides and S

5.2.3.4 Discussion

It is crucial for the understanding and modelling of the refining kinetics of the reactions, to parameterize the number of droplets ejected into the emulsion zone due to the impinging gas jet on the surface of the hot metal bath. Thus, it is important to discuss how different investigators have approached the calculation of the axial jet velocity which is the key factor in estimating the droplet amount.

Several studies have been performed to develop functional correlations to predict the drop generation due to the impinging gas jet on the liquid surface. Standish et al. developed a

functional relationship between Weber number and droplet generation rate on basis of their cold model experiments. Deo and Boom applied this relationship to a real BOF process and derived a correlation between amounts of metal ejected per unit volume blown gas as a function of the Weber number. Furthermore, a modified blowing number has been proposed to correct the temperature effect on droplet generation rate and has been found to be suitable for the prediction of droplet generation rate. The total number of ejected droplets into the emulsion zone, results in a cumulative weight of up to a maximum of 21 percent of the total hot metal.

It is found that not only oxygen jet velocity, impact zone temperature, bottom stirring and pressure within the vessel influence the droplet generation but it is also suggested that the wear of the lance might influence the flow leaving the nozzle gravely. For future extension of the model it might be of interest to factor in the wear of the lance.

Furthermore, previous work conducted by different research groups does not consider the generation of dust, as well as the reduced residence time of droplets that are ejected onto the refractory lining, or droplets that do not bloat upon ejection into the furnace atmosphere.

5.3 IMPURITIES

5.3.1 Carbon

The carbon removal process in the Basic Oxygen Furnace (BOF) can be divided into three distinct phases: the initial phase, the second phase, and the third phase.

In the initial phase, a significant portion of oxygen is consumed for the oxidation of minor elements such as silicon (Si), manganese (Mn), phosphorus (P), titanium (Ti), and vanadium (V). This phase plays a critical role in achieving a low carbon content and typically accounts for about 60-70% of the total carbon removal. The decarburization rate during this phase is primarily controlled by the oxygen supply.

The second phase occurs when the carbon content reaches a critical level, and the mass transfer of dissolved carbon becomes a rate-limiting step. As a result, the decarburization rate starts to decrease linearly as a function of carbon content. This phase is characterized by the partial reduction of oxidized phosphorus (P) and manganese (Mn) in the metal bath due to the reduction potential of carbon, which is highest at the critical carbon content.

In the third phase, the carbon content is no longer able to reduce all of the formed iron oxide (FeO), leading to a rapid increase in the FeO content in the slag. Subsequent oxidation becomes necessary during this phase to maintain the required temperature and chemical balance in the furnace.

To summarize, the three phases of carbon removal in the Basic Oxygen Process are distinct and critical for achieving the desired steel quality, as shown in Figure 5-15.

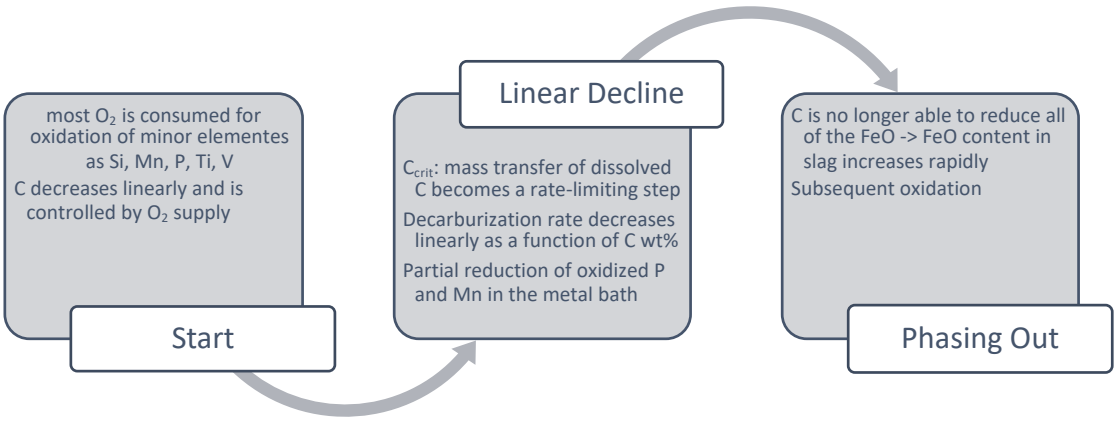

Figure 5-15 Three phases of decarburization

The decarburization does further differ strongly depending on the reaction interface. In the impact zone, decarburization occurs through the oxidation of carbon in the melt with gaseous oxygen and carbon dioxide at the gas-metal interface. The rate of decarburization caused by the reaction with oxygen is assumed to be controlled by mass transfer in the gas phase. On the other hand, decarburization by carbon dioxide is believed to be controlled by both mass transfer in the gas phase and chemical reaction at the interface. The retracing effect of sulphur is also included in the kinetic model.

In the emulsion zone, describing decarburization becomes more complex due to interactions between different constituents. The rate of carbon removal slows down in the presence of silicon and manganese in the droplet, while the internal nucleation of carbon monoxide gas increases the kinetics of phosphorus transfer. An increase in sulphur level in the droplet influences the CO formation rate. The quick formation of surface-active oxides like silicon dioxide SiO_2 and phosphorus pentoxide P_2O_5 slows down the kinetics of decarburization by blocking the reaction sites for carbon and iron oxide reaction.

[C]+(FeO)={CO}+[Fe] Eq. 35

$$C_{m,C,eq} = \frac{P_{CO}\alpha_{Fe}}{f_c\alpha_{FeO}K_c} \quad \text{Eq. 36}$$

$$log(K_c) = 5.096 - \frac{5730}{T_m} \quad \text{Eq. 37}$$

$$a_C = C_C f_C \quad \text{Eq. 38}$$

$$log(f_c) = 0.1666C_{m,C} - 0.01585C_{m,C}^2 + 9.9613 \times 10^{-7}C_{m,C}^3(T-273) + 3.0246 \times 10^{-5}C_{m,C}(T-273) \quad \text{Eq. 39}$$

5.3.1 Silicon

Capturing the evolution of silicon is of high importance when describing the BOF process because its oxidation reaction is a great heat source. Furthermore, the Si joins with the lime and dolomite added throughout the blow, which then influences the amount of slag generated. This interlinks the desiliconization and dephosphorization because the amount of slag generated is the main influencing factor for the efficiency of the P oxidation.

In general Si has a great affinity for oxygen which leads to most of it being refined within the first quarter of the blow. The evolution of the desiliconization process however differs between reaction zones. Within the impact zone oxygen predominates and thus becomes the driving factor for the Si present to get oxidized.

Impact Zone

$(O_2)_g = 2[O]$ Eq. 40

$$logK_o = \frac{6170}{T_{iz}} + 0.125$$ Eq. 41

$[Si]+2[O]=(SiO_2)$ Eq. 42

$$logK_{Si} = \frac{30110}{T_{iz}} - 11.40$$ Eq. 43

$$logK = logK_o + logK_{Si}$$ Eq. 44

At the slag metal interface however, there is much more FeO than oxygen which makes it the main cause for silicon oxidation. Lastly in the emulsion zone, the droplet surface is in contact with both iron oxide and oxygen, thus the refining is promoted by both constituents. It has been suggested that the presence of more than 0.05 wt% of Si hinders the nucleation of CO at slag-metal interface which leads to good slag-metal contact and an acceleration in the desiliconization, [48]. It is also important to note that the equilibrium partition ratio changes if the slag contains more than 40 wt% FeO. The reasoning behind that assumption is that experimental work has suggested that the desiliconization reaction is controlled only by the mass transport in metal phase.

Slag Metal interface

$[Si] + (Feo) = (SiO_2) + [Fe]$ Eq. 45

$$L_{Si} = \begin{cases} 1 - \frac{C_{s,Fe}}{40}, C_{s,FeO} \leq 40 \\ 0, C_{s,Feo} > 40 \end{cases}$$ Eq. 46

$$C_{sm,Si,eq} = L_{Si} \times C_{m,Si}$$ Eq. 47

5.3.2 Manganese

The key to understanding the behaviour of manganese during a blow, is the knowledge of the distribution ratio. Suito and Inoue [49] conducted a thorough investigation of the manganese distribution ratio between high MnO-containing slags and steel/hot metal, shedding light on manganese behaviour. Based on studies involving slags with small amounts of MnO (0.6-5 mass%, [30]) as well as high amounts of MnO (8-16 mass%) the activity coefficients, equilibrium quotients and manganous capacity were formulated as a function of slag composition and temperature. Notably, the study highlighted that the distribution ratio of manganese in hot metal is significantly influenced by the total iron content, rather than the MnO content. These findings have been successfully integrated into various models, yielding accurate predictions, and are therefore incorporated in the formulation of the present model.

In this study, the estimation of the manganese distribution ratio begins with the calculation of MnO's activity coefficients, employing a linear function based on slag composition (Eq. 48). Subsequently a linear function based on a multiple regression analysis is applied to calculate the equilibrium quotient (Eq. 49). The manganous capacity, which relates the mass% of MnO to the activity of manganese and oxygen, is then determined (Eq. 50). Based on these calculations the distribution ratio and the equilibrium concentration can be accurately estimated.

$$log\gamma_{MnO} = 0.0415\left[C_{s,CaO} + 0.45C_{s,SiO_2} + 0.60C_{s,MgO} + 0.66C_{s,Fe_tO} + 0.45C_{s,MnO} + 0.95C_{s,P_2O_5}\right] + \frac{803}{T} - 3.075 \quad \text{Eq. 48}$$

$$logk'_{Mn} = -0.0180\left[C_{s,CaO} + 0.23C_{s,MgO} + 0.28C_{s,Fe_tO} - 0.98C_{s,SiO_2} - 0.08C_{s,P_2O_5}\right] + \frac{7300}{T} - 2.697 \quad \text{Eq. 49}$$

$$logC_{Mn} = -0.0188\left[C_{s,CaO} - 0.21C_{s,SiO_2} + 0.12C_{s,MgO} + 0.31C_{s,Fe_tO} + 1.65C_{s,P_2O_5}\right] + \frac{14200}{T} - 3.685 \quad \text{Eq. 50}$$

$$L_{Mn} = \frac{C_{s,MnO}}{[\%Mn]_i} \quad \text{Eq. 51}$$

$$C_{Mn,eq} = \frac{C_{s,MnO}}{L_{Mn}} \quad \text{Eq. 52}$$

5.3.3 Phosphorus

Phosphorus removal by direct oxidation is limited because the low equilibrium partial pressure of the gaseous products renders them thermodynamically unstable. As a result, dephosphorization mainly occurs at the interface between the slag and metal, provided that the slag exhibits a sufficiently high oxidizing potential and possesses the capacity to absorb phosphorus ions. Basic components in the slag provide free oxygen, and iron oxide rich slags promote this oxidation reaction. Which makes the iron oxide concentration and evolution a key part in predicting the phosphorus content in the hot metal bath. Additionally, additives such as lime and dolomite strongly absorb phosphate ions. One of the critical mechanisms involved in dephosphorization is the transport of phosphorus from the hot metal to the slag-metal interface. The rate of this transport is dependent on several factors, including the temperature and composition of the metal and slag. The transfer of phosphorus predominantly occurs through diffusion, and the rate of diffusion is influenced by the concentration gradient, the temperature, and the diffusion coefficient.

The determination of equilibrium concentrations requires the calculation of species activity, which can be challenging due to the evolving ionic nature of the slag over time. Therefore, the hypothetical species ($PO_{2.5}$) containing one phosphorus atom proposed by Nagabayashi et. al [50] has been chosen to represent the dephosphorization reaction. They investigated the phosphorus distribution between slag and liquid iron for temperatures between 1573 and 1953 K and formulated an equilibrium relation.

Based on the equilibrium relation of the phosphorus reaction (Eq. 53) the distribution ratio of phosphorus between slag and hot metal can be defined as Eq. 54, which subsequently allows for the determination of the equilibrium concentration Eq. 55.

$$P + 2.5O = (PO_{2.5})_{(slag)} \quad \text{Eq. 53}$$

$$L_p = 15.324 + 0.021C_{s,CaO} - 0.036C_{s,MgO} - 0.043C_{s,SiO_2} + 0.004C_{s,FeO} + 0.027C_{s,MnO} - 0.029C_{s,Al_2O_3} - 0.057C_{s,TiO_2} - 0.029C_{s,V_2O_5} - 0.006T \quad \text{Eq. 54}$$

$$C_{P,eq} = \frac{C_{s,P}}{L_P} \quad \text{Eq. 55}$$

The distribution ratio of phosphorus is a well-researched topic and there are a variety of proposed empirical models. This one was chosen due to its prediction being the closest to measured data sets.

5.3.2 Discussion Impurity Removal

Figure 5-16, shows a summary of the simulation results using different diffusion coefficients. The results differ significantly for the prediction of concentration in metal bath of manganese and silicon, whereas for carbon and phosphorus there is no apparent distinction between the different trends.

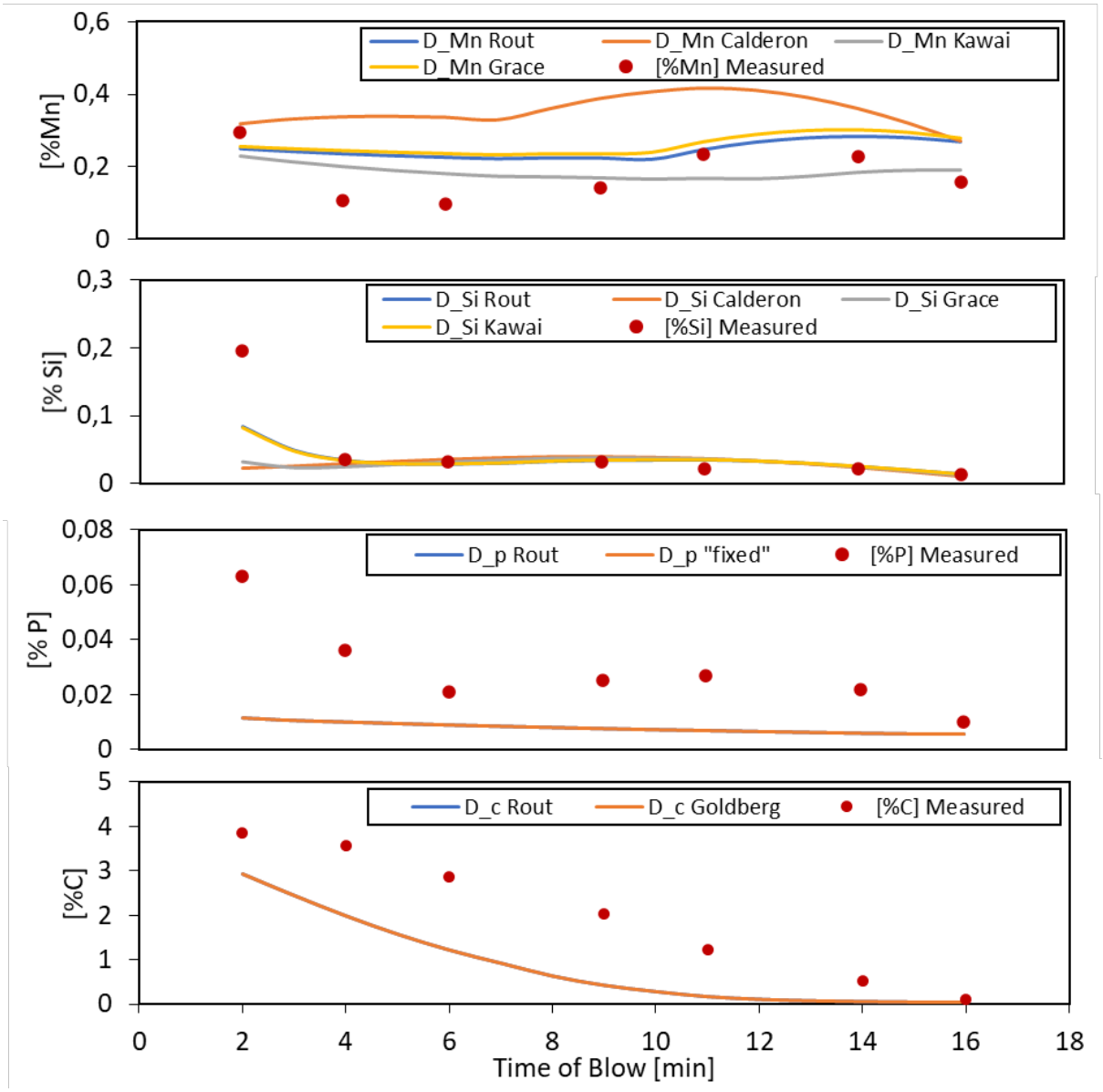

Figure 5-16 Refining rates with different diffusion coefficients; Manganese (top left), Silicon (top right), Phosphorus (bottom left), Carbon (bottom right)

Considering the advantages and disadvantages of the different methods for measuring diffusion coefficients, it would have been expected that the correlation proposed by Calderon et al. [3] produces the best simulation results. However, as depicted in Figure 5-16 there are significant deviations from the measured data for the manganese prediction. For manganese the highest accuracy in prediction is achieved by using the measured diffusion coefficient by Kawai et al. [4].

This aberration can have been caused by the use of an unfitting manganese distribution ratio, a deviation in proposed slag composition in comparison to the real time slag composition, or it could even be traced back to mistake in measuring the diffusion coefficient. The complexity of the posed problem makes it difficult to pinpoint just one possible source of error. For the mathematical model programmed, the diffusion coefficient for manganese with the least mean deviation from the measured value, by Kawai et al. [4], was chosen. As expected the correlation proposed by Calderon et al. [3] for silicon achieves the most accurate prediction for its concentration in the hot metal bath. Therefore it is implemented in the model. Varriing diffusion coefficients for carbon and phosphorus do not impact the refining reaction greatly, thus the diffusion coefficients proposed by Rout et al. are applied.

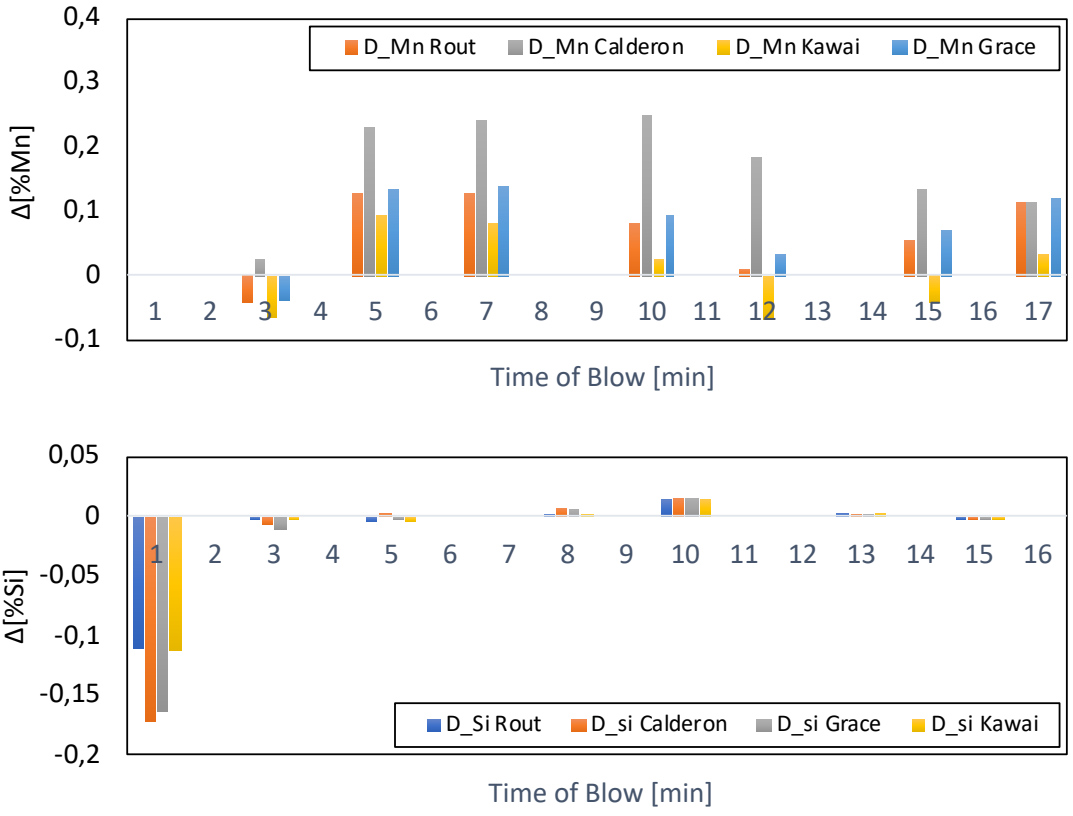

Figure 5-17 Diffusion coefficients: mean deviation from measured data

The slag composition is an extremely influential factor, not only in the real-life process but also in the mathematical model proposed. The distribution ratios for manganese, silicon and phosphorus change greatly depending on the slag composition.

Implementing a dynamic slag composition prediction model, would be a rather time-consuming task and was not attempted in the course of this project. However, it would be a vital next step to enhance the prediction accuracy. The gPROMS model was validated by using the exact measured data as well as a proposed slag composition evolution.

The change in slag composition during the blow implemented in the final model was adopted from the “Fundamentals of Steelmaking” by Turkdogan.

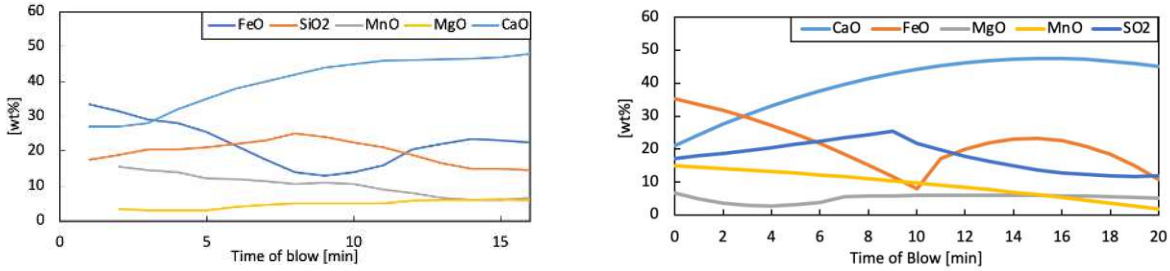

Figure 5-18 (left) slag composition measured by cicutti; (right) imposed slag composition

The simulation results for the slag composition measured by Cicutti [46] and the slag composition proposed, are depicted in Figure 5-18. The impact of different time dependent evolutions on the refining rates is very evident, Figure 5-19. Unexpectedly the simulated silicon refining rate fits the measured one almost perfectly using the proposed slag evolution. The predictions for manganese and phosphorus differ from the measured data, Figure 5-19. However, it has to be noted that the initial concentrations of impurities in the hot metal seem to be too little. The concentrations at minute 0 and minute 2 cannot be the same. These concentrations were adopted as stated in the validation input parameters. If the concentrations at minute 0 were higher, it could be expected that the predictions would not differ that greatly from the measured data.

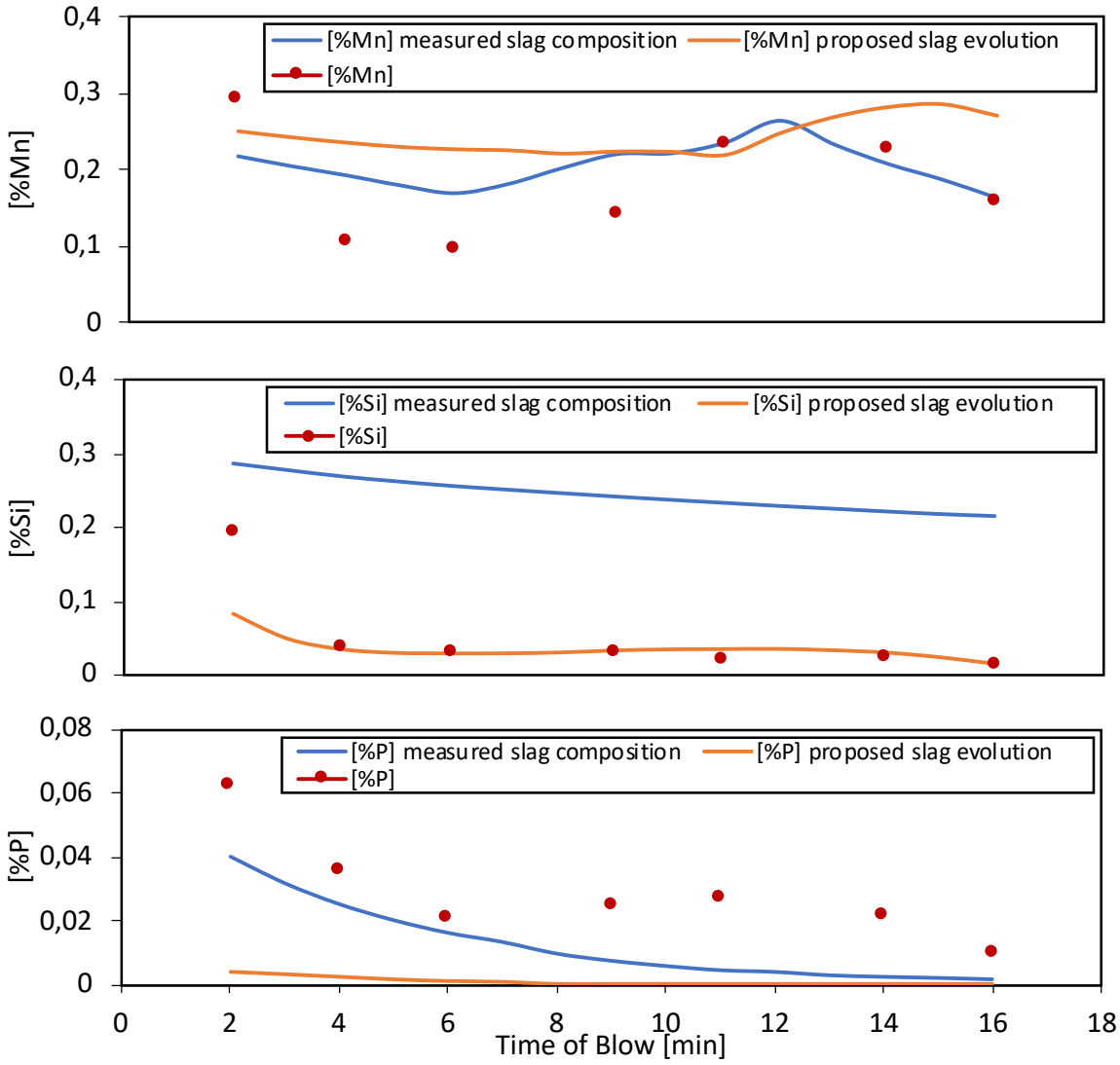

Figure 5-19 Impact of different slag compositions on the simulation results

6 Melting and Dissolution Behaviour

This chapter discusses the melting and dissolution behaviour of different solids. In particular scrap, iron ore and fluxes such as lime and dolomite.

6.1 Scrap Melting

The oxidation reactions happening during the blow, generate a great amount of heat. To be able to reach a target temperature at the end of the treatment it is necessary to control and absorb the heat generated, therefore scrap is charged. Various research groups that have conducted experiments conclude that most of the charged scrap is dissolved within less than ten minutes, regardless of the size of the individual scrap pieces. However, it has been observed that dissolving heavy scrap with a thickness of 40 cm can take up to 16 minutes, while light scrap with a thickness of less than 2 cm is dissolved within less than 5 minutes, [51].

The most influential factors affecting the melting of scrap metal in a furnace include:

1. Metal bath temperature: A higher metal bath temperature will result in faster melting of the scrap, while a lower metal bath temperature will result in slower melting.
2. Scrap temperature: If the scrap added is preheated, it will melt faster than if it is added at room temperature.
3. Carbon content of the metal bath: A higher carbon content in the metal bath will result in faster melting of the scrap, while a lower carbon content will result in slower melting. This correlation can be observed in the Fe-C-diagram Figure 2-3 provided on page 5.
4. Carbon content of the scrap: Scrap with a higher carbon content will melt faster than scrap with a lower carbon content.
5. Hot metal bath stirring through top and bottom blow: Stirring the metal bath through top and bottom blowing can increase the heat transfer and thus result in faster melting of the scrap.

6. Size of the surface area of scrap: Larger surface area will increase the heat transfer and thus result in faster melting of the scrap.

6.1.1 Model Options

In this study, two submodels are implemented to simulate the scrap melting process. The choice between these models depends on the desired level of accuracy and the availability of information. The two models primarily differ in complexity and thus detail of output generated.

6.1.1.1 Detailed Model

The mathematical model presented in the doctoral thesis by Ajay Kumar Shukla [51], referred to as the "detailed model", describes the phenomenon of scrap dissolution based on mass and heat transfer. The mass transfer coefficient is calculated assuming forced convection, invoking the Chilton-Colburn analogy and the heat transfer coefficient is a function of mixing energy represented by 61-63 and can solved using Quasi-Static approach [51].

$$\frac{dL}{dt} = \frac{\sum_{n=1}^{\infty} -\frac{A_n}{n\pi}(1-\cos(n\pi))\lambda^2 k_{sc} L e^{-\lambda\alpha_{sc}t} - h(T_b - T'_m)}{\rho_{sc}\left(\Delta H_{sc} + C_{P,sc}(T_b - T'_m)\right) - \sum_{n=1}^{\infty}\frac{A_n}{n\pi}(1-\cos(n\pi))(\rho_{sc}C_{P,sc} + 2\lambda^2 k_{sc}t)e^{-\lambda\alpha_{sc}t}} \quad \text{Eq. 56}$$

$$\lambda = \left(\frac{n\pi}{2L(t)}\right) \quad \text{Eq. 57}$$

$$A_n = 2(T_{sc0} - T'_m)\frac{1-\cos(n\pi)}{n\pi} \quad \text{Eq. 58}$$

Furthermore, increasing the complexity of this model is the effect of carbon content on the melting process. Assuming the interfacial carbon content to be equal to the carbon content in the metal bath [23], considers that the carbon of the bath migrates to the scrap surface lowering the melting temperature of the scrap. The drawback of this assumption is that similar scrap types all melt at the same time even though they do not have the same carbon content.

All influential factors discussed during the introduction of this chapter are considered in the detailed model. Thereby providing a more accurate simulation of the melting of scrap, while deepening the understanding on how different conditions affect the process. However, it is important to acknowledge that even with the level of detail incorporated into the model, it

cannot fully replicate reality. Therefore, certain assumptions need to be made in order to simplify the complexity of the process and implement the model successfully. These assumptions are summarized in Table 3.

6.1.1.2 "Simple" model

The "simple" scrap melting model proposed by [52] is an alternative to the more detailed model, that allows the user to simulate the process of melting scrap metal in a furnace with fewer assumptions, summarized in Table 3.

The weight change of scrap is described as follows:

$$\frac{dW_{sc}}{dt} = \frac{-M_{Fe} k_{ther1} k_{area1} W_{sc} (T_b - T_{sc}) \left(\frac{T_{sc}}{T_b}\right)}{(\lambda_{Fe} + C_{P,Fe(s)})(T_b - T_{sc})} \qquad \text{Eq. 59}$$

$$\text{with } k_{ther1} = 0.4 \frac{kW}{Km^2} \qquad k_{area1} = 0.005 \frac{m^2}{kg}$$

The scrap temperature development with respect to time is described by the heat transferred as follows:

$$\frac{dT_{sc}}{dt} = \frac{(k_{ther1} k_{area1} W_{sc} (T_b - T_{sc}))}{W_{sc} C_{P,Fe(s)} / M_{Fe}} \qquad \text{Eq. 60}$$

6.1.1.3 Implementation

The user can choose between the two presented model options, when providing the input parameters depending on the desired accuracy of the melting process prediction and the information available. Either model adds the scrap at minute zero and then melts it during the course of the main blow. There is no option for further scrap addition during the blow because it is typically not practised. The two models mainly differ in their complexity and the extent of simulated details. Both models make various assumptions which are summarized in Table 3.

Both the detailed and simple scrap melting models offer their own distinct advantages and are implemented in a way that the impurities transfer into the hot metal bath and thus influence the refining rates.

The simple model, with its less demanding input requirements, provides a straightforward and user-friendly approach, making it accessible to users with limited information. Despite its simplicity, the model accurately describes the melting rate, aligning well with existing literature.

Assumption	
Both models consider the scrap is fully submerged in the metal bath which eliminates the need to model the effects of partial submergence.	
Detailed Model	
The heat transfer occurs only in the axial direction.	
The physical properties of the plate are constant.	
Simple Model	
The scrap melting rate is proportional to the heat transfer rate from the liquid to the solid which eliminates the need to model the effects of heat transfer in multiple directions.	
The heat transfer coefficient is imposed.	
The specific reaction interface is imposed.	
Input Parameters	
Detailed Model	**Simple Model**
Scrap weight [kg] or number of scrap pieces	Scrap weight [kg]
Scrap composition [wt%]:	Scrap composition [wt%]:
Silicon, Manganese, Carbon	Silicon, Manganese, Carbon
Scrap size:	
Length [m], Thickness [m]	

Table 3 Scrap melting model assumptions, simplifications and input parameters

In contrast, the detailed quasi-static approach offers a high level of accuracy in representing the cooling effects of scrap by also considering conversion heat and reduction heat. Additionally, this approach includes a heat balance which can be easily interconnected with other reactions in the basic oxygen furnace model. This is a great advantage if the overall model is developed further in the future. Similar to the simple model, it considers the influence of scrap melting on the weight and composition of the hot metal bath, as well as the modification of slag composition due to impurities. However, the detailed model requires more extensive input information compared to the simple model.

6.1.2 Validation

The melting rate of a scrap charge of 30 ton in a 200 ton converter was simulated using either model. Both submodels presented calculate plausible melting rates in comparison to literature and the opinion of experts. Literature suggests that most of the scrap is molten within less than 10 minutes of the blowing process. The simple model melts the 30 ton scrap charge within less than 10 minutes. The detailed model depicts the melting rate of different scrap sizes and melts the total scrap charge in approximately 10 minutes.

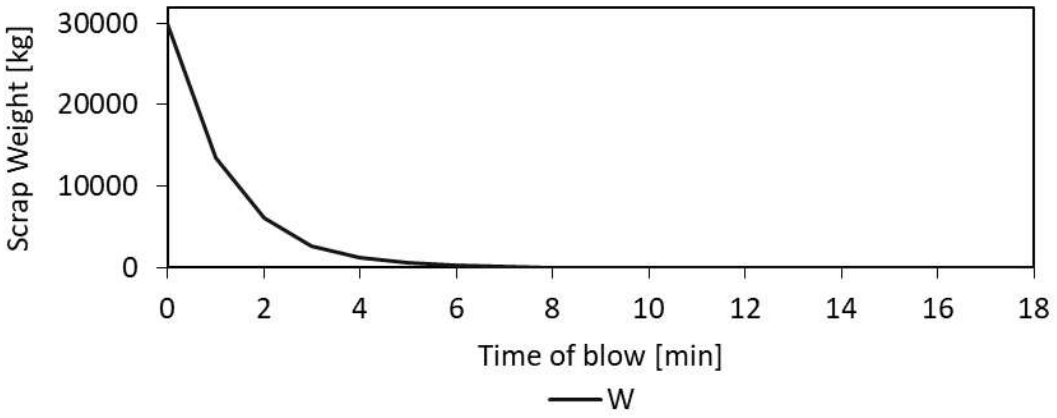

Figure 6-1 Change of scrap weight, modelled using the "simple" approach.

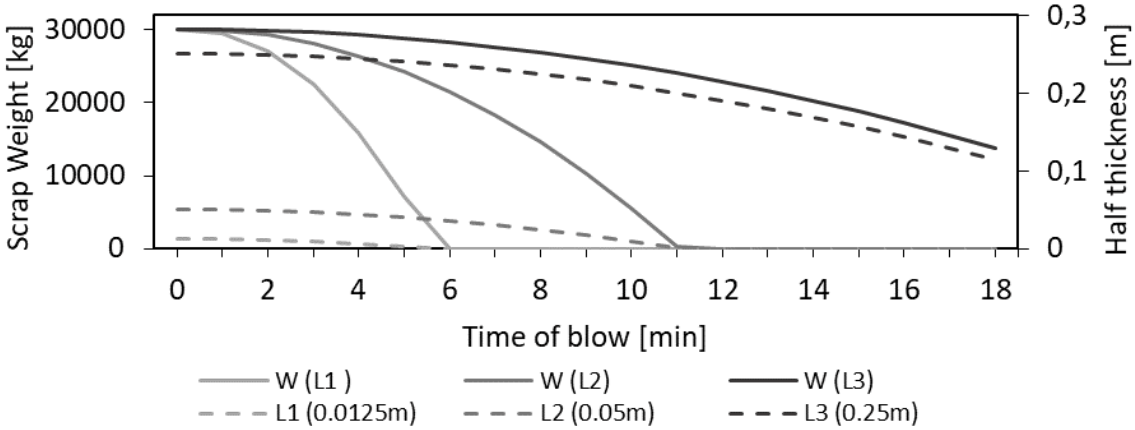

Figure 6-2 Change of scrap thickness using the "detailed" approach.

Ultimately, the choice between the two models depends on the available data and the level of detail desired in the simulation. Both models contribute valuable insights into the scrap melting process, allowing for a comprehensive understanding of its dynamics and effects within the overall steelmaking process.

6.2 Iron Ore Dissolution

Iron ore is commonly charged into the steelmaking process either before or during the blow to serve as a coolant for the metal bath. Its cooling effect is approximately three times that of scrap, although the mass of iron ore charged is usually very little in comparison to the metal bath and scrap. Therefore, a relatively simple model is used to describe the cooling effect. The model is similar to the "simple" scrap model used. Iron ore typically comes in the form of lumps or pellets, and its chemical composition differ greatly depending on the deposit, as shown in Figure 6-3. However, the main element in the samples is iron, with only a relatively low amount of residual elements present.

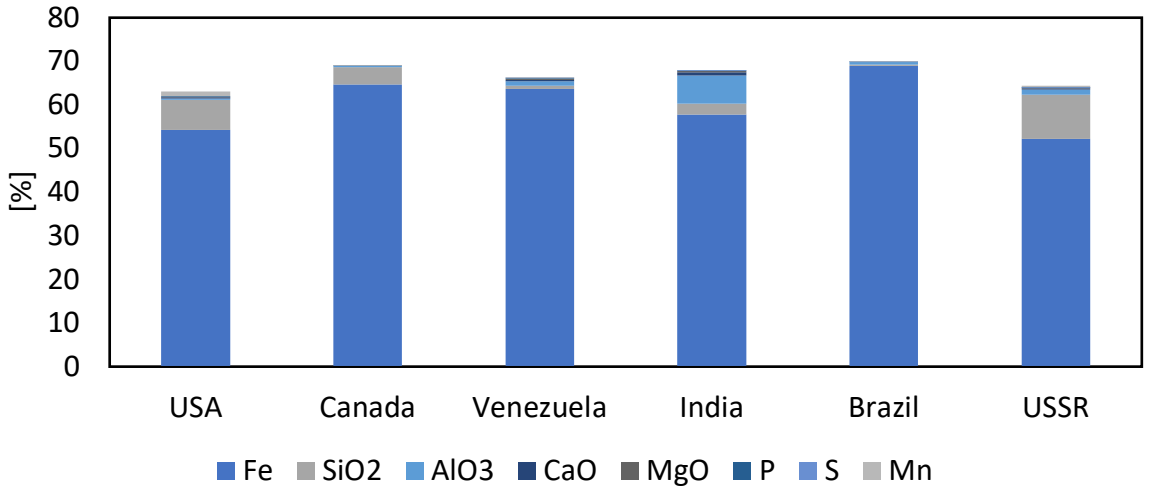

Figure 6-3 Iron ore chemical composition; visualization of the values provided in [6]

The model incorporates the endothermic reaction of iron oxide reduction in the ore, as shown in Eq. *61*, which releases a significant amount of gas and contributes to slag foaming.

$$Fe_3O_4 + [C] \rightarrow (3FeO) + CO_{(g)} \quad \Delta H^{rxn} = -184.660\ kJ/mol \qquad \text{Eq. 61}$$

The iron ore dissolution subprocess simulates the dissolution of iron ore into a molten metal bath, and certain assumptions are made to simplify the complexity of the process, as proposed by [21]. Firstly (1), the model assumes that the iron ore particles are spherical, simplifying the calculations related to the surface area of the particles. Secondly (2), the temperature is uniform within the particle, and that at the time of charge the iron ore particles instantaneously assume the temperature of the hot metal bath. Thirdly (3), all iron in the iron ore is in the form of magnetite, simplifying the calculations by disregarding the presence of other minerals. Fourthly (4), a empirically specified fraction of the total heat

contributes to the melting of iron ore, while the remainder is used for sensible heating. This implies that a certain proportion of the heat raises the temperature of the iron ore, while the rest is utilized for melting it. Fifthly (5), as long as the temperature of the ore is lower than that of the metal bath, the heat is used to heat up the iron ore. When temperature of the iron ore approaches that of the metal bath, a fraction of total heat is employed to increase the melting rate. These assumptions collectively enable a more accurate simulation of the iron ore dissolution process in the molten metal bath and facilitate the understanding of how different conditions affect the process.

The submodel begins by calculating the total heat transferred to the surface of an iron ore particle, followed by estimating the heat consumed by the reduction reaction and the melting process. This estimation leads to the determination of the melting rate for iron oxide.

$$Q_{conv,ore} = 4\pi r_{ore}^2 h_{ore}(T_s - T_{ore}) \quad \text{Eq. 62}$$

$$Q_{red,ore} = \frac{\gamma_{Fe,ore}}{3M_{Fe}} \dot{W}_{ore,melt} \Delta H_{ore} \quad \text{Eq. 63}$$

$$Q_{ore} = n_{ore}\left(Q_{conv,ore} + Q_{red,ore}\right) \quad \text{Eq. 64}$$

$$\dot{W}_{ore,melt} = -4\pi \rho_{ore} r_{ore}^2 \frac{dr_{ore}}{dt} \quad \text{Eq. 65}$$

A simulation was conducted using this approach for two different particle sizes and the necessary parameters and initial values needed to run the simulation are provided in Table 4.

Parameters		
h_{ore}	2500	[W/m^{2}K]
$C_{p,ore}$	200,83	[J/molK]
ρ_{ore}	2,88	[kg/m^3]
ΔH_{ore}	184,66	[kJ/mol]
M_{Fe}	0,02809	[kg/mol]
$\gamma_{Fe,ore}$	0,7	[-]

Initial Values			
Set A	Particle radius	0,03	[m]
	Temperature	303	[K]
	Iron ore	1700	[kg]
Set B	Particle radius	0,015	[m]
	Temperature	303	[K]
	Iron ore	1700	[kg]

Table 4 Parameters for iron ore dissolution (left); Initial values for simulations (right)

The simulation results shown in Figure 6-4 illustrate the melting behavior of iron ore for two different particle radii. The charge with smaller particles exhibits a slower decrease in radius, which can be attributed to Eq. 62. As the particle radius decreases, the total heat transferred to the surface of an iron ore particle decreases as well.

The model presented provides valuable insights into the factors influencing the iron ore melting rate, including temperature, heat transfer, and iron ore properties. However, it is important to acknowledge that the real iron ore melting process involves additional factors, such as chemical reactions and the presence of other minerals.

The simulation results demonstrate that smaller particles exhibit a slower melting rate, Figure 6-4. This observation aligns with well-established principles in heat transfer research. As the size of a particle decreases, the heat transfer to its surface decreases due to the decreasing ratio of surface area to volume. Since heat transfer primarily occurs at the surface of the particle, a smaller particle will have a lower rate of heat transfer than a larger particle of the same material. In the context of iron ore dissolution, it is reasonable to expect that as the particles become smaller, the decrease of particle radius during the melting process will slow down. As the particles get smaller, the heat transfer to the surface of the particle decreases, which means that less heat is available to melt the particle. This will result in a slower melting rate for smaller particles.

In conclusion, the model provides a plausible explanation for the observed slower melting rate of smaller particles based on heat transfer principles. However, further research and experimentation are needed to validate and refine these findings, especially considering the complex nature of the iron ore melting process and the presence of other factors such as chemical reactions and additional minerals.

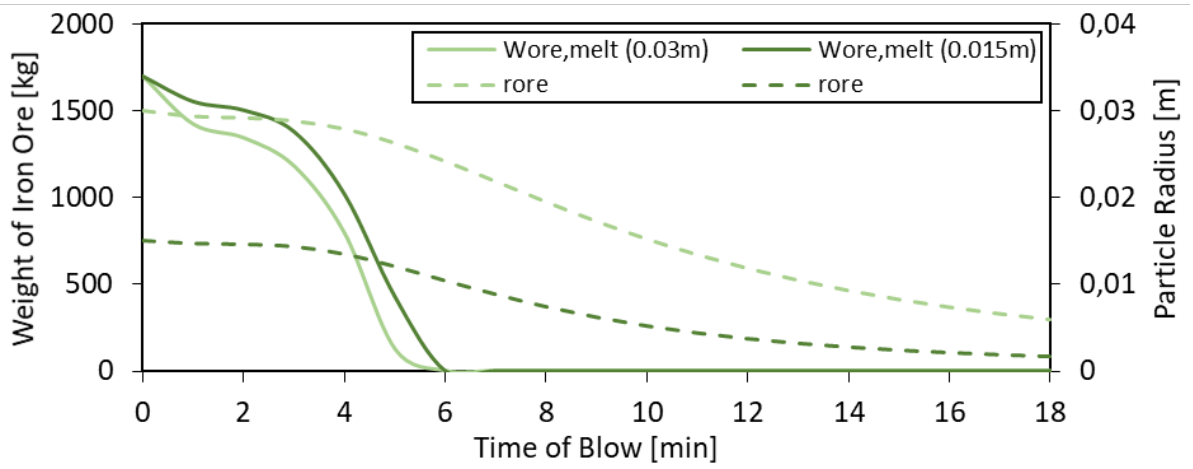

Figure 6-4 Simulation results: Dissolution of iron ore with various particle sizes

6.3 FLUX DISSOLUTION

To accurately depict the dissolution of fluxes in the model, the approach proposed by Dogan et. al [18] was adopted. The two fluxes considered for dissolution are the solid oxides dolomite and lime, with their main components assumed to be magnesium oxide (MgO) and calcium oxide (CaO), respectively. The key factors that influence the dissolution process include the slag temperature, the composition, and the bath mixing. Various studies have been conducted on the dissolution mechanisms [18] indicating that the content of FeO in the slag phase is the most influential factor for the CaO and MgO diffusion out of the dolomite. When the FeO concentration exceeds 20% by mass, the diffusion of MgO through a boundary layer is the rate limiting step, as described by Eq. 67. Conversely, when the FeO concentration is below that threshold, the diffusion of CaO through the boundary layer becomes rate-limiting.

To solve Eq. 67 and Eq. 68, the mass transfer coefficients for dolomite and lime are estimated based on the particle settling velocity, taking into account the effects of bath mixing and foaming due to rising CO gas bubbles. The rising CO bubbles are generated by the decarburization reaction during the blow and enhance the mass transfer rate.

The model makes certain assumptions regarding the flux particles:

- Spherical shape: The flux particles are assumed to have a spherical shape. This simplifying assumption allows for easier calculation of their dissolution properties.
- Proportional dissolution: The dissolution of flux particles is assumed to be proportional to the rate of change of their radius. This assumption provides a relationship between the dissolution rate and the changing size of the particles.

To determine the saturation percentage of CaO Eq. *66*, the model incorporates the nonlinear regression proposed by Dering et. al [21]. Additionally, the energy balance for a uniform flux particle (Eq. 70) and the rate at which the heat is absorbed by the flux particles (Eq. 69) are considered in the calculation process.

$$C_{s,CaO_{sat}} = \frac{3.52T_s - 4823.7e^{-\frac{2.93}{100}C_{s,SiO_2}} + 12.4C_{s,FeO} - 9.71C_{s,MgO} + 17.9C_{s,CaO}}{100} \quad \text{Eq. 66}$$

$$\frac{dr_{Dolomite}}{dt} = \begin{cases} \alpha_{MgO}^{p} k_D \frac{\rho_s}{100\rho_{MgO}} \left(1 + \frac{M_{MgO}}{M_{CaO}}\right) \left(C_{s,CaO} - C_{s,CaO_{sat}}\right), C_{s,FeO} < 20\% \\ \alpha_{MgO}^{p} k_D \frac{\rho_s}{100\rho_{MgO}} \left(1 + \frac{M_{CaO}}{M_{MgO}}\right) \left(C_{s,MgO} - C_{s,MgO_{sat}}\right), C_{s,FeO} \geq 20\% \end{cases} \quad \text{Eq. 67}$$

$$\frac{dr_{Lime}}{dt} = \alpha_{CaO}^{p} k_{CaO} \frac{\rho_s}{100\rho_{CaO}} \left(C_{s,CaO} - C_{s,CaO_{sat}}\right) \quad \text{Eq. 68}$$

$$Q_{flux} = 4\pi \sum_i r_i^2 h_i n_i (T_s - T_i) \;\; i \in \{Lime, Dolomite\} \quad \text{Eq. 69}$$

$$W_i C_{P,i} \rho_i \frac{dT_i}{dt} = 4\pi r_i^2 h_i n_i (T_s - T_i) \; i \in \{Lime, Dolomite\} \quad \text{Eq. 70}$$

$$W_i = \frac{4}{3} \pi r_i^3 \rho_i \quad \text{Eq. 71}$$

6.3.1 Dolomite and Lime

To estimate the dolomite or lime dissolution rate, the model first calculates the particle settling velocity, which is then used to determine the mass transfer coefficient. This calculation is performed for each point in time as long as the radius of the dolomite particle is greater than zero. The subscript i stands for dolomite (MgO) and lime (CaO).

$$u_i = \left[\frac{(\rho_s - \rho_i) g}{9\sqrt{\mu_s \rho_s}}\right]^{2/3} d_{particle} \quad \text{Eq. 72}$$

For the estimation of the mass transfer coefficient of spherical, solid particles a semi-empirical relationship based on Sherwood, Reynolds and Schmidt numbers is used. This approach is well-established and widely used for the estimation of mass transfer coefficients of different shaped solids involved in steelmaking [18].

$$Re_i = u_i 2r_{particle} \frac{\rho_{slag}}{\mu_{slag}} \quad \text{Eq. 73}$$

$$Sh_i = 1 + 0.724 \cdot nes^{0.48} \cdot Re_i^{0.48} Sc_i^{1/3} \quad \text{Eq. 74}$$

$$k_i = \frac{Sh_i D_i}{2r_{particle}} \quad \text{Eq. 75}$$

$$D_i = A_i \frac{T_{slag}}{\mu_{slag}} \quad \text{Eq. 76}$$

6.3.2 Validation

Figure 6-5 illustrates the dissolution behavior of dolomite and lime particles, showcasing the evolution of their radii after being charged into the converter. For this example, dolomite is charged at minute 3, while lime is charged at minute 1 during the main blow, which can vary depending on the operation parameters. The observed dissolution kinetics and behavior in this study are consistent with the findings reported in the literature.

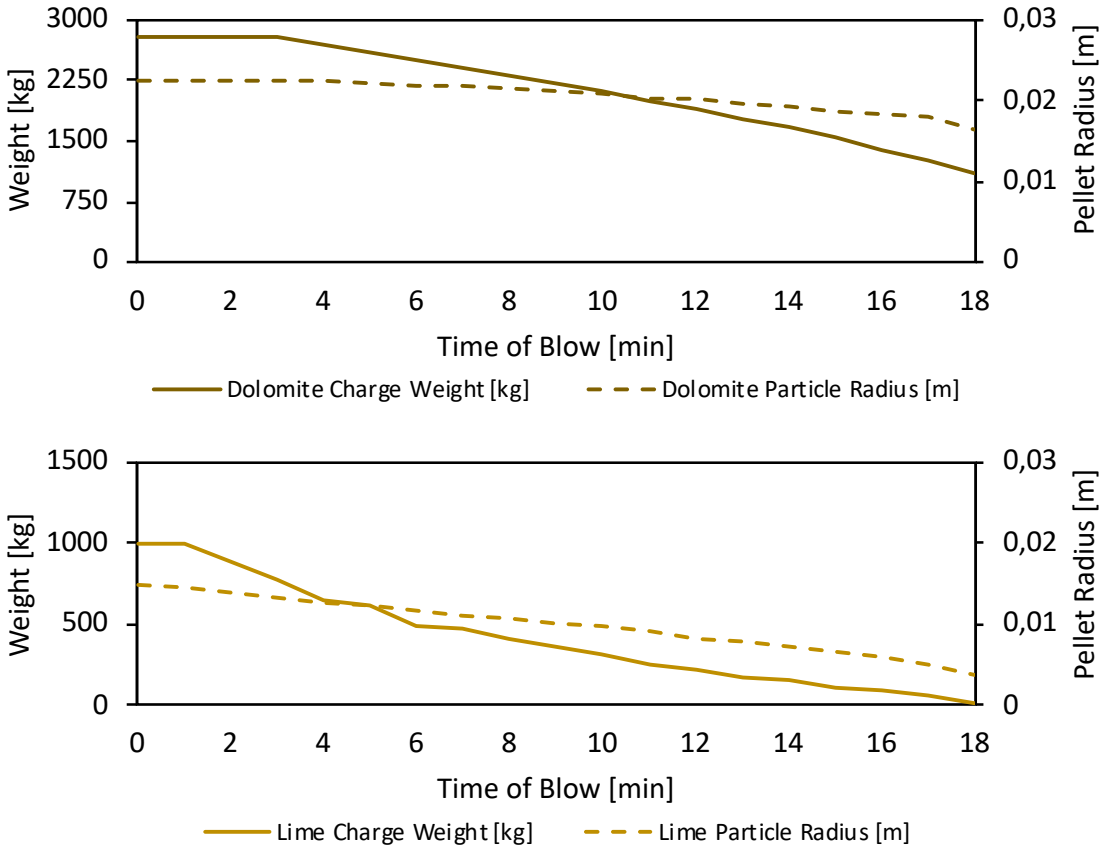

Figure 6-5 Dolomite and lime dissolution behavior

7 VALIDATION OVERALL MODEL

For the validation of the overall model two simulations with two different datasets available in literature were run and compared to simulations done by other research groups. These datasets consist of a description of the basic oxygen furnace geometry and measured hot metal bath compositions at different points in time during the blow.

7.1 200 TON CONVERTER

The input parameters for the simulation of the 200 ton converter were taken from [46] and are summarized in Table 5. These parameters define the initial conditions and characteristics of the converter and its contents at the start of the simulation.

Hot metal bath weight		170000	[kg]
Hot metal bath temperature		1623 to 1923	[K]
Initial hot metal composition	Carbon	3.86	[wt%]
	Silicon	0.19	[wt%]
	Manganese	0.29	[wt%]
	Phosphorus	0.065	[wt%]
Scrap weight		30000	[kg]
Scrap composition	Carbon	0.08	[wt%]
	Silicon	0.001	[wt%]
	Manganese	0.52	[wt%]
Oxygen blow		620	[Nm^3/min]
Lance nozzle		6 hole	
Diffusion coefficient in metal phase at 1873 K	Carbon	$2.0x10^{-9}$	[m^2/s]
	Silicon	$3.8x10^{-9}$	[m^2/s]
	Manganese	$3.7x10^{-9}$	[m^2/s]
	Phosphorus	$4.7x10^{-9}$	[m^2/s]
Gas fraction in emulsion		0.8	
Angle of droplet ejection		60	[°]

Table 5 The input parameters for a 200 ton converter as described by [46]

The operation parameters provided by the literature source [46] are summarized in Figure 7-1. The operation parameters that are provided by the literature source are represented by dotted lines whereas the imposed operation parameters are represented by solid lines.

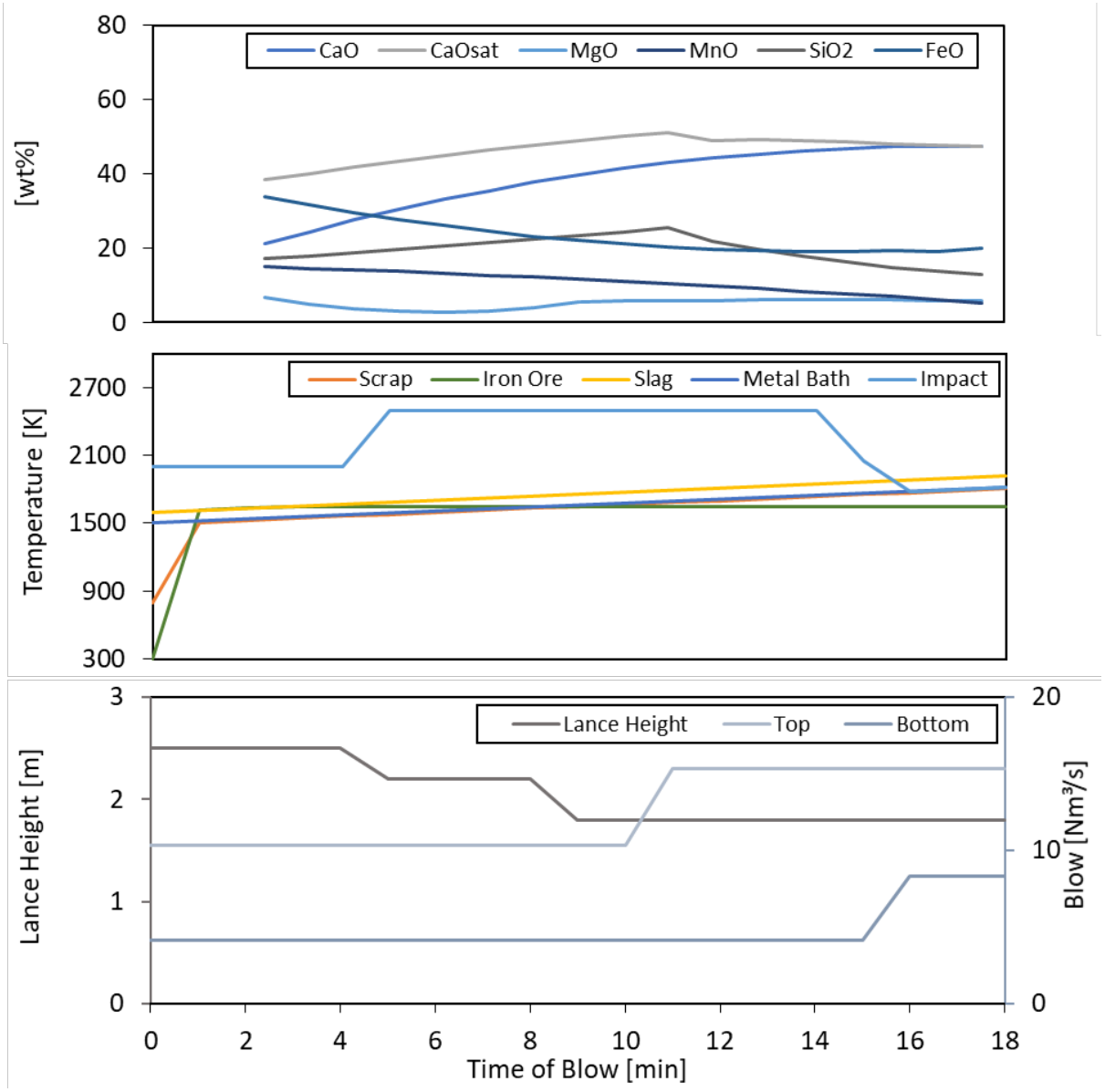

Figure 7-1 (top) Evolution of slag composition for a 200 ton converter; (middle) Temperature profile for a 200 ton converter; (bottom) Operation parameters 200 ton converter: Volume flow and lance height

7.1.1 Decarburization

According to the findings presented in Figure 7-2, the simulation results are in good agreement with the measured data. It is very plausible that most of the carbon is removed in the emulsion zone. The yellow curve illustrating the decarburization process in the emulsion

zone, has two sharp increments at minute 8 and 11 which can be attributed to the repositioning of the lance. This repositioning results in a reduced distance between the lance and the surface of the hot metal bath, consequently inducing momentary splashing and an augmented production of droplets. This, in turn, leads to the expansion of the reaction interface, thereby elevating the rate at which carbon is eliminated.

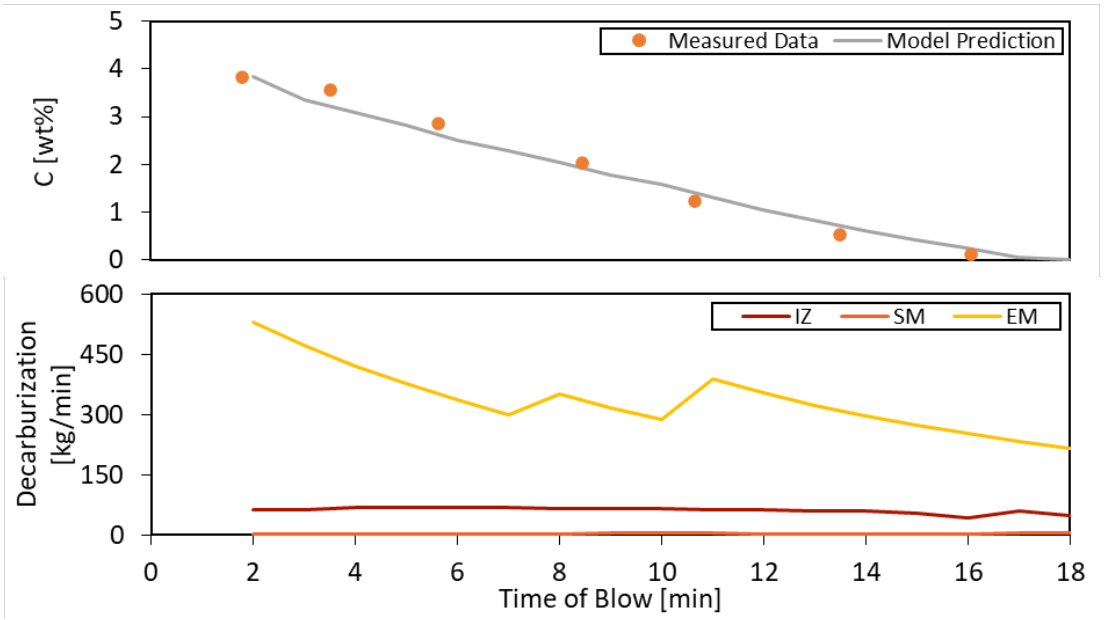

Figure 7-2 200 ton Converter: (top) Carbon content during blow, (bottom) decarburization rate depending on the reaction interface: impact zone (IZ), slag metal zone (SM), emulsion zone (EM)

Further the carbon content prediction was compared to simulations conducted by other research groups as well as the measured data provided by [46]. The prediction is in very good agreement with the measured data as shown in Figure 7-3.

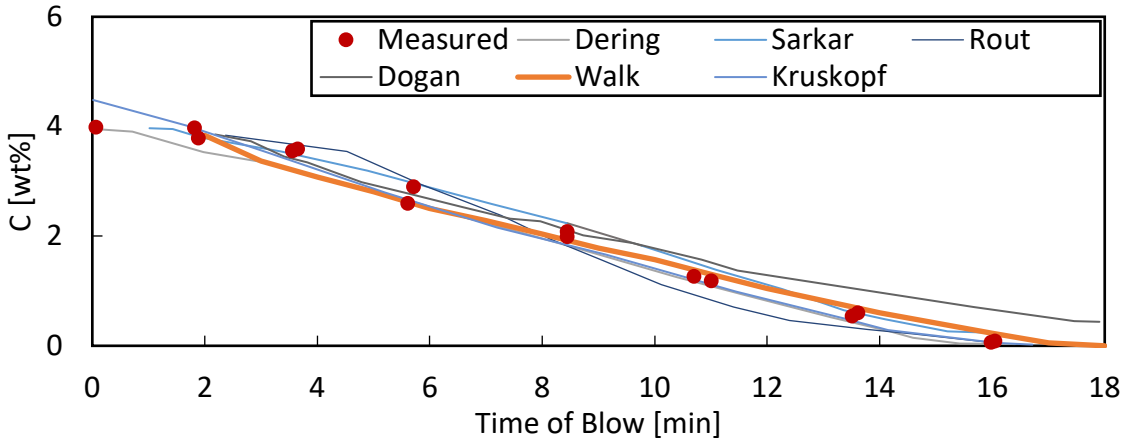

Figure 7-3 Comparison of carbon content simulations of different research groups

7.1.2 Desiliconization

The prediction of silicon content in the hot metal bath over time is in good accordance with the measured data, as depicted in Figure 7-4. However, it is noteworthy that during the time interval from minute 9 to 12, as well as in the initial stages, certain deviations from the measured data are observed.

These discrepancies can potentially be attributed to the evolution of iron oxide content within the slag, which serves as the primary influential factor in the equilibrium concentration modeling of desiliconization. It is likely that a more comprehensive and detailed model encompassing the evolution of the slag would further enhance the accuracy of the silicon content prediction.

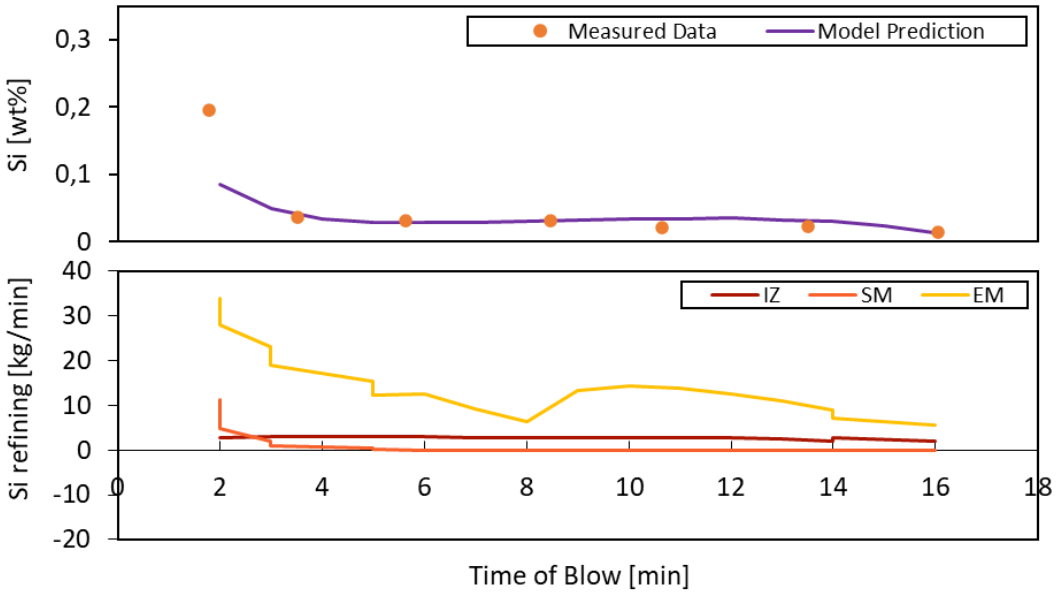

Figure 7-4 200 ton Converter: (top) Silicon content during blow, (bottom) desiliconization rate depending on the reaction interface: impact zone (IZ), slag metal zone (SM), emulsion zone (EM)

7.1.3 Manganese removal

The removal rate of manganese exhibits good agreement with the measured data, particularly in relation to the end point composition, as depicted in Figure 7-5. Between minute 2 and 10 the simulated composition differs noteworthily from the measured data. This is due to the assumption that the post combustion ratio is constant which “hinders” the forward and backward reaction. However, the change in slag composition drives the backward reaction at the emulsion interface as it is shown in Figure 7-5 on the right. By incorporating a dynamic

post-combustion ratio that is based on the off-gas composition, it would be feasible to calculate the fluctuations in manganese composition, characterized by the "dip" and subsequent "rise".

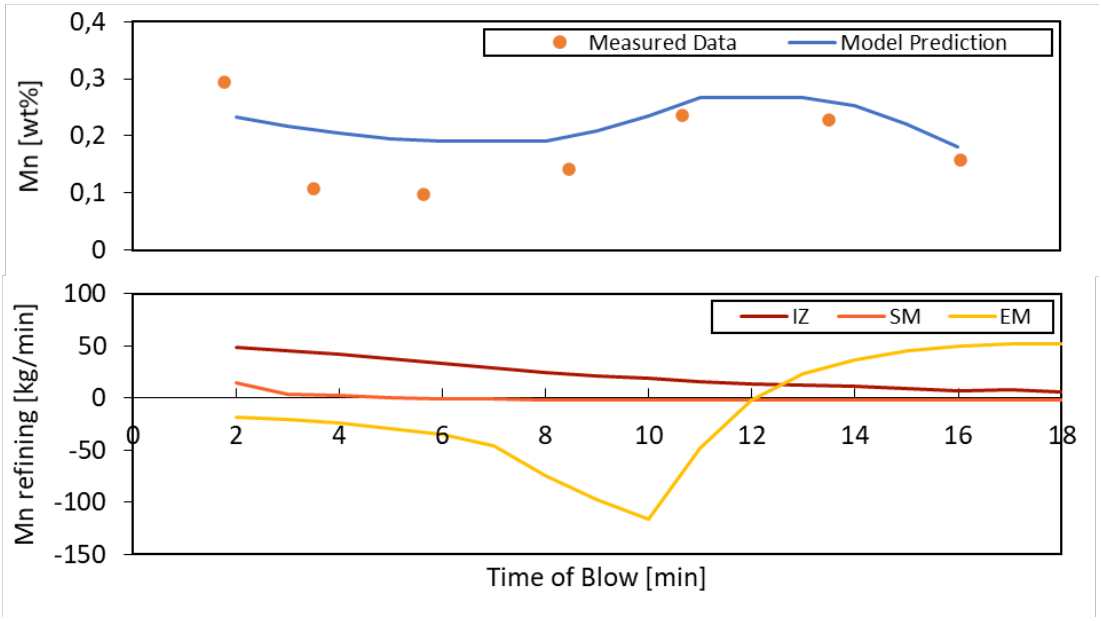

Figure 7-5 200 ton Converter: (top) Manganese content during blow, (bottom) manganese removal rate depending on the reaction interface: impact zone (IZ), slag metal zone (SM), emulsion zone (EM)

7.1.4 Dephosphorization

Figure 7-6 depicts the evolution of the dephosphorization process. However, it is observed that the predicted phosphorus content deviates noticeably from the measured data, particularly during the time interval from minute 9 to 13. During this specific period, the phosphorus backward reaction should dominate at the interface between the slag and metal. Nevertheless, due to the current implementation of the slag evolution, the calculation of the phosphorus distribution ratio necessary for determining the backward reaction is not triggered. It is important to note that the accuracy of dephosphorization modeling heavily relies on the composition of the slag. Therefore, incorporating a dynamic slag composition model would significantly enhance the accuracy of predicting the phosphorus content in the hot metal bath.

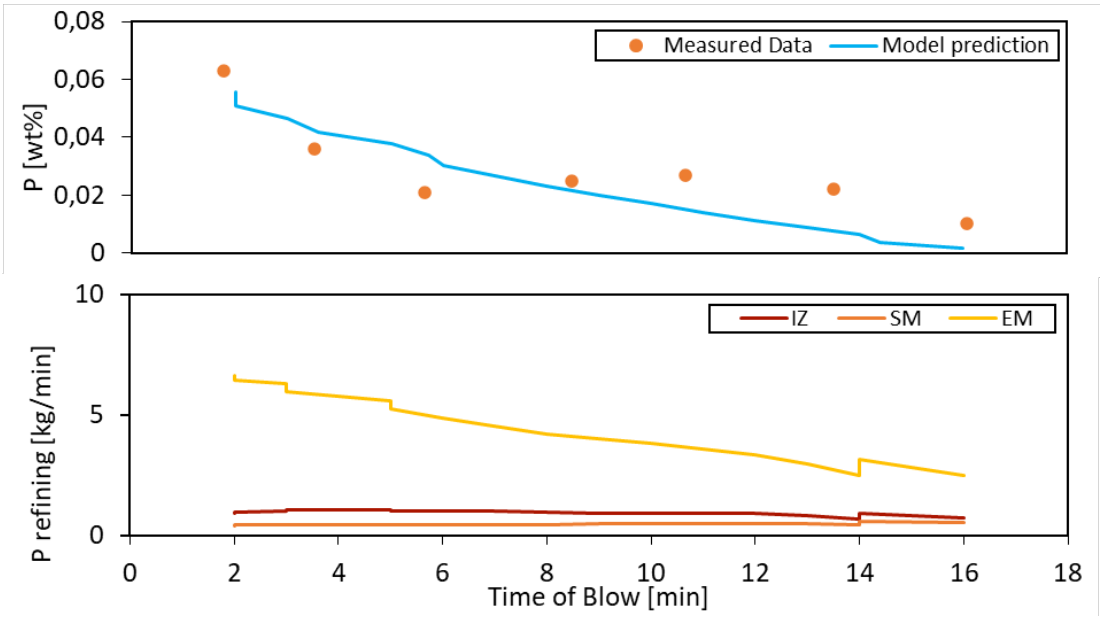

Figure 7-6 200 ton Converter: (top) Phosphorus content during blow, (bottom) dephosphorization rate depending on the reaction interface: impact zone (IZ), slag metal zone (SM), emulsion zone (EM)

7.2 50 TON CONVERTER

The input parameters for the simulation of the 50 ton converter were taken from [53] and are summarized in Table 6. These parameters define the initial conditions and characteristics of the converter and its contents at the start of the simulation.

Hot metal bath weight		48000	[kg]
Hot metal bath temperature		1603 to 1973	[K]
Initial hot metal composition	Carbon	3.88	[wt%]
	Silicon	0.073	[wt%]
	Manganese	0.2	[wt%]
	Phosphorus	0.026	[wt%]
Scrap weight		5000	[kg]
Scrap composition	Carbon	0.08	[wt%]
	Silicon	0.001	[wt%]
	Manganese	0.52	[wt%]
Oxygen blow		130	[Nm^3/min]
Lance nozzle		3 hole	
Lance angle		15	[°]
Diffusion coefficient in metal phase at 1873 K	Carbon	$2.0x10^{-9}$	[m^2/s]
	Silicon	$3.8x10^{-9}$	[m^2/s]
	Manganese	$3.7x10^{-9}$	[m^2/s]
	Phosphorus	$4.7x10^{-9}$	[m^2/s]
Gas fraction in emulsion		0.8	
Angle of droplet ejection		60	[°]

Table 6 Input parameters for 50 ton converter as presented in [46] and [54]

The operation parameters provided by the literature source [53] are summarized in Figure 7-7.

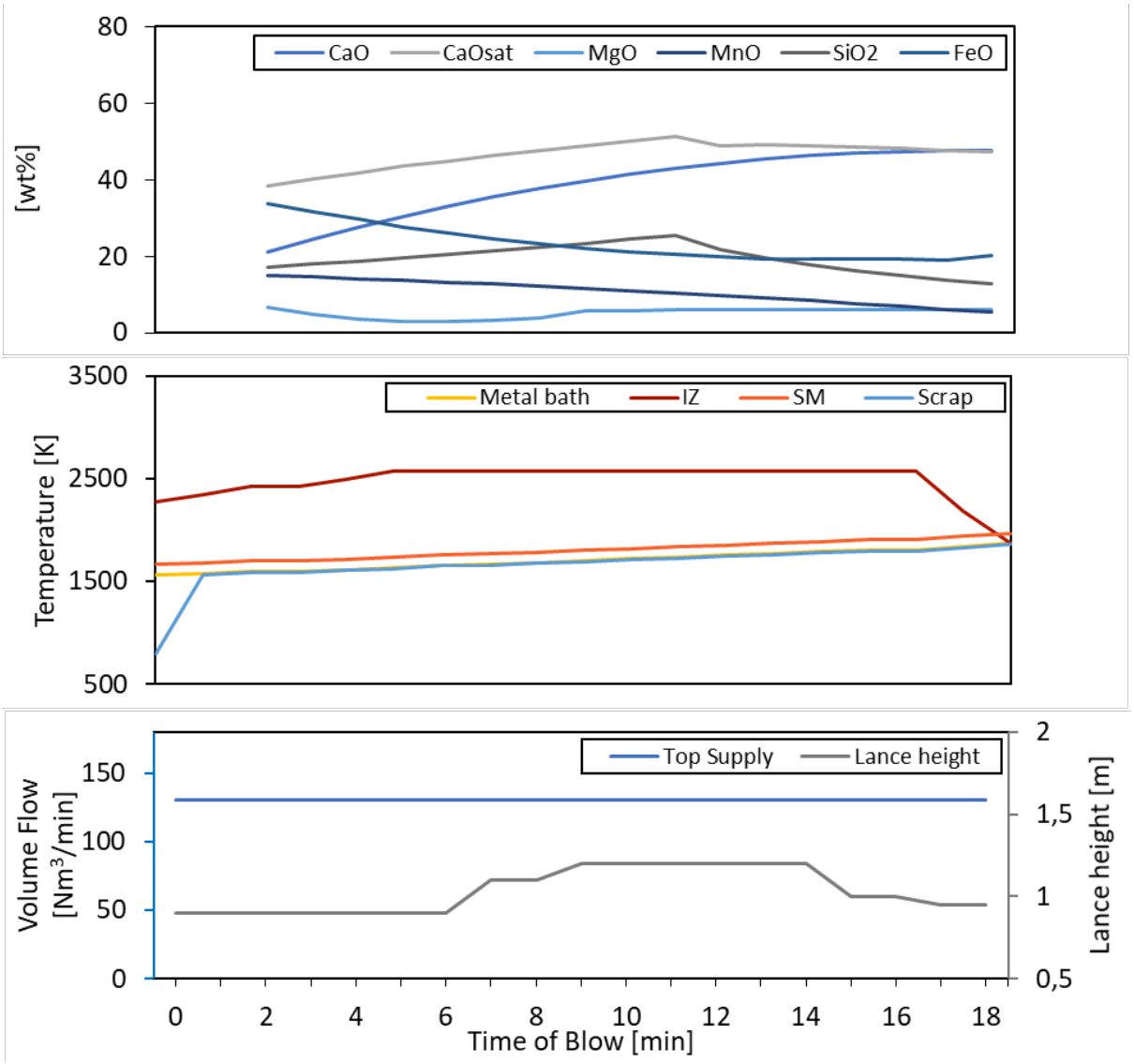

Figure 7-7 (top) Evolution of slag composition for a 50 ton converter; (middle) Temperature profile for a 50 ton converter; (bottom) Operation parameters 50 ton converter: Volume flow and lance height

7.2.1 Decarburization

The predicted decarburization with respect to time is in good accordance with the measured data, Figure 7-8, especially during the second half of the blow. The slight discrepancy in the beginning might be due to the imposed slag composition or the fixed postcombustion ratio differing from the real blow condition.

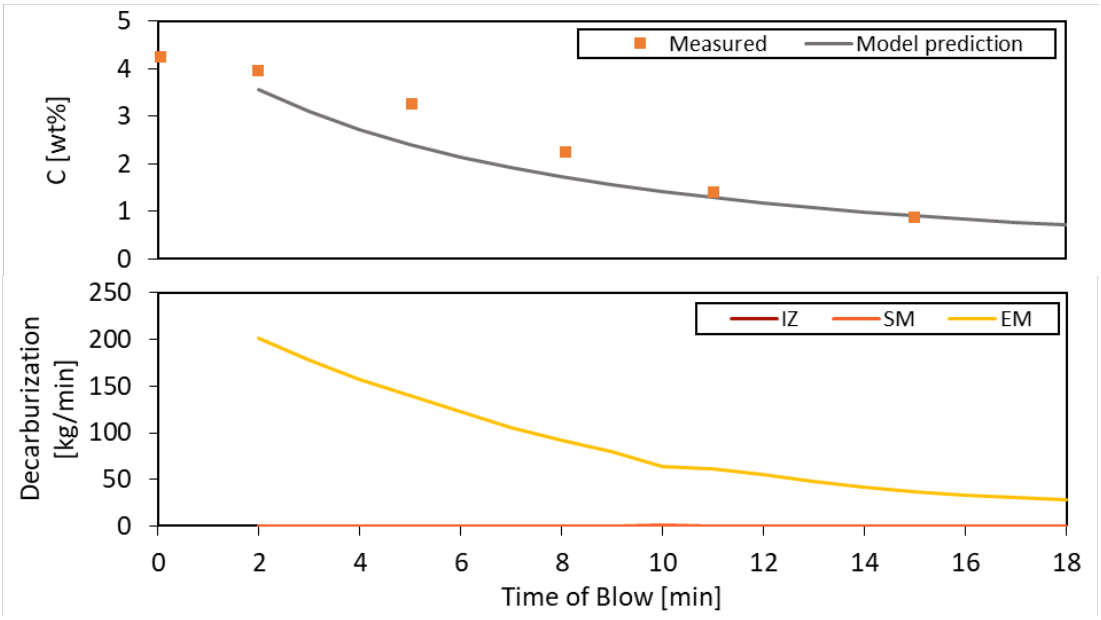

Figure 7-8 50 ton Converter: (top) Carbon content during blow, (bottom) decarburization rate depending on the reaction interface: impact zone (IZ), slag metal zone (SM), emulsion zone (EM)

7.2.2 Refining rates

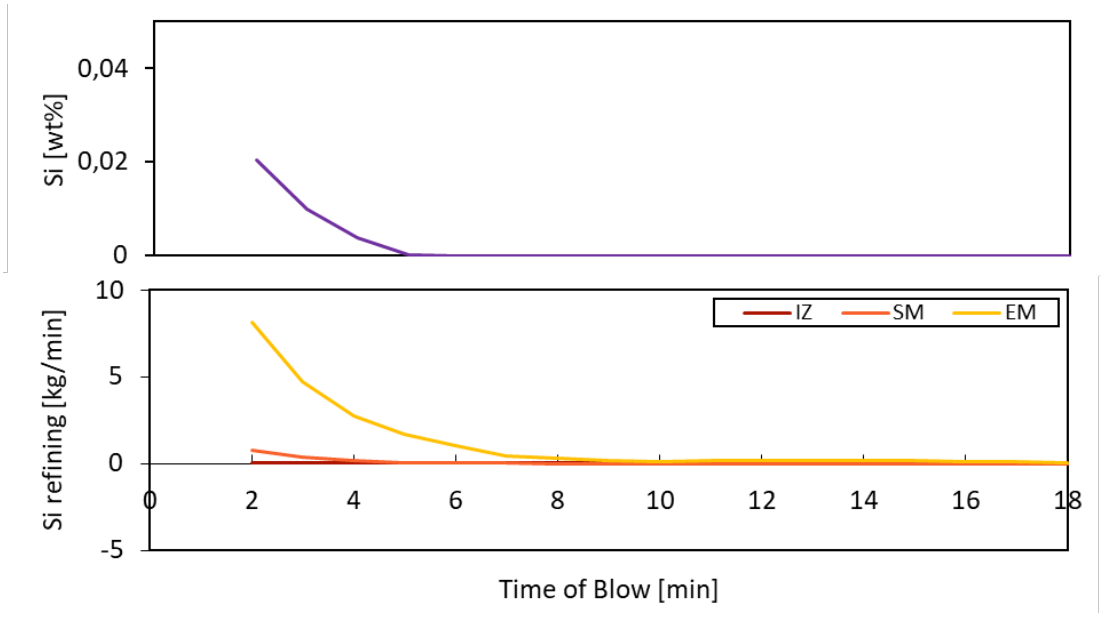

Figure 7-9 50 ton Converter: (top) Silicon content during blow, (bottom) desiliconization rate depending on the reaction interface: impact zone (IZ), slag metal zone (SM), emulsion zone (EM)

The simulation indicated a rapid refining of silicon, with a significant portion oxidized by the fourth minute. This observation is consistent with Figure 7-9 and aligns well with the trend depicted in Figure 7-4. By the fifth minute, silicon is almost fully oxidized, reaching a residual percentage in the hot metal bath close to 0wt%. Furthermore, the validation of the model

presented in this study using data from a 200-ton converter demonstrated a high level of agreement, particularly after the third minute of refining.

However, the minimal residual silicon raises questions regarding the completeness of the refining process. One potential area for improvement is the incorporation of a dynamic slag composition model to enhance prediction reliability, as it may better capture the evolving chemical environment during refining.

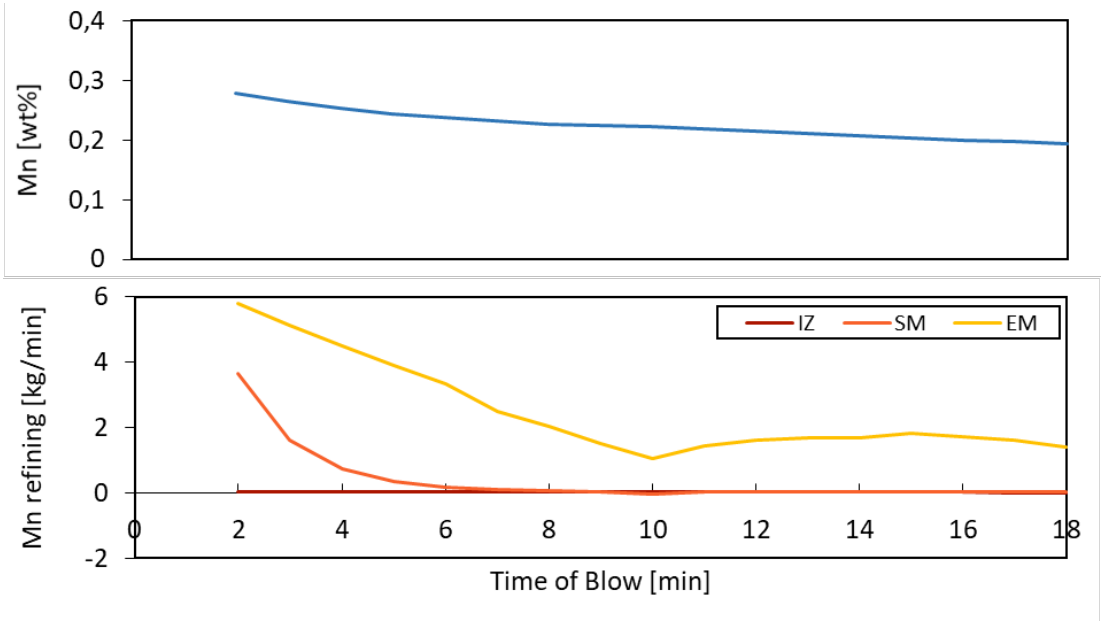

Figure 7-10 50 ton Converter: (top) Manganese content during blow, (bottom) Manganese removal rate depending on the reaction interface: impact zone (IZ), slag metal zone (SM), emulsion zone (EM)

In contrast to silicon, the simulation results for manganese refining rates in the 50-ton converter Figure 7-10 deviated notably from those observed in the 200-ton converter. This discrepancy is primarily attributed to the absence of pronounced forward and reverse reactions, suggesting that either the imposed slag composition in this simulation significantly differs from the actual slag composition or that the calculation method for droplet residence time may not be appropriate due to the change in reactor size.

Nevertheless, the endpoint manganese content appears reasonable when compared to the 200-ton converter data Figure 7-5, indicating that while the kinetics may vary, the final outcome remains consistent.

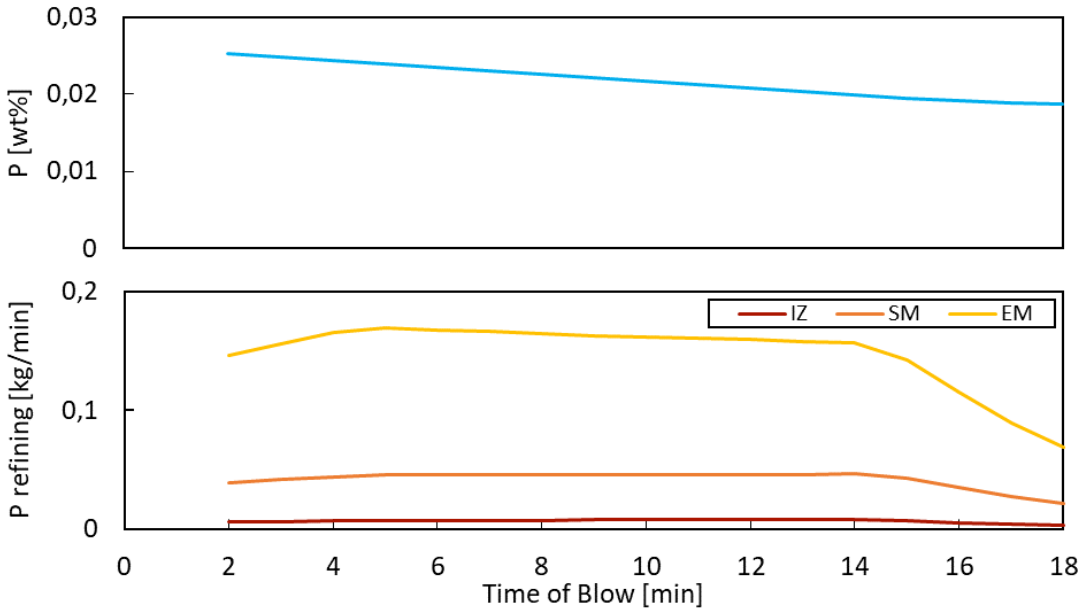

Figure 7-11 50 ton Converter: (top) Phosphorus content during blow, (bottom) dephosphorization rate depending on the reaction interface: impact zone (IZ), slag metal zone (SM), emulsion zone (EM)

For phosphorus Figure 7-11, a lower endpoint concentration of approximately 0.01wt% would be expected. However, the simulation began with only approximately one-third of the phosphorus weight percent compared to the 200-ton converter. This initial limited phosphorus to be oxidized might have influenced the refining process, due to the difference between equilibrium concentration and hot metal bath concentration being very little and thus not exerting a pronounced driving force.

Additionally, the simulation showed that refining in the slag-metal zone (SM) appeared to be more pronounced in comparison to the refining rates of the 200-ton converter Figure 7-6. This difference can be attributed to the smaller impact zone created by the 50-ton converter's reduced number of nozzles. The larger slag-metal zone had a more significant impact on the refining rate.

The relatively linear decrease in phosphorus content over time suggests that either the representation of slag composition in the simulation is not accurate or that the chosen operational parameters do not fully facilitate effective dephosphorization.

In summary, the simulation results highlight the influence of various factors on the refining rates of silicon, manganese, and phosphorus in the 50-ton converter. Notably, the larger slag-metal zone in the 50-ton converter, owing to fewer lance nozzles, contributed to the observed differences in refining rates compared to the 200-ton converter.

However, it is crucial to note that without knowledge of the specific endpoint concentrations for different constituents, the refining rates may also indicate that the operational parameters selected for this particular blow may not have been optimal. Further research and refinement of the simulation model are warranted to address these discrepancies and enhance the predictive accuracy of refining rates in smaller converters.

In conclusion, this study provides valuable insights into the refining process in a 50-ton converter and suggests avenues for future investigation and improvement.

8 CONCLUSION AND OUTLOOK

In conclusion, the mathematical model developed to depict the basic oxygen steelmaking process successfully captures a wide range of influential factors affecting the refining reactions in the converter. The model represents a significant advancement in understanding the complex interactions involved in this crucial industrial process, bringing it one step closer to reality. The validation results demonstrate that the model's calculations align remarkably well with both measured data and predictions made by other research teams.

Two key factors differentiate this model from existing ones in the literature. Firstly, a comprehensive investigation was conducted on diffusion coefficients used to describe the refining rates. By carefully selecting diffusion coefficients measured in liquid and gas phases for liquid-liquid and liquid-gas interfaces, respectively, the model's refining rate predictions significantly improved, yielding more accurate results. This adaptation was pivotal in enhancing the prediction capabilities of the model.

Secondly, the behaviour of droplets in the converter's emulsion zone was subjected to a more detailed analysis. Existing literature predominantly employs droplet size distribution models, incorporating the bloated droplet theory and the ballistic movement of droplets. However, this presented model goes further by considering the effect of loss as dust production in the off-gas. Consequently, the force balance indicates that some droplets may be blown out of the converter, challenging the conventional understanding of droplet dynamics. This novel insight expands the scope of the model and its ability to represent the complexity of the process.

The knowledge gained from this model holds promising implications for process optimization. It enables the feasibility of using raw materials of lower quality, enhances the efficient planning of flux additions based on the refining state, and facilitates the design of furnace and lance geometry tailored to specific requirements. Nonetheless, further research and improvement remain essential to explore the full potential of this model.

The most influential factors affecting the simulation outcome have been identified as diffusion coefficients, axial jet velocity, and slag evolution. Understanding and managing

these aspects will be crucial for fine-tuning the model's predictions and refining the steelmaking process.

Looking ahead, the presented model's reliance on converter geometry suggests exciting possibilities. By employing a backward calculation parameterization approach algorithm, it might be feasible not only to predict refining rates but also to forecast converter and lance geometry. This advancement could allow for the precise adaptation of apparatuses to the desired product specifications.

Moreover, the model's structure lends itself to easy integration of additional kinetic aspects. By incorporating the wear of the converter lining and lance into the model, the complexity of the system can be further expanded. Predicting wear can provide valuable insights into maintenance requirements and enhance the predictability of the process.

Of particular importance is the wear of the lance, which significantly influences blowing behaviour and, consequently, droplet ejection, affecting the largest reaction interface in the converter. Implementing a lance wear prediction capability could profoundly impact the modelling outcome and contribute to better process control and optimization.

In conclusion, the mathematical model of the basic oxygen steelmaking process presented here represents a significant advancement in the field. Its ability to capture complex interactions and provide accurate predictions of refining rates and other process parameters opens up new avenues for process optimization and customization. As ongoing research continues to refine the model and explore additional influential factors, it holds the potential to change the steelmaking industry, making it more efficient, sustainable, and adaptable to changing demands.

9 NOMENCLATURE

Abbreviation	Definition	Unit
A	Area	$[m^2]$
a	empirical parameter	$[-]$
b	empirical parameter	$[-]$
C	Concentration	$[wt\%]$
D	Diffusion coefficient	$[m^2\ /s]$
d	Diameter	$[m]$
F	Volumetric flowrate	$[Nm^3/s]$
H	Height	$[m]$
k	Mass transfer coefficient	$[kg/m^2\ s]$
L	Equilibrium distribution ratio	$[-]$
M	Molecular mass	$[kg/mol]$
N	Blowing number	$[-]$
n	Quantity	$[-]$
P	Pressure	$[Pa]$
Q	Heat transfer	$[W/m^2\ ]$
r	Radius	$[m]$
R	Universal gas constant	$[J/molK]$
$rate$	Change of concentration or mass per second	
T	Temperature	$[K]$
t	Time	$[s]$
u	Velocity	$[m/s]$
V	Volume	$[m^3]$
W	Weight	$[kg]$
Greek Symbols		
γ	Activity coefficient	$[K]$
ε	Stirring energy	$[W/t]$

θ	Nozzle angle	$[deg]$
ρ	Density	$[kg/m^3]$
λ	Thermal conductivity	$[W/mK]$
μ	Viscosity	$[sPa]$

Subscripts and Superscripts

0	Initial conditions
a	Atmospheric
ap	Apparent
B	Metal bath
cav	Individual cavity
$conv$	Conversion
d	Droplet
$eject$	Droplets ejected from the hot metal bath
em	Emulsion metal interface
eq	equilibrium
f	Gas film
g	Gas phase
gm	Gas metal interface
iz	Jet impact zone
j	Impurity: carbon, silicon, manganese, phosphorus
L	Lance
m	Metal phase
$melt$	Melting
$nozzle$	Lance nozzle
ore	Iron ore
red	Reduction
res	Residence time
$return$	Droplets returning to the hot metal bath
s	Slag phase

sm	Slag metal interface
t	Time
T	Temperature corrected
th	Lance throat
x	Axial velocity

10 List of Tables

11 List of Figures

12 Works Cited

[1] Å. Ekdahl, "Climate Change and the Production of Iron and Steel: An Industry View," Steel Association: Brussels, Belgium, 2021.

[2] International Energy Agency, "Iron and Steel Technology Roadmap," IEA: Paris, France, 2020.

[3] L. Price, J. Sinton, E. Worrell, D. Phylipsen, H. Xiulian and L. Ji, "Energy use and carbon dioxide emissions from steel production in China," *Energy,* vol. 27, no. 5, pp. 429-446, 2002.

[4] "Eurofer," Januar 2023. [Online]. Available: https://www.eurofer.eu/about-steel/learn-about-steel/what-is-steel-and-how-is-steel-made/.

[5] H. Jalkanen and L. Holappa, "Chapter 1.4 - Converter Steelmaking," in *Treatise on Process Metallurgy, Volume 3*, Elsevier, 2014, pp. 223-270.

[6] T. Miller, J. Jimenez, A. Sharan and D. Goldstein, "Chapter 9 Oxygen Steelmaking Processes," in *In The Making, Shaping, and Treating of Steel, 11th ed.*, Pittsburgh, PA, The AISE Steel Foundation, 1998, pp. 475 - 524.

[7] H. E. McGannon, The Making, Shaping and Treating of Steel: Ninth Edition, Pittsburgh, Pennsylvania: United States Steel Corporation, 1971.

[8] "Chemie-Schule," 2013. [Online]. Available: https://www.chemie-schule.de/KnowHow/Eisen-Kohlenstoff-Diagramm#google_vignette.

[9] K. J. Barker, J. R. Paules and N. Rymarchyk, "Oxygen Steelmaking Furnace Mechanical Description and Maintenance Considerations," *Material Science,* 1998.

[10] H. Odenthal, J. Kempken, J. Schlüter and W. Emling, "Advantageous numerical simulation of the converter blowing process," *Iron Steel Technol.,* no. 4, pp. 71-89, 2007.

[11] "ispatguru," 2023. [Online]. Available: https://www.ispatguru.com/oxygen-blowing-lance-and-lance-tips-in-converter-steel-making/.

[12] "ispatguru," 2023. [Online]. Available: https://www.ispatguru.com/combined-blowing-process-in-converter-steel-making/.

[13] L. De Vos, I. Bellemans and C. Vercruyssen, "Basic Oxygen Furnace: Assessment of Recent Physiochemical Models," *Metall Mater Trans B,* vol. 50, pp. 2647-2666, 2019.

[14] C. Chigwedu, J. Kempken and W. Pluschkell, "Stahl Eisen," vol. 126, pp. 25-31, 2006.

[15] B. Deo and A. Shukla, "5th International Congress on the Science and Technology of Steelmaking," Dresden, Germany, 2012.

[16] N. Dogan, G. A. Brooks and M. A. Rhamdhani, "Comprehensive Model of Oxygen Steelmaking Part 1: Model Development and Validation," *ISIJ International,* vol. 51, no. 7, pp. 1086-1092, 2011.

[17] N. Dogan, G. A. Brooks and M. A. Rhamdhani, "Comprehensive Model of Oxygen Steelmaking Part 2: Application of Bloated Droplet Theory for Decarburization in Emulsion Zone," *ISIJ International,* vol. 51, no. 7, pp. 1093-1101, 2011.

[18] N. Dogan, G. A. Brooks and M. A. Rhamdhani, "Kinetics of Flux Dissolution in Oxygen Steelmaking," *ISIJ International,* vol. 49, no. 10, pp. 1474-1482, 2009.

[19] N. Dogan, G. A. Brooks and M. A. Rhamdhani, "Comprehensive Model of Oxygen Steelmaking Part 3: Decarburization in Impact Zone," *ISIJ International,* vol. 51, no. 7, pp. 1102-11, 2011.

[20] B. Rout, G. Brooks, M. Rhamdhani and e. al., "Dynamic Model of Basic Oxygen Steelmaking Process Based on Multi-zone Reaction Kinetics: Model Derivation and Validation.," *Metall Mater Trans B,* vol. 49, p. 537–557, 2018.

[21] D. Dering, C. Swartz and N. Dogan, "Dynamic Modeling and Simulation of Basic Oxygen Furnace (BOF) Operation," *Processes,* vol. 8, no. 4, p. 483, 2020.

[22] E. Turkdogan, Fundamentals of Steelmaking, London: The Institute of Materials, 1996.

[23] N. Dogan, Mathematical Modelling of Oxygen Steelmaking. Doctoral Thesis, 2011.

[24] P. Kubicek and T. Peprica, "Diffusion in molten metals and melts: application to diffusion in molten iron," International Metals Review, 1983.

[25] D. Goldberg and G. Belton, "The Diffusion of Carbon in Iron-Carbon Alloys at 1560°C," *Metallurgical Transactions,* vol. 5, pp. 1643-8, 1974.

[26] Y. Kawai and K. Mori, " Equilibrium and Kinetics of Slag-Metal Reactions," *Transactions ISIJ,* vol. 13, pp. 303-17, 1973.

[27] R. Grace, "Diffusion of third elements in liquid iron saturated with carbon," *Transactions of the Metallurgical Society of AIME,* no. 212, pp. 331-7 , 1958.

[28] F. Calderon, N. Sano and Y. Matsushita, "Diffusion of Manganese and Silicon in Liquid Iron over the Whole Range of Composition," *Metallurgical Transactions,* vol. 2, pp. 3325-32, 1971.

[29] A. Shukla, B. Deo and D. Robertson, "Scrap Dissolution in Molten Iron Containing Carbon for the Case of Coupled Heat and Mass Transfer Control.," *Metall Mater Trans B 44,* p. 1407–1427, 2014.

[30] H. Suito and R. Inoue, in *Trans. Iron Steel Inst. Jpn. 24, 257*, 1984.

[31] S. C. Koria and K. W. Lange, "Penetrability of impinging gas jets in molten steel bath," *Process metallurgy ,* vol. 58, no. 9, pp. 421-426, 1987.

[32] I. Sawada, T. Ohashi and H. Kajioka, *Tetsu-to-Hagane,* vol. 70, pp. 160-161, 1984.

[33] S.-y. Kitamura, T. Kitamura, K. Shibata, Y. Mizukami, S. Mukawa and J. Nakagawa, "Effect of Stirring Energy, Temperature and Flux Composition on Hot Metal Dephosphorization Kinetica," *ISIJ International,* vol. 31, no. 11, pp. 1322-1328, 1991.

[34] Y. Ogasawara, Y. Miki, Y. Uchida and N. Kikuchi, "Development of High Efficiency Dephosphorization System in Decarburization Converter Utilizing FetO Dynamic Control," *ISIJ Int.,* vol. 53, p. 1786–93, 2013.

[35] W. Van der Knoop, B. Deo, A. Snoeijer, G. Van Unen and R. Boom, "A dynamic slag-droplet model for the steelmaking process," *ISIJ,* pp. 302-307, 1992.

[36] B. Rout, G. Brooks, Subagyo and e. al., "Modeling of Droplet Generation in a Top Blowing Steelmaking Process.," *Metall Mater Trans B,* vol. 47, p. 3350–3361, 2016.

[37] K. Chou, U. Pal and R. Reddy, "A General Model for BOP Decarburization," vol. 33, pp. 862-68, 1993.

[38] B. Rout, G. Brooks, M. Akbar Rhamdhani and e. al., "Dynamic Model of Basic Oxygen Steelmaking Process Based on Multizone Reaction Kinetics: Modeling of Manganese Removal.," *Metall Mater Trans B,* vol. 49, p. 2191–2208, 2018.

[39] A. Kadrolkar and N. Dogan, "The Decarburization Kinetics of Metal Droplets in Emulsion Zone," *Metall Mater Trans B,* vol. 50, p. 2912–2929, 2019.

[40] G. Brooks, Y. Pan, Subagyo and K. Coley, "Modeling of Trajectory and Residence Time of Metal Droplets in Slag-Metal-Gas Emulsion in Oxygen Steelmaking," *Metallurgical and Materials Transactions B,* vol. 36B, pp. 525-535, 2005.

[41] G. Brooks, Y. Subagyo and K. Coley, "Modeling of Trajectory and Residence Time of Metal Droplets in Slag-Metal-Gas Emulsions in Oxygen Steelmaking," Metallurgical and Materials Transactions B.

[42] N. Standish and Q. He, "A model study of residence time of metal droplets in the slag in basic oxygen furnace steelmaking," *ISIJ Int.,* vol. 29, no. 6, pp. 455-61, 1989.

[43] B. Deo and A. Shukla, in *5th International Congress on the Science and Technology of Steelmaking*, Dresden, germany, 2012.

[44] A. Subagyo, G. Brooks and K. Coley, "Residence time of metal droplets in slag-metal-gas emulsions through top gas blowing," *Can. Metall. Q.,* vol. 44, no. 1, pp. 199-30, 2005.

[45] I. Sumi, Y. Kishimoto, Y. Kikuchi and H. Igarashi, "Effect of high-temperature field on supersonic oxygen jet behavior," *ISIJ Int.,* vol. 46, no. 9, pp. 1312-17, 2006.

[46] C. Cicutti, M. Valdez, T. Pérez, J. Petroni, A. Gómez, R. Donayo and L. Ferro, in *Sixth International Conference on Molten Slags, Fluxes and Salts*, Stockholm-Helsinki: Warrandale, PA, 2000.

[47] I. Sumi, Y. Kishimoto, Y. Kikuchi and H. Igarashi, "Effect of high-temperature field on supersonic oxygen jet behavior," *ISIJ Int.,* vol. 46, no. 9, p. 1312–17, 2006.

[48] B. Rout, G. Brooks, Z. Li and M. A. Rhamdhani, "Analysis of Desiliconization Reaction Kinetics in a BOF," in *AISTech*, 2016.

[49] H. Suito and R. Inoue, "Thermodynamic Assessment of Manganese Distribution in Hot Metal and Steel," *ISIJ International,* vol. 35, no. 3, pp. 266-271, 1995.

[50] R. Nagabayashi, M. Hino and S. Ban-Ya, "Mathematical Expression of Phosphorus Distribution in Steelmaking Process by Quadratic Formalism," *ISIJ International,* vol. 29, no. 2, pp. 140-147, 1989.

[51] A. Shukla, Dissolution of Steel Scrap in Molten Metal During Steelmaking. Ph.D. Dissertation, Indian Institute of Technology, Kanpur, India, 2011.

[52] J. Bekker, I. Craig and P. Pistorius, "Modeling and Simulation of an Electric Arc Furnace Process," *ISIJ International,* vol. 39, no. 1, pp. 23-32, 1999.

[53] H. Jalkanen, "Experiences in physiochemical medelling of oxygen converter process (BOF)," in *Materials Science*, 2006.

[54] B. K. Rout, G. Brooks, M. A. Rhamdhani, Z. Li, F. N. Schrama and A. Overbosch, "Dynamic Model of Basic Oxygen Steelmaking Process Based on Multizone Reaction Kinetics: Modeling of Decarburization," *Metallurgical and Materials Transactions B,* vol. 49B, pp. 1022-1033, 2018.

[55] Y. Lytvynyuk, J. Schenk, M. Hiebler and A. Sormann, "Thermodynamic and Kinetic Model of the Converter Steelmaking Process. Part 1: The Description of the BOF Model," *steel research,* vol. 85, no. 4, pp. 537-543, 2014.

[56] R. Sarkar, P. Gupta and S. Basu, "Dynamic Modeling of LD Converter Steelmaking: Reaction Modeling Using Gibbs' Free Energy Minimization.," *Metall Mater Trans B,* vol. 46, p. 961–976, 2015.

[57] A. Kruskopf, Multiphysical Modeling Approach for Basic Oxygen Steelmaking Process Doctoral Dissertation, School of Chemical Engineering, 2018.

[58] C. Kattenbelt and B. Roffel, "Dynamic Modeling of the Main Blow in Basic Oxygen Steelmaking Using Measured Step Responses," *Metall Mater Trans B,* vol. 39, p. 764–769, 2008.

[59] G.-h. Li, B. Wang, Q. Liu, X.-z. Tian, R. Zhu, L.-n. Hu and G.-g. Cheng, "A process model for BOF process based on bath mixing degree," *International Journal of Minerals, Metallurgy and Materials,* vol. 17, no. 6, pp. 715-22, 2010.

[60] S. Chen and Z. Cai, "An Improved Dynamic Model of the Vanadium Extraction Process in Steelmaking Converters," *Applied Sciences,* vol. 10, no. 1, p. 111, 2020.

[61] J. Ruuska, A. Sorsa, J. Lilja and K. Leiviskä, "Mass-balance Based Multivariate Modelling of Basic Oxygen Furnace Used in Steel Industry," *IFAC PapersOnLine,* vol. 50, no. 1, p. 13784–13789, 2017.

[62] M. Schlautmann, B. Kleimt, S. Khadhraoui, K. Hack, P. Monheim, B. Glaser, R. Antonic, M. Adderley and F. Schrama, "3rd European Steel Technology and Application Days (ESTAD)," Vienna, Austria, 2017.

[63] V. Visuri, M. Järvinen and A. Kärnä, "A Mathematical Model for Reactions During Top-Blowing in the AOD Process: Derivation of the Model.," *Metall Mater Trans B,* vol. 48, p. 1850–1867, 2017.

[64] F. Pahlevani, S. Kitamura, H. Shibata and N. Maruoka, "Simulation of Steel Refining Process in Converter," *Steel Research Int.,* vol. 81, no. 8, pp. 617-22, 2010.

[65] S. Ohguchi, D. G. C. Robertson, B. Deo, P. Grieveson and J. H. E. Jeffes, "Simultaneous Dephosphorization And Desulphurization Of Molten Pig Iron," *Ironmaking and Steelmaking,* vol. 11, no. 4, pp. 202-213, 1984.

[66] K. A and D. N., "Model Development for Refining Rates in Oxygen Steelmaking: Impact and Slag-Metal Bulk Zones.," *Metals,* vol. 9, no. 3, p. 309, 2019.

[67] S. Khadhraoui, H.-J. Odenthal, S. Das, M. Schlautmann, K. Hack, B. Glaser and R. Woolf, "A new approach for modelling and control of dephosphorization in BOF converter," *La Metallurgia Italiana,* vol. 11, no. 12, pp. 5-16, 2018.

[68] D. Mombelli, C. Mapelli, S. Barella, A. Gruttadauria, R. Sosio, G. Valentino and V. Ancona, "Model for Phosphorus Removal in LD Converter and Design of a Valuable Operative Practice," vol. 89, no. 5, 2018.

[69] B. Deo, P. Ranjan and A. Kumar, "Mathematical model for computer simulation and control of steelmaking," *steel research,* vol. 58, no. 9, pp. 427-431, 1987.

[70] P. Cavaliere, "Chapter 5 Basic Oxygen Furnace: Most Efficient Technologies for Greenhouse Emissions Abatement," in *Clean Ironmaking and Steelmaking Processes Efficient Technologies for Greenhouse Emissions Abatement*, Lecce, Italy.

[71] M. Schlautmann, B. Kleimt, S. Khadhraoui, K. Hack, P. Monheim, B. Glaser, R. Antonic, M. Adderley and F. Schrama, "Dynamic on-line monitoring and end point control of dephosphorisation in the BOF converter," in *3rd European Steel Technology and Application Days (ESTAD)*, Vienna, 2017.

[72] D. Pasternak and A. Olander, "Diffusion in Liquid Metals," *AIChe Journal,* vol. 13, no. 6, pp. 1052-7, 1967.

[73] Y. Doh, P. Chapelle and A. Jardy, "Toward a Full Simulation of the Basic Oxygen Furnace: Deformation of the Bath Free Surface and Coupled Transfer Processes Associated with the Post-Combustion in the Gas Region.," *Metall Mater Trans B,* vol. 44, p. 653–670, 2013.

[74] A. Kadrolkar, N. Andersson and N. Dogan, "Dynamic Flux Dissolution Model for Oxygen Steelmaking," *Metall Mater Trans B,* vol. 48, p. 99–112, 2017.

[75] M. Jung and A. Van Ende, in *Proceedings Asia Steel International Conference 2015*, The Iron and Steel Institute of Japan, Yokohama, 2015.

[76] L. Holappa and P. Kostamo, "Development of Blowing Practice in the Koverhar LD Plant," Scand. J. Metall., 1974.

A. Appendix

A.1 Model summary

Reference	**Dogan** [19]	**Rout** [54]	**Lytvynyuk** [55]
Type **Number of Reaction Zones**	reaction interface model 2 (+ subsystems)	reaction interface model 3 (no subsystems)	reaction interface model 1
Integration of Thermodynamics	-	Partition ratio From literature	Equilibrium constants + coupled reaction model
Integration of Kinetics	Macro and micro kinetics	Macro and micro kinetics	Macro kinetics
Temperature	Imposed linear profile $T_{slag} > T_{steel}$	Imposed linear profile $T_{slag} > T_{steel}$	Heat balance
Impurities	C	C, Mn, P, Si	C, Mn, P, Si, Ti, V
Reference	**Sarkar** [56]	**Kruskopf** [57]	**Van Ende**
Type **Number of Reaction Zones**	reaction interface model 3	reaction volume model 1	reaction volume model 10
Integration of Thermodynamics	Gibbs free energy Minimization	Gibbs free energy Minimization	Gibbs free energy Minimization
Integration of Kinetics	Macro and micro kinetics	Size reaction volume	Sizes reaction volume
Temperature	Imposed linear profile $T_{slag} = T_{steel}$	Heat balance	Heat balance
Impurities	C, Mn, Si	C, Si	C, Mn, P, Si
Reference	**Jalkanen** [5]	**Kettenbelt** [58]	**Deo and Shukla** [42]
Type **Number of Reaction Zones**	- 1 (+ submodels)	Statistical -	- -
Integration of Thermodynamics	-	-	Gibbs free energy Factsage database
Integration of Kinetics	-	-	-
Temperature	- $T_{slag} = T_{steel}$ (mean T)	- T_{bath}	-
Impurities	Si, Ti, V, Mn, P	C	-
Blown Oxygen Rate	Low fit rate Simulated values are larger No explanation	Input measurement	-
Lance Height	Taken into account	Taken into account (empirical)	-

Reference	**Li** [59]	**Chen** [60]	**Dering** [21]
Type **Number of Reaction Zones**	- -	- 3 Systems	- -
Integration of Thermodynamics	-	Gibbs free energy	-
Integration of Kinetics	-	-	-
Temperature	T_{bath} (can be predicted)	- -	-
Impurities	Si, Mn	C, Mn, P, Si, Ti, **V**	-
Blown Oxygen Rate	invariable	Input	-
Lance Height	yes	Input	-
Reference	**Ruuska** [61]	**Schlautmann // Khadhraoui** [62]	**Ville-Valtteri Visuri** [63]
Type **Number of Reaction Zones**	Statistical No Zones only submodels	Interlinked local equilibria 3 + nonreactive slag part	
Integration of Thermodynamics	-	-	equilibrium
Integration of Kinetics	-	-	-
Temperature	-	-	-
Impurities	-	-	C, Mn, Si
FeO Concentration Peak	-	-	-
Blown Oxygen Rate	-	-	-
Lance Height	-	-	Impact zone geometry
Reference	**Pahlevani** [64]	**Chigwedu** [14]	**Ohguchi** [65]
Type **Number of Reaction Zones**	Coupled reaction model -	- 1	Coupled reaction model -
Integration of Thermodynamics	-	-	-
Integration of Kinetics	-	-	-
Temperature	-	-	-
Impurities	-	-	-
FeO Concentration Peak	-	-	-
Blown Oxygen Rate	-	-	-
Lance Height	-	-	-

A.2 REACTIONS MODELLED

The reactions modelled are summarized in the following table. Only well investigated, documented and validated reaction systems have been chosen.

Addition:

Iron Ore

$$Fe_2O_3 \rightarrow 2Fe + 1.5\ O_2 \quad \text{Eq. 77}$$

$$FeO \rightarrow Fe + 0.5\ O_2 \quad \text{Eq. 78}$$

Impact Zone:

$$[Si] + O_2(g) \rightarrow (SiO_2) \quad \text{Eq. 81}$$

$$[Fe] + \frac{1}{2}O_2(g) \rightarrow (FeO) \quad \text{Eq. 83}$$

$$[Mn] + \frac{1}{2}O_2(g) \rightarrow (MnO) \quad \text{Eq. 85}$$

$$CO + \frac{1}{2}O_2(g) \rightarrow CO_2(g) \quad \text{Eq. 87}$$

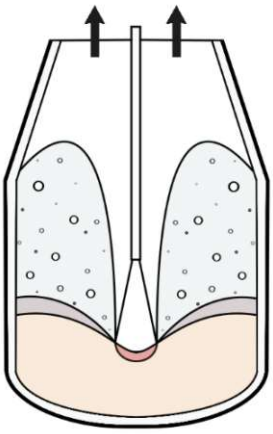

Oxidation of CO gas

$$[C] + \frac{1}{2}O_2(g) \rightarrow CO(g) \quad \text{Eq. 79}$$

$$[C] + CO_2(g) \rightarrow 2CO(g) \quad \text{Eq. 80}$$

Droplet and slag bulk metal:

$$(FeO) + [C] \rightarrow [Fe] + CO(g) \quad \text{Eq. 82}$$

$$Si + 2\ FeO \rightarrow SiO_2 + 2Fe \quad \text{Eq. 84}$$

$$Mn + FeO \rightleftharpoons CO + Fe \quad \text{Eq. 86}$$

$$2\ P + 5\ FeO + 4\ CaO \rightleftharpoons 4\ CaO.P_2O_5 + 5\ Fe \quad \text{Eq. 88}$$

Slag Zone:

$$Si + 2FeO \rightarrow SiO_2 + 2Fe \quad \text{Eq. 89}$$

$$Mn + FeO \rightarrow MnO + Fe \quad \text{Eq. 90}$$

$$2P + 5FeO \rightarrow P_2O_5 + 5Fe \quad \text{Eq. 91}$$

A.3 JET PENETRABILITY CALCULATION [30]

Parameters for a specific calculation scenario			
L_h	1.6	$[m]$	… Lance height
n_n	6	$[-]$	… Number of nozzles
d_{th}	0.032	$[m]$	… Diameter of throat diameter
P_a	1.01325	$[bar]$	… Atmospheric pressure
P_o	10.13	$[bar]$	… Oxygen supply pressure
$nangle$	10	$[°]$	… Inclination angle of a nozzle
ρ_m	6680	$[kg/m^3]$	… Density of liquid hot metal
g	9.81	$[m/s^2]$	… Gravitational acceleration
$\dot{m}_n$		[-]	… Momentum flow rate of each nozzle
$\dot{m}_t$		[-]	… Total momentum flow rate
$\dot{M}_d$		[-]	… Momentum flow rate
$\dot{M}_h$		[-]	… Momentum flow rate

Equation	Result	
$\dot{m}_t = 0.7854 \times 10^5 \times n_n \times d_{th}^2 \times P_a \left(\frac{1.27 P_0}{P_a} - 1\right)$	$\dot{m}_t = 2819.71920$	Eq. 92
$\dot{m}_n = \frac{\dot{m}_t}{n_n}$	$\dot{m}_n = 939.90640$	Eq. 93
$\dot{M}_d = \frac{\dot{m}_t \left(1 + \sin(nangle)\right)}{\rho_m g L_h^3}$	$\dot{M}_d$ = 0.0047901	Eq. 94
$\dot{M}_h = \frac{\dot{m}_n \cos(nangle)}{\rho_m g L_h^3}$	$\dot{M}_h = 3.4485 \cdot 10^{-3}$	Eq. 95
$h = 4.469 \dot{M}_h^{0.66} L_h$	$h = 0.16949\ m$	Eq. 96
$r_{cav} = 0.5 \times 2.813 L_h \dot{M}_d^{0.282}$	$r_{cav} = 1.30296\ m$	Eq. 97
$A_{cav} = \frac{\pi r_{cav}^4}{6h^2}\left[\left(1 + \frac{4h^2}{r_{cav}^2}\right)^{3/2} - 1\right]$	$A_{cav} = 5.42275\ m^3$	Eq. 98
$A_{iz} = n_n A_{cav}$	$A_{iz} = 16.26826\ m^3$	Eq. 99

A.4 BATH STIRRING ENERGY

Parameters for an exemplary scenario			
D	5.8	$[m]$	… Diameter of furnace
n_n	6	$[-]$	… Number of nozzles
H	1.56	$[m]$	… Hot metal bath height
L	1.5	$[m]$	… Lance height
d	0.0506	$[m]$	… Diameter of nozzle
W	210	$[ton]$	… Weight of metal bath
θ	23	$[°]$	… Inclination angle of a nozzle
T	1623	$[K]$	… Temperature of impact zone
R	8.3145	$[J/molK]$	… Gas constant
k_m^{gm}		*[cm/s]*	… Mass transfer coefficients
E_{st}		*[W/t]*	… Stirring energy
Q_1		*[Nm³/min]*	… Gas flow rate
V_1		*[m/s]*	… Gas velocity at the nozzle exit
Q_1		*[m³/s]*	… Volumetric flow rate

Equation	Result	
$\log(k_m^{gm}) = 1.98 + 0.5\log\left(\frac{\varepsilon H^2}{100D}\right) - \frac{125000}{2.3RT}$	$k_m^{gm} = 0.58604\ \frac{cm}{s}$	Eq. 100
$E_{st} = \frac{0.0453 Q_1 V_1^2 d \cos^2(\theta)}{WL}$	$E_{st} = 3099{,}751\ \frac{Watt}{ton}$	Eq. 101
$V_1 = \frac{Q_1}{60A_1} = \frac{Q_1}{60\frac{\pi}{4}d^2}$	$V_1 = 897.60\ \frac{m}{s}$	Eq. 102
$Q_1 = \frac{650}{n_n}\ \frac{m^3}{min}$	$Q_1 = 108.3\ \frac{m^3}{min}$	Eq. 103

A.5 Iron Ore Dissolution Calculation Algorithm

1. $\frac{4}{3}\pi r_{ore}^3 \rho_{ore} C_{P,ore} \frac{dT_{ore}}{dt} = \left(1 - \frac{T_{ore}}{T_m}\right) 4\pi r_{ore}^2 h_{ore} (T_s - T_{ore})$
2. $\frac{dT_{ore}}{dt} = \left(1 - \frac{T_{ore}}{T_m}\right) (T_s - T_{ore}) \frac{3h_{ore}}{r_{ore}\rho_{ore}C_{P,ore}}$
3. Initial values as in table: the temperature of the iron ore particles can be calculated

   $$\frac{dT_{ore}}{dt} = \left(1 - \frac{303K}{T_m}\right) (T_s - 303K) \frac{3 \cdot 2500 \frac{W}{m^2 K}}{0.03m \cdot 2.88 \frac{kg}{m^3} \cdot 200.83 \frac{J}{molK}}$$

4. To calculate the change of the particle radius

   $$A_{ore}\rho_{ore}\left(\Delta H_{ore} + C_{PFeO}(T_s - T_{ore})\right)\frac{dr_{ore}}{dt} = -\left(\frac{T_{ore}}{T_m}\right) Q_{conv,ore}$$

   $$\rho_{ore}\left(\Delta H_{ore} + C_{PFeO}(T_s - T_{ore})\right)\frac{dr_{ore}}{dt} = -\left(\frac{T_{ore}}{T_m}\right) h_{ore}(T_s - T_{ore})$$

   $$\frac{dr_{ore}}{dt} = -\left(\frac{T_{ore}}{T_m}\right) h_{ore}(T_s - T_{ore}) \frac{1}{\rho_{ore}\left(\Delta H_{ore} + C_{PFeO}(T_s - T_{ore})\right)}$$

5. *Initial values*

   $$\frac{dr_{ore}}{dt} = -\left(\frac{303K}{T_m}\right) 2500 \frac{W}{m^2 K} (T_s - 303K) \frac{1}{2.88 \frac{kg}{m^3}\left(184.66 \frac{kJ}{mol} + 200.83 \frac{J}{molK}(T_s - 303K)\right)}$$

6. *With the change of particle radius the melting rate can be calculated*

   $$\dot{W}_{ore,melt} = -4\pi\rho_{ore} r_{ore}^2 \frac{dr_{ore}}{dt}$$

7. $Q_{red,ore} = \frac{y_{Fe,ore}}{3M_{Fe}} \dot{W}_{ore,melt} \Delta H_{ore}$

A.6 FLUX DISSOLUTION CALCULATION ALGORITHM

Lime dissolution rate:

1. If: $r_{Lime} > 0$

   particle settling velocity: $u_{CaO} = u_{Lime} = \left[\frac{(\rho_{slag}-\rho_{lime})g}{9\sqrt{\mu_{slag}\rho_{slag}}}\right]^{2/3} d_{particle}$

   $$\left[\frac{\left(\frac{kg}{m^3}-\frac{kg}{m^3}\right)\frac{m}{s^2}}{\sqrt{\frac{kg\,kg}{msm^3}}}\right]^{\frac{2}{3}} m = \left[\frac{\left(\frac{kg}{m^2s^2}\right)}{\sqrt{\frac{kg\,kg}{msm^3}}}\right]^{\frac{2}{3}} m = \left[\frac{\left(\frac{kg}{m^2s^2}\right)}{\frac{kg}{m^2s^{1/2}}}\right]^{\frac{2}{3}} m = \left[\frac{m^2s^{1/2}kg}{m^2s^2kg}\right]^{\frac{2}{3}} m = \left[s^{-\frac{3}{2}}\right]^{\frac{2}{3}} m = \frac{m}{s}$$

   $$Re_{CaO} = u_{CaO} 2r_{Lime} \frac{\rho_{slag}}{\mu_{slag}}$$

   $$Sh_{CaO} = 1 + 0.724 \cdot nes^{0.48} \cdot Re_{CaO}^{0.48} Sc_{CaO}^{1/3}$$

   $$k_{Lime} = \frac{Sh_{CaO} D_{CaO}}{2r_{Lime}}$$

2. With

   $$D_{CaO} = A_{CaO} \frac{T_{slag}}{\mu_{slag}}$$

3. Also for a $r_{Lime} < 0$ all the under 1 stated eq. have to be set zero

4. Number of particles

   $$n_{Lime} = u_{Lime}$$

Dolomite dissolution rate:

1. If: $r_{dolomite} > 0$

   particle settling velocity: $u_{MgO} = u_{Dolomite} = \left[\frac{(\rho_{slag}-\rho_{lime})g}{9\sqrt{\mu_{slag}\rho_{slag}}}\right]^{2/3} d_{particle}$

   $$Re_{MgO} = u_{MgO} 2r_{Dolomite} \frac{\rho_{slag}}{\mu_{slag}}$$

   $$Sh_{MgO} = 1 + 0.724 \cdot nes^{0.48} \cdot Re_{MgO}^{0.48} Sc_{MgO}^{1/3}$$

   $$k_{Dolomitee} = \frac{Sh_{MgO} D_{MgO}}{2r_{Dolomitee}}$$

2. With

   $$D_{MgO} = A_{MgO} \frac{T_{slag}}{\mu_{slag}}$$

3. Also for a $r_{dolomite} < 0$ all the under 1 stated eq. have to be set zero

A.7 POSTER

Dynamic Modeling of Basic Oxygen Steelmaking

Arleen Walk *[1], Johannes Niel[1], Bernd Weiß[2], Walter Wukovits[1]

[1]Institute of Chemical, Environmental and Bioscience Engineering, TU Wien, Austria *Author Contact arleen.walk@tuwien.ac.at

[2]Primetals Technologies Austria GmbH, Linz, Austria

Introduction

- Basic oxygen steelmaking (BOS) generates approximately 70% of the worldwide produced crude steel
- The main target of this process is to decrease impurities in liquid metal by oxidizing them
- The current work proposes a dynamic model in gPROMS ModelBuilder® to deepen the understanding of the process by offering insight into the reactions taking place

Figure 1: Basic oxygen furnace [2]

Model Features

- Multizone kinetic theory approach
- Variation of lance height
- Top and bottom blow
- Flux additions and scrap melting
- Varying vessel and nozzle geometry
- Compatible with gPROMS based model library for balancing iron and steel production

Basic Oxygen Steelmaking Process

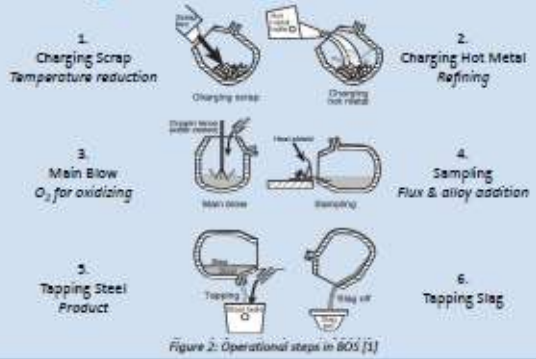

Figure 2: Operational steps in BOS [1]

Basic Oxygen Steelmaking Model

The model is developed in gPROMS ModelBuilder® and is mainly based on the work of Kadrolkar and Dogan [3] as well as Rout et al. [4]. It consists of three main zones as shown in Figure 3, the (i) Impact Zone, (ii) Slag-Bulk Zone and (iii) Emulsion Zone.

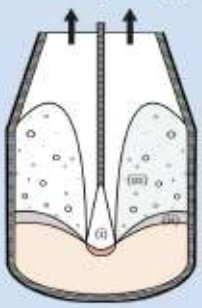

Figure 3: BOS reaction interfaces

(i) Impact Zone $\leq 0{,}3C_{wt\%}$

$$\left.\frac{d(W_m C_{jm})}{dt}\right|_{iz} = -A_{iz} k_m^{gm} \rho_m \left(C_{jm} - C_{jm}^{gm}\right) \quad \text{Eq. 1}$$

(i) Impact Zone $> 0{,}3C_{wt\%}$

$$\left.\frac{d(W_C)}{dt}\right|_{iz} = \left(\frac{dW_C}{dt}\right)_{iz}^{CO_2} + \left(\frac{dW_C}{dt}\right)_{iz}^{O_2} \quad \text{Eq. 2}$$

(ii) Slag-Bulk Zone

$$\left.\frac{d(W_m C_{jm})}{dt}\right|_{sm} = -A_{sm} k_m^{sm} \rho_m \left(C_{jm} - C_{jm}^{sm}\right) \quad \text{Eq. 3}$$

(iii) Emulsion Zone

$$\left.\frac{d(W_m C_{jm})}{dt}\right|_{em} = -\frac{W_{jm}^{ejects} - W_{jm}^{returns}}{\Delta t} \quad \text{Eq. 4}$$

Scrap Melting Rate Eq. 6

$$\frac{dW_{sc}}{dt} = \frac{-M_{Fe} k_{conv} k_{area} W_{sc} (T_b - T_{sc}) \left(\frac{T_{sc}}{T_b}\right)}{(\lambda_{Fe} + C_{p,Fe(s)})(T_b - T_{sc})}$$

Iron Ore Dissolution Eq. 7

$$W_{ore,melt} = -4\pi \rho_{ore} r_{ore}^2 \frac{dr_{ore}}{dt}$$

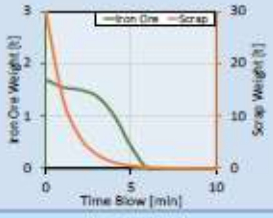

Results and Discussion

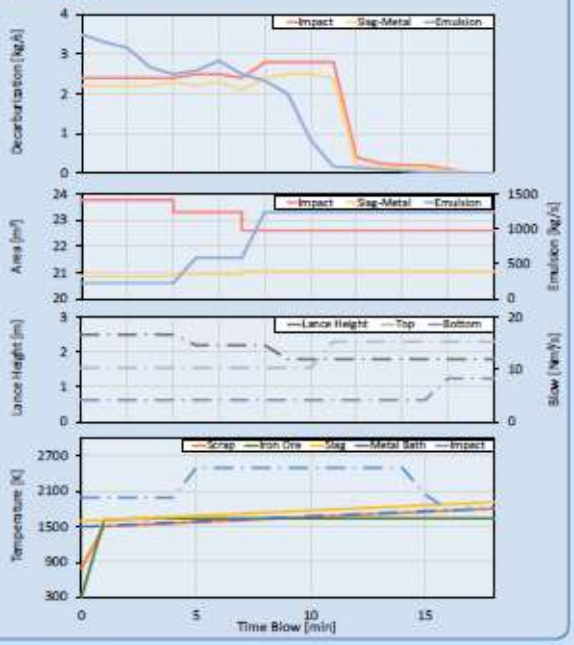

Summary

- Implementation of three reaction interfaces and the influence of blowing time and lance height on reaction development and mass transfer coefficients
- Detailed consideration of the effect of scrap, flux, and alloy additions on mass and heat transfer between reaction zones

Outlook

Insight into the evolution of the different refining reactions and their development with respect to time and addition of additives can have a great impact on the control of the process. The presented converter model has the potential to offer the level of understanding and parameter balancing to fine tune the gains in performance.

Acknowledgement

The authors gratefully acknowledge the funding of work by the research program COMET (Competence Center for Excellent Technologies), the Austrian program for competence centers (FFG contract number 869295).

References

[1] T. W. Miller, "Chapter 9 Oxygen Steelmaking Processes" (1999). [2] https://www.primetals.com/de/presse-medien/news/primetals-technologies-to-replace-bof-converter-at-hbis-oerbia-in-xmedierevo (18.3.2020, 14:43) [3] A. Kadrolkar, N. Dogan: Metals 2019, 9, 309, doi:10.3390/met9030309 [4] B.K. Rout, G. Brooks, M. Akbar Rhamdhani, Z. Li, F.N.H. Schrama, I. Sun: Metall. Mater. Trans. B, https://doi.org/10.1007/s11663-017-1166-7

2021 FemChem Scientific Workshop – 20th September 2021, TU Wien

A.8 POSTER

A Dynamic Multi-Zone gPROMS Model of Basic Oxygen Steelmaking Based on Reaction Kinetics

Arleen Walk *[1], Johannes Niel[1], Bernd Weiß[2], Walter Wukovits[1]

[1]Institute of Chemical, Environmental and Bioscience Engineering, TU Wien, Austria *Author Contact arleen.walk@tuwien.ac.at
[2]Primetals Technologies Austria GmbH, Linz, Austria,

Introduction

The basic oxygen steelmaking process generates approximately 70% of the worldwide produced crude steel, making it one of the most important primary steelmaking processes. The main target of this process is the decrease of impurities in liquid metal by oxidizing them trough oxygen blowing. At present the modelling is limited which makes the process highly dependent on the knowledge and prior experience of the operator. Thus, the current work proposes a dynamic model in gPROMS ModelBuilder® to deepen the understanding of the process by offering insight into the reactions taking place during an oxygen blow. The model is based on a multizone kinetic theory approach and can explain changes in the critical process parameters such as flux additions, vessel and nozzle geometry. The model will be compatible with gPROMS based model library for balancing iron and steel production.

Figure 1: Basic Oxygen Furnace at Primetals [2]

Basic Oxygen Steelmaking Process

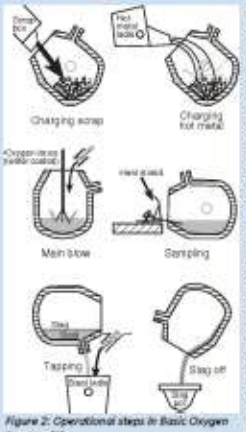

Figure 2: Operational steps in Basic Oxygen Furnace [1]

The process is a six-step batch process (Figure 1). In the beginning the scrap is charged, its main purpose is the consumption of energy which leads to a decrease in temperature during the ensuing exothermic oxygen blow. Followed by the hot metal being charged. After that the lance is lowered into the vessel and the oxygen blow, which is responsible for the oxidation of the impurities, begins. The duration of one blow is usually between 15 and 22 minutes, during which the charge undergoes three main refining periods. Throughout the first period most of the oxygen is consumed by the oxidation of minor elements (Si, Mn, P, Ti, V), and the carbon content decreases linearly. After reaching the critical C-content the mass transfer of dissolved C becomes a rate-limiting step, which is characteristic for the second period. During the third period C is no longer able to reduce all the formed FeO, which leads to a rapid increase of FeO content in slag. Lastly the steel and the slag are tapped separately.

Model

The model is developed in gPROMS ModelBuilder® and is mainly based on the work of Dogan et al. [3] and Rout et al. [4]. It consists of three zones, as depicted in Figure 2, the (i) Impact Zone, (ii) Slag-Bulk Zone and (iii) Emulsion Zone. The kinetics of the refining process in each zone, is represented by mathematical correlations which factor in empirical values as well as the the different phases occurring during the main blow. First the jet velocity, fluid properties and droplet generation rate (Eq. 1) are determined, with the lance height and the converter geometry having a grave impact on the calculation results. Secondly, the (i) and (ii) reaction interface areas are calculated (Eq. 3, 4), followed by the calculation of the emulsion interface (Eq. 2) and the mass transfer coefficients. Lastly, the overall refining rate for the process can be expressed as shown in (Eq. 5).

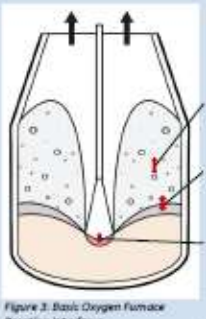

Figure 3: Basic Oxygen Furnace Reaction Interfaces

Supersonic Oxygen Jet

$$\frac{R_B}{F_G} = \frac{(N_{B,T})^{2.2}}{\left[2.6\times10^{6} + 2.0\times10^{-4}(N_{B,T})^{12}\right]^{0.2}} \quad \text{Eq. 1}$$

(iii) Emulsion Zone

$$A_{em} = \frac{R_{B,T}\times t_{res}}{\rho(t)} \quad \text{Eq. 2}$$

(ii) Slag-Bulk Zone

$$A_{sm} = \pi\left(\frac{D_B^2}{4} - n_n \times r_{cav}^2\right) \quad \text{Eq. 3}$$

(i) Impact Zone

$$A_{ii} = n\frac{\pi r_{cav}^4}{6h^2}\left[\left(1+\frac{4h^2}{r_{cav}^2}\right)^{3/2} - 1\right] \quad \text{Eq. 4}$$

Overall Refining Rate

$$\left.\frac{d(W_m C_{jm})}{dt}\right|^{t}_{overall} = \left.\frac{d(W_m C_{jm})}{dt}\right|^{t}_{A_{(i)}} + \left.\frac{d(W_m C_{jm})}{dt}\right|^{t}_{A_{(ii)}} + \left.\frac{d(W_m C_{jm})}{dt}\right|^{t}_{A_{(iii)}} \quad \text{Eq. 5}$$

Results and Discussion

The results as presented in Figure 4 show how different parameters of (i) and (iii) vary with time as a function of the lance height. Various sources suggest that (i) and (ii) do not impact the overall refining significantly. However, they are vital for the understanding of the process with the impact zone (i) being the origin of the emulsion zone (iii), which is the main contributor to the refining reactions. This model is capable of dynamically adapting to varying converter and lance geometries. Future work will focus on implementing time variant oxygen flow and incorporating recent findings on oxygen jet behaviour.

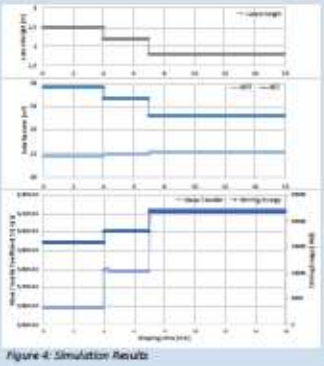

Figure 4: Simulation Results

Summary

- Implementation of three reaction interfaces and their interaction dependent on time
- Detailed consideration of the fluid dynamics within the vessel and the impact on the formation of the interaction interfaces

Outlook

Insight into the evolution of the different refining reactions and their development with respect to time and addition of additives can have a great impact on the control of the process. The presented converter model has the potential to offer the level of understanding and parameter balancing to fine tune the gains in performance.

Acknowledgement

The authors gratefully acknowledge the funding of work by the research program COMET (Competence Center for Excellent Technologies), the Austrian program for competence centers (FFG contract number 869295).

References

[1] Miller, T. W., "Chapter 9 Oxygen Steelmaking Processes," (1999). [2] https://www.primetals.com/de/presse-medien/news/primetals-technologies-to-replace-bof-converter-at-fdb-aerbla-in-smederevo (18.3.2020), 14:43 [3] A. Kadrolkar, N. Dogan Metals 2019, 9, 309, doi:10.3390/met9030309 [4] B.K. Rout, G. Brooks, M. Akbar Rhamdhani, Z. Li, F.N.H. Schrama, J. Sun Metall. Mater. Trans. B, https://doi.org/10.1007/s11663-017-1166-7

2021 Virtual Advanced Process Modelling Forum – 13-15 April 2021

A.9 POSTER

Dynamic Modelling of Basic Oxygen Steelmaking

Arleen Walk *[1], Johannes Niel[1], Bernd Weiß[2], Walter Wukovits[1]

[1]Institute of Chemical, Environmental and Bioscience Engineering, TU Wien, Austria *Author Contact arleen.walk@tuwien.ac.at

[2]Primetals Technologies Austria GmbH, Linz, Austria

Introduction

- Basic oxygen steelmaking (BOS) generates approximately 70% of the worldwide produced crude steel
- The main target of this process is to decrease impurities in liquid metal by oxidizing them
- Research suggests that most of the refining takes place on the surface of droplets generated during the process
- The current work extends a dynamic model in gPROMS Modelbuilder® by detailed droplet refining modelling

Figure 1: Basic oxygen furnace at Primetals [2]

Model Features

- Droplet generation
- Bloated droplet theory
- Model for ballistic motion
- Residence time prediction
- Trajectory of droplet
- Droplet size distribution
- Loss as ash in off-gas
- Compatible with gPROMS based model library for balancing iron and steel production

Former work introduces a dynamic multi zone kinetic gPROMS® model: (presented APM Forum 2021)

- Implementation of three reaction interfaces and the influence of blowing time and lance height on reaction area development and mass transfer coefficients
- Detailed consideration of the fluid mechanics within the vessel and the impact on the formation of the interaction interfaces

Basic Oxygen Steelmaking

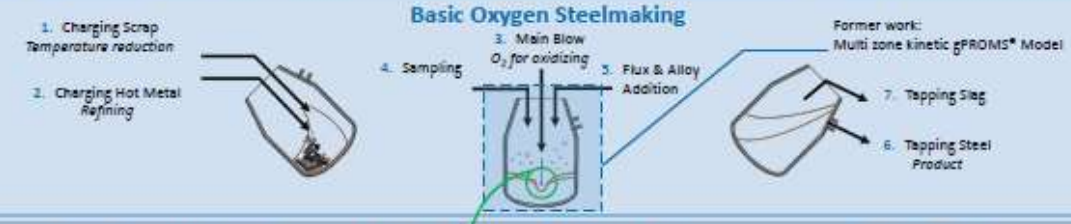

Results and Discussion

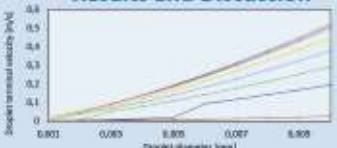

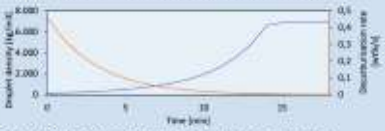

Formation of droplets due to impinging oxygen jet

- Assumptions: perfectly mixed system, ejection angle is known, ejection into a quiescent slag gas mixture
- Studies suggest, that droplets can reside up to two minute in the slag or slag-gas continuum – this is in good accordance with the model predictions

Main influences on residence time:

- Bloating of droplets which occurs due to internal generation CO gas
- Size and ejection angle of metal droplet
- Slag interface velocity and bath stirring

Detailed Droplet Refining Model

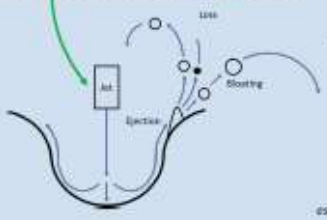

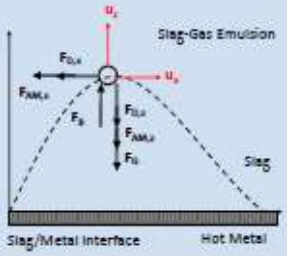

Algorithm

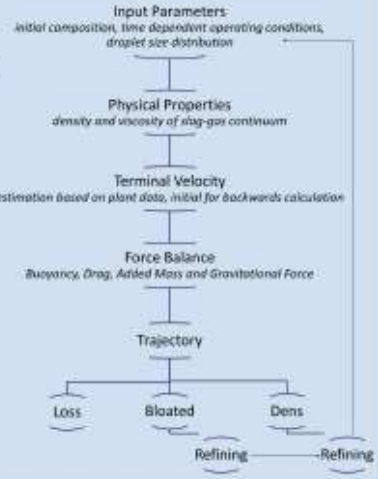

Summary

- Implementation of detailed droplet behavior:
  Model for ballistic motion of metal droplets in slag and slag-gas continuum
  Model for motion of bloated metal droplets in slag and slag-gas continuum including refining reactions [1]
- Detailed consideration of droplet sizes, losses and refining

Outlook

Insight into the evolution of droplet generation and refining with respect to time and varying process conditions can affect the control of the process gravely. The presented and implemented droplet models have the potential to offer a deeper level of understanding on how process parameters influence the refining and thus the environmental and economic gains.

Acknowledgement

The authors gratefully acknowledge the funding of work by the research program COMET (Competence Center for Excellent Technologies), the Austrian program for competence centers (FFG contract number 869295).

References

[1] Subagyo, G.A. Brooks & K.S. Coley (2005) Residence time of metal droplets in slag-metal-gas emulsions through top gas blowing, Canadian Metallurgical Quarterly, 44:1, 119-130, DOI:10.1179/cmq.2005.44.1.119 [2] https://www.primetals.com/de/presse- medien/news/primetals-technologies-to-replace-bof-converter-at-hbis-serbia-in-smederevo (18.3.2020, 14:43)

Advanced Process Modelling Forum 2022 – London, United Kingdom, 18-19 October 2022